TU WIEN
TECHNISCHE UNIVERSITÄT WIEN
Vienna University of Technology

ACIN
AUTOMATION & CONTROL INSTITUTE
INSTITUT FÜR AUTOMATISIERUNGS- & REGELUNGSTECHNIK

Contactless Positioning for Microwave Measurements

DIPLOMARBEIT

Ausgeführt zum Zwecke der Erlangung des akademischen Grades eines
Diplom-Ingenieurs (Dipl.-Ing.)

unter der Leitung von
Univ.-Prof. Dr.sc.techn. Georg Schitter
Dipl.-Ing. Mathias Poik
Dipl.-Ing. Thomas Hackl

eingereicht an der
Technischen Universität Wien
Fakultät für Elektrotechnik und Informationstechnik
Institut für Automatisierungs- und Regelungstechnik

von
Martin Schober
Matrikelnummer: 01226965

Wien, im Februar 2023

Advanced Mechatronic Systems Group
Gußhausstraße 27-29, A-1040 Wien, Internet: http://www.acin.tuwien.ac.at

Die approbierte gedruckte Originalversion dieser Diplomarbeit ist an der TU Wien Bibliothek verfügbar
The approved original version of this thesis is available in print at TU Wien Bibliothek.
TU WIEN Bibliothek Your knowledge hub

Abstract

The production of integrated circuits and electronic devices demands a high level of quality and process control. The standard procedure to test a device for functionality is to contact it with probes that have the same or even greater size than the device itself. A lot of research is done to remedy this by introducing probes and measurement techniques, where a sharp tip of few nanometres radius maps the local properties of a device. The lateral resolution of these probes extends into the nanoscale. This great locality of the measurement demands the probe to be in mechanical contact, or few tenths of nanometres off, the device surface. Many measurement methods therefore fail when a device is passivated, since passivation layers can have up to micrometers of thickness. Another problem is the mechanical interaction with the surface, which can damage the probe and device surface. Recently high frequency measurement methods which interface the probe to a Network Analyser have emerged that operate within the microwave spectrum. These are able to extend the penetration depth past the passivation and enable accurate subsurface imaging. These methods rely on the capacitive coupling between the tip and the device, which is highly position sensitive and influences reflection and transmission coefficients at the tip to sample interface.

In this work a positioning strategy is proposed and implemented to accurately position a cantilever probe, which is based on a differential measurement of the reflection coefficient. This implementation aims to be as non-invasive as possible, meaning the positioning process does not require any physical tip-surface-interaction during the measurement. With a calibration of materials, regarding their tip to sample surface distance, a defined vertical position can be established. Lateral position information can be derived from material property changes, which are translated to different tip to sample surface distances during a scan. This also offers the possibility of detecting material faults, since every known material composition has its own assigned distance. Typical vertical positioning errors are below 30 nm and lateral positioning errors are within 150 nm in the presented experiments. The procedure is limited in speed by the filter bandwidth and the data transmission rate of the involved measurement equipment to about 10 micrometers per minute.

Die approbierte gedruckte Originalversion dieser Diplomarbeit ist an der TU Wien Bibliothek verfügbar
The approved original version of this thesis is available in print at TU Wien Bibliothek.
TU WIEN Bibliothek Your knowledge hub

Zusammenfassung

Die Produktion von integrierten Schaltungen und Computerchips erfordert ein hohes Maß an Güte in der Qualitäts- und Prozesskontrolle. Der industrielle Standard zur Prüfung auf Funktion ist den Chip mit Prüfspitzen zu kontaktieren. Jedoch sind die Kontaktflächen, die dazu benötigt werden, groß, wodurch nicht auf interne Charakteristika geprüft werden kann. Viel Forschung beschäftigt sich mit kleineren Prüfspitzen und neuen Messmethoden, bei der mit scharfen Prüfspitzen von wenigen Nanometern Enddurchmesser lokale Eigenschaften von Prüflingen abgebildet werden können. Diese Spitzen erlauben Messungen mit Nanometer-Auflösung. Die Lokalität der Messung erfordert, dass die Spitze in mechanischem Kontakt mit der zu prüfenden Stelle, oder nur wenige zehn Nanometer davon entfernt ist. Passivierung von Prüflingen macht diese erforderliche Nähe oft unmöglich, da sie bis zu Mikrometer dick sein kann. Zusätzlich kann der andauernde Kontakt zur Oberfläche während des Messvorganges sowohl die Spitze, als auch den Prüfling beschädigen. Messmethoden, die diese Prüfspitzen mit Hochfrequenzmessgeräten, z.B. Netzwerkanalysatoren, verbinden und Messungen im Mikrowellenspektrum durchführen, sind in der Lage Passivierungen zu durchdringen und akurate Messergebnisse ohne direkten Kontakt zu liefern. Sie basieren auf den Reflexions- und Transmissionkoeffizienten an dem kapazitiven übergang zwischen der Prüfspitze und dem Prüfling, der stark von der Positionierung der Spitze abhängt.

In dieser Arbeit wird eine Strategie zur Positionierung von elektrisch leitfähigen Rasterkraftsonden präsentiert, die auf differenziellen Hochfrequenzmessungen des Reflexionskoeffizienten basiert. Diese Implementierung hat das Ziel kontaktlos zu sein. Durch Kalibration von Materialien auf Abstände zwischen der Spitze und Oberfläche kann eine vertikale Position vorgegeben werden. Laterale Information zur Positionierung wird aus Veränderungen von Materialeigenschaften gewonnen, die durch die Messmethode in unterschiedliche Abstände zwischen der Spitze und der Oberfläche während eines Scanvorganges umgewandelt werden. Dies hat den Vorteil, dass auch Materialfehler erkannt werden können, da diese in einer unerwarteten Distanz zur Oberfläche münden. Der typische Positionierfehler liegt in der Vertikalen bei weniger als 30 nm und lateral bei weniger als 150 nm in den präsentierten Versuchen. Die Scangeschwindigkeit ist durch Messzeitkonstanten auf etwa 10 Mikrometer pro Minute begrenzt.

Die approbierte gedruckte Originalversion dieser Diplomarbeit ist an der TU Wien Bibliothek verfügbar
The approved original version of this thesis is available in print at TU Wien Bibliothek.
TU WIEN Bibliothek Your knowledge hub

Contents

1 Introduction **1**
1.1 Motivation . . . 1
1.2 Goal of this thesis . . . 2
1.3 Structure of this work . . . 3

2 State of the Art **4**
2.1 Common probes for microwave measurements . . . 4
2.1.1 Contact-based measurements . . . 4
2.1.2 Contactless measurements . . . 6
2.2 Cantilever-based probing . . . 10
2.2.1 RF Measurement principles . . . 11
2.2.2 Scanning Microwave Microscopy (SMM) . . . 13
2.2.3 Imaging of subsurface structures . . . 14
2.3 Probe positioning . . . 16

3 Proposed positioning strategy and evaluation system **18**
3.1 System description and requirements . . . 18
3.1.1 Sample properties . . . 19
3.1.2 Positioning performance . . . 20
3.2 Positioning Strategy . . . 21
3.2.1 Calibration of materials . . . 21
3.2.2 Vertical positioning . . . 22
3.2.3 Lateral positioning . . . 22
3.3 Evaluation of position . . . 23
3.4 System Overview . . . 24

4 Theory **25**
4.1 Transmission Line Model . . . 25
4.2 Waveguides . . . 28
4.3 Scattering Parameters . . . 29
4.4 Vector Network Analyser measurement principle . . . 30
4.5 Interferometric RF measurements . . . 31

Die approbierte gedruckte Originalversion dieser Diplomarbeit ist an der TU Wien Bibliothek verfügbar
The approved original version of this thesis is available in print at TU Wien Bibliothek.
TU WIEN Bibliothek Your knowledge hub

4.6 Atomic Force Microscopy . . . 33
4.7 Model-Based RF Voltage Sensing . . . 34

5 Implementation **36**
5.1 System Overview . . . 36
5.2 Probe and VNA interface . . . 40
5.3 Vector Network Analyser . . . 40
5.4 Samples . . . 42
5.5 Real Time System . . . 44
5.6 Sensor Characterisation . . . 44

6 Evaluation of measurement capabilities **47**
6.1 Atomic force microscope in contact mode . . . 47
6.2 Scanning Microwave Microscopy, Contact Mode . . . 49
6.3 Scanning Microwave Microscopy, Lift Mode . . . 52
6.4 Evaluation of the implemented measurements and measurement drift . . . 55

7 Non-invasive probe positioning **58**
7.1 Differential measurements . . . 58
7.2 Contactless Differential Measurements . . . 64
7.3 Vertical calibration and positioning . . . 66
7.3.1 Verification of vertical positioning . . . 69
7.4 Lateral positioning . . . 73
7.5 Faults and unexpected behaviours . . . 76

8 Conclusion and Outlook **78**
8.1 Summary and Conclusion . . . 78
8.2 Outlook . . . 79

Die approbierte gedruckte Originalversion dieser Diplomarbeit ist an der TU Wien Bibliothek verfügbar
The approved original version of this thesis is available in print at TU Wien Bibliothek.
TU WIEN Bibliothek Your knowledge hub

List of Figures

2.1 DUT with connected GSG probes. 4
2.2 Wafer probing station. 5
2.3 MPI T110A GSG50 Probe. 5
2.4 MPI Titan DC-220GHz Probe 6
2.5 SEM images of GSG micro probes. 6
2.6 Different RF Measurement Probes. 7
2.7 Coaxial probe with tungsten needle attached. 8
2.8 Magnetic Loop Probe. 9
2.9 Magnetic field of microstrip line. 9
2.10 SEM image of shielded cantilever probe 10
2.11 SEM image of RMN 25Pt300 probe. 11
2.12 Basic RF measurement setup 12
2.13 Methods to enhance sensitivity in microwave measurements 12
2.14 Schematic drawing of a SMM setup 13
2.15 Subsurface imaging with SMM 14
2.16 Overview of subsurface imaging techniques. 15

3.1 Basic RF measurement setup 19
3.2 Allowed changes of material and topography 20
3.3 Expected change of tip position during scan 21
3.4 Vertical position control scheme 22
3.5 Simplified measurement setup 24

4.1 Infinitesimal small section of a transmission line 26
4.2 Grounded coplanar waveguide structure. Gold is conductor material and green is dielectric. 28
4.3 Schematic of a two port S-Parameter measurement. 29
4.4 Simplified block diagram of a 2-Port VNA measurement. 30
4.5 Input reflection coefficient of a series of two port networks 31
4.6 Block diagram of an optical Michelson Interferometer. 32
4.7 Interferometric setup with a power splitter and phase shifter 33

Die approbierte gedruckte Originalversion dieser Diplomarbeit ist an der TU Wien Bibliothek verfügbar
The approved original version of this thesis is available in print at TU Wien Bibliothek.
TU WIEN Bibliothek Your knowledge hub

4.8 Deflection measurement and transmission coefficient measurement over vertical position 35

5.1 Block diagram of the developed test setup. 36
5.2 SEM images of conductive cantilever 37
5.3 RF-PCB with SMA connector, waveguide and cantilever chip. 37
5.4 Flexure with piezoelectric actuator and screwed on RF-PCB. 38
5.5 Assembly of the AFM measurement head. 38
5.6 Complete physical measurement setup. 39
5.7 GUI to control the system and perform measurements 40
5.8 Sketch of physical VNA connections 41
5.9 Interdigital capacitor sample. 42
5.10 Dopant calibration sample overview 42
5.11 Photo of dopant calibration sample 43
5.12 SMM test samples. 43
5.13 Control schemes for vertical position 44
5.14 Strain gauge characterisation. 45
5.15 Deflection measurement in AFM and QPD characterisation. 46

6.1 AFM images of interdigital capacitor structure 48
6.2 AFM and SMM images of dopant calibration sample 50
6.3 AFM and SMM images of spiral structure beneath passivtaion 51
6.4 AFM and SMM images of dopant calibration sample in lift mode . . . 53
6.5 AFM and SMM images of spiral structure beneath passivtaion in lift mode 54
6.6 Topography image and SMM line scan of spiral sample in contact and lift mode 55
6.7 Drift of measurements over 16 hours 56
6.8 Topography image and SMM line scans of spiral sample in lift mode at different positions 57

7.1 Approach curves of reflection coefficient on passivated sample 60
7.2 Map of non-linear weighting factor of metal pads 61
7.3 Map of non-linear weighting factor on 6.5 um square metal pad 62
7.4 Measurement areas on interdigital capacitor 62
7.5 Map of non-linear weighting factor on passivated metal finger structures 63
7.6 Map of non-linear weighting factor on passivated metal finger structures with 1.5 um passivation 63
7.7 Map of non-linear weighting factor on passivated metal finger structures with 0.5 um passivation 63
7.8 Principle of differential measurement 64
7.9 Difference quotient approach curves for gold electrode and bulk silicon . 65
7.10 Difference quotient approach curves for metal pad and bulk silicon under 500nm passivation 66
7.11 Differential measurement over tip to sample distance for different amplitudes 67
7.12 Difference quotient over tip to sample distance for different amplitudes on gold 67

Die approbierte gedruckte Originalversion dieser Diplomarbeit ist an der TU Wien Bibliothek verfügbar
The approved original version of this thesis is available in print at TU Wien Bibliothek.
TU WIEN Bibliothek Your knowledge hub

7.13 Difference quotient over tip to sample distance for different amplitudes on silicon 68
7.14 Difference quotient for gold and silicon 68
7.15 Vertical calibration on gold and silicon 69
7.16 Verification measurement of tip to sample distance 70
7.17 Absolute distance to sample error for different targets on gold 71
7.18 Absolute distance to sample error for different targets on silicon 71
7.19 Absolute distance to sample error for different amplitudes on gold . . . 72
7.20 Possible target selection for lateral positioning and resulting height lines. 73
7.21 Line scan on int.-dig. capacitor sample with control of difference quotient 74
7.22 Line scan of passivated 15 μm square metal pad with diff. quotient control. 75
7.23 Normalized line scan on passivated square metal pad with diff. quotient control and model based voltage sensing. 75
7.24 Normalized line scan on passivated resistor structure with non-linear fitting method 77

Die approbierte gedruckte Originalversion dieser Diplomarbeit ist an der TU Wien Bibliothek verfügbar
The approved original version of this thesis is available in print at TU Wien Bibliothek.
TU WIEN Bibliothek Your knowledge hub

List of Tables

7.1 Mean and standard deviation of absolute error measurements on gold electrode with different targets. 71
7.2 Mean and standard deviation of absolute error measurements on bulk silicon with different targets. 71
7.3 Mean and standard deviation of absolute error measurements on gold electrode with different amplitudes. 72

Die approbierte gedruckte Originalversion dieser Diplomarbeit ist an der TU Wien Bibliothek verfügbar
The approved original version of this thesis is available in print at TU Wien Bibliothek.
TU Bibliothek WIEN Your knowledge hub

Acronyms

ACIN	Automation and Control Institute
AFM	Atomic Force Microscopy
AMS	Advanced Mechatronic Systems Group
C-AFM	Conductive AFM
DUT	Device Under Test
EFM	Electrostatic Force Microscopy
GCPW	Grounded Coplanar Waveguide
GSG	Ground-Signal-Ground
GUI	Graphical User Interface
IF	Intermediate Frequency
KPFM	Kelvin Probe Force Microscopy
LO	Local Oscillator
MFM	Magnetic Force Micoscropy
PCB	Printed Circuit Board
QPD	Four Quadrant Photo Detector
RF	Radio Frequency
SCM	Scanning Capacitance Microscopy
SEM	Scanning Electron Microscopy
SG	Strain Gauge
SMA	SubMiniature A
SMIM	Scanning Microwave Impedance Microscopy
SMM	Scanning Microwave Microscopy
SPM	Scanning Probe Micoscropy
VNA	Vector Network Analyser

Die approbierte gedruckte Originalversion dieser Diplomarbeit ist an der TU Wien Bibliothek verfügbar
The approved original version of this thesis is available in print at TU Wien Bibliothek.
TU WIEN Bibliothek Your knowledge hub

Symbols

A	Amplitude
C	Capacitance
C'	Distributed Capacitance
G	Conductance
G'	Distributed Conductance
I	Current
L	Inductance
L'	Distributed Inductance
N_A	Number of Atoms per qubic centimetre
R	Resistance
R'	Distributed Resistance
R_{eff}	Effective Tip Size
S_{XY}	Scattering Parameter
T	Target Value
U, V	Voltage
Z	Impedance
Z'	Distributed Impedance
Z_0	Characteristic Transmission Line Impedance
Γ	Reflection Coefficient
α	Attenuation
β	Phase shift
ϵ_r	Relative Permittivity
ϵ_{eff}	Effecitve Permittivity
γ	Propagation Constant
λ	Wavelength
ω	Angular Frequency
c	Speed of Light
d	Thickness of Passivation
d_z	Tip to Sample Distance
f	Frequency
z	Differential Measurement Range

Die approbierte gedruckte Originalversion dieser Diplomarbeit ist an der TU Wien Bibliothek verfügbar
The approved original version of this thesis is available in print at TU Wien Bibliothek.
TU WIEN Bibliothek Your knowledge hub

CHAPTER 1

Introduction

1.1 Motivation

Millimetre wave technology has found its way into consumer electronics with 5G and radar applications have surpassed 100 GHz and applications in the medical field and material sciences operate into the terahertz region [1]. Electronics for those high frequencies are still a topic for research and challenging in their own way. In the last decades integrated circuits have been shrunk to sizes so small that practically any device of our daily life has been equipped with microchips and networking capabilities. Everything talks to each other and the number of connected devices is soon to be expected to outgrow the number of humans on this planet [2]. To be able to provide such huge quantities of interconnected devices the semiconductor industry has grown as well [3]. With each step to a new, smaller structure the demands on the quality control of their facilities and manufacturing processes increase. It is paramount to recognize faults and potential failure hazards in the early stages of prototyping of a new device.

To test the functionality of a device and characterize its behaviour, RF signals are applied at its input and measured at its output with contact pads, that are typically interfaced with Ground-Signal-Ground probes [4] to a Vector Network Analyzer. These probes offer a reliable testing method with high throughput on a standardized platform. Correct positioning of the probes is important to ensure accurate and repeatable measurements of the device properties. Manual or semi-automatic wafer probing stations are commonly used to do this and research is done on automatic probe positioning with computer vision algorithms [5]. The landing pads for these probes are tens to hundreds of micrometers in size and sometimes even bigger than the device itself, so a lot of chip space is occupied for probing. Wirelessly interconnecting devices always includes high frequency transmissions and while they are low power on the receiving end, the senders are large and require high power. Internal analysis of device properties during operation is desirable, especially in the prototyping phase to detect unwanted behaviour early. For instance, the knowledge of voltage distributions in power amplifiers and switches

Die approbierte gedruckte Originalversion dieser Diplomarbeit ist an der TU Wien Bibliothek verfügbar
The approved original version of this thesis is available in print at TU Wien Bibliothek.
TU WIEN Bibliothek Your knowledge hub

that operate in the GHz bands is often wanted [6], but not accessible because of the size of these conventional probes.

New measuring techniques that involve a single sharp probe tip, that is positioned to be in direct contact or slightly above an area of investigation, enable the precise mapping of material and electrical properties like voltage- [7], current- [8] and doping concentration distributions [9]. These probes are much smaller than the standard GSG-probes and are able to measure on the micro- to nanoscale, so equally precise positioning on the same scale is required. They are often positioned by measuring topography or are scanned over a certain area of interest. A limitation of direct, contact-based probing is, that it is in many cases impossible due to the nature of how structures are grown layer by layer [10], or undesirable because the probe could interfere with the circuits and distort the measurement. Probing methods without direct contact to the sample are often performed in a differential procedure to eliminate cross-talk, which leads to a loss of sensitivity. Another hindrance to contact-based and contactless measurements can be the passivation of a device surface, which completely seals off any direct contact to its internals and provides no topographic information, thus making precise probe positioning more difficult. It also results in worse sensitivity due to the forced distance between of the probe and the area of interest. Contact-based probing in itself may also be undesirable due to probe wear, because probe degradation results in worse measurement accuracy [11]. Contact pads can be added to establish a connection to parts of the device that are buried or where probe interference may be problematic, but they need to be on a much smaller scale than the standard Ground-Signal-Ground pads.

Therefore a solution that can provide a defined probe location in relation to a given device section with electrical or material properties of interest, or small pad that interfaces to such internal quantities, is needed. This solution should not require any contact of the probe to the device to prevent probe and sample degradation.

1.2 Goal of this thesis

The goal of this thesis is to provide a contactless positioning strategy for cantilever-probe-based microwave measurement methods that establishes a well-defined tip location in all spatial dimensions. A suitable setup to develop, implement, test and validate this strategy is to be designed and constructed. To this end an atomic force microscope (AFM) and a scanning microwave microscope (SMM) are combined. In a first step the probe should be positioned manually in close vicinity (few micrometre accuracy) to an area of interest with the aid of a camera setup. From there the implemented positioning strategy should be able to position the probe at a desired location by detecting changes in the tip-sample impedance, which is determined by measuring the reflection coefficient at the tip-sample interface with a vector network analyser. For the lateral position sub-micrometer accuracy is demanded, based on the typical structure size of microwave devices which ranges from single to tens of micrometres. The vertical tip position accuracy should be as good as possible since the vertical tip distance from the device

Die approbierte gedruckte Originalversion dieser Diplomarbeit ist an der TU Wien Bibliothek verfügbar
The approved original version of this thesis is available in print at TU Wien Bibliothek.
TU WIEN Bibliothek Your knowledge hub

surface is a crucial factor in the performance of contactless microwave measurements. A value of less than 100 nm is expected to be achievable, although better accuracy is of course desirable. The whole positioning process should be as non-invasive as possible, i.e. no contact between a given sample and the cantilever tip shall occur at any time to preserve the tip and sample surface. This ensures the integrity of measurements that follow the positioning procedure over longer periods of time. Verification for externally accessible information such as topography changes and the vertical positioning are provided by the AFM.

To summarize the key goals:

- Development of a suitable test setup that combines AFM and SMM.
- Development of a non-invasive positioning strategy using microwave measurements.
- Verification of the position with AFM.

1.3 Structure of this work

Chapter 2 presents the state of the art of current probes and their positioning methods, some of the applications of those probes that are similar to the approach discussed in this work, the spatial accuracy of those applications, as well as their limitations on imaging subsurface features. In Chapter 3 the structure of the test setup is presented and Chapter 4 explains the theory behind the measuring techniques that are used in this work and provides a more in depth explanation of how they are combined to provide accurate results. Chapter 5 discusses the implementation and limitations of the test setup. Chapter 6 discusses if the implemented techniques are suitable to achieve the intended goals and presents solutions if they are not. Chapter 7 presents the final procedures to reach those goals and how they are implemented, as well as their results. The end of this work is Chapter 8, which summarizes this work and its results, and gives an outlook for possible improvements.

Die approbierte gedruckte Originalversion dieser Diplomarbeit ist an der TU Wien Bibliothek verfügbar
The approved original version of this thesis is available in print at TU Wien Bibliothek.
TU WIEN Bibliothek Your knowledge hub

CHAPTER 2

State of the Art

In this chapter different types of probes are presented, as well as their application in contact-based and contactless microwave measurements and how those measurements can be used to determine different material qualities. Additionally a brief overview of common subsurface imaging techniques is provided, as well as a more detailed explanation of Scanning Microwave Microscopy (SMM), to illustrate why SMM is chosen for this work. A discussion of different probe positioning techniques and their limitations, based on the employed probes, concludes this chapter.

2.1 Common probes for microwave measurements

2.1.1 Contact-based measurements

The industry standard in probing of a device under test (DUT) is to do a purely functional test by connecting one Ground-Signal-Ground (GSG) probe at an input and one GSG probe at an output of the device. Figure 2.1 [12] shows a typical configuration of such a test.

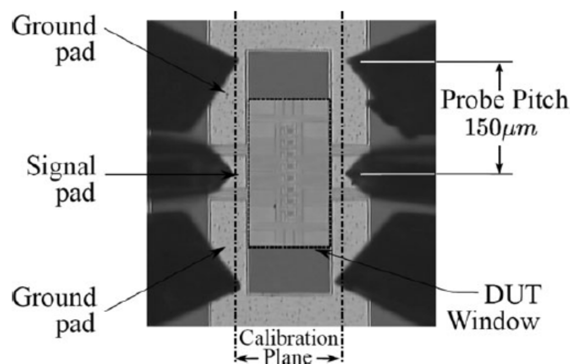

Figure 2.1: DUT with connected GSG probes [12].

Die approbierte gedruckte Originalversion dieser Diplomarbeit ist an der TU Wien Bibliothek verfügbar
The approved original version of this thesis is available in print at TU Wien Bibliothek.
TU WIEN Bibliothek Your knowledge hub

These probes are usually mounted on a wafer probing station as shown in Figure 2.2. These stations hold the sample (wafer) with a vacuum pump in place and offer a height adjustable table with mounting options for different measurement applications. While it is possible to mount more than two probes, space requirements on the chip quickly become a limiting factor for smaller devices.

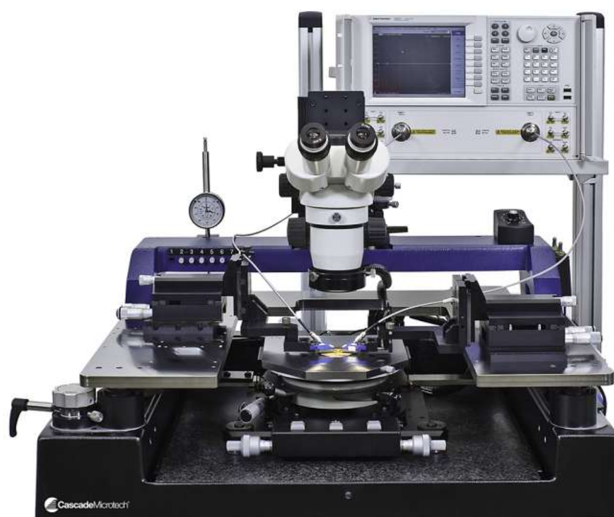

Figure 2.2: Manual wafer probing station Form Factor PM8 [13].

The frequency range in which they can measure depends on the type of measurement equipment and connector (and cable) that is used to interface the probes. Typical maximum values range from 26GHz (SMA) to 110GHz (1mm). From 110GHz upward probes are interfaced with cavity waveguides. Figure 2.3 shows a classical GSG probe that operates up to 110GHz, Figure 2.4 a 220GHz probing configuration that requires frequency extenders directly attached to the probes.

Figure 2.3: MPI T110A GSG50 probe, operates up to 110 GHz with a 1mm coaxial connector[1].

[1]https://www.mpi-corporation.com/wp-content/uploads/2020/02/T110A-GSG50-1.jpg

Die approbierte gedruckte Originalversion dieser Diplomarbeit ist an der TU Wien Bibliothek verfügbar
The approved original version of this thesis is available in print at TU Wien Bibliothek.
TU WIEN Bibliothek Your knowledge hub

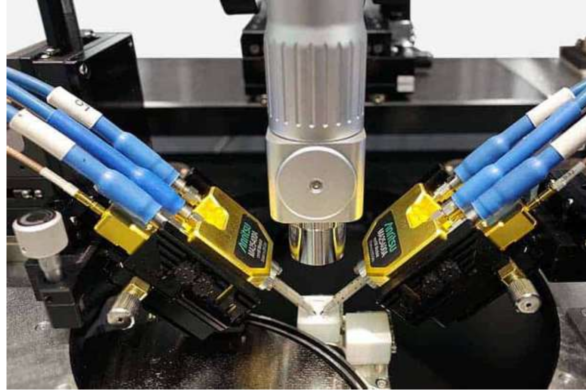

Figure 2.4: Probing configuration up to 220GHz with a MPI Titan DC-220GHz Probe[2].

There have also been attempts to miniaturize these probes [14], Figure 2.5, but a smaller probe inherently needs better positioning to ensure good and reliable contact. This is a problem that has not been finally solved for regular GSG probes, so it is to be seen if these miniaturizations can replace their bigger counterparts in the future.

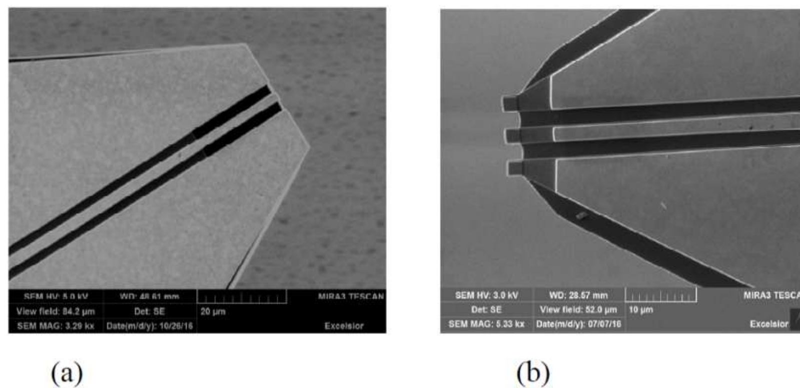

Figure 2.5: SEM images of GSG micro probes (a) first and (b) second generation [14].

2.1.2 Contactless measurements

In addition to these GSG probes there are many other microwave probes, that employ measurement techniques that do not need a fixed connection, and therefore allow scanning operations to quantify electrical characteristics of a DUT over large areas.
The basic types of (non-GSG) probes involved in microwave measurements are depicted in Figure 2.6. They all operate on the same basic principle. A conductive probe with certain geometrical features is placed in close vicinity or contact with the sample surface and primarily coupled to it via a capacitance. These probes can be categorized in active and passive probes, depending on their state of excitation. For measurements using an active probe an outgoing electrical wave is directed at a certain area of the sample. The wave interacts with materials underneath the probe and energy of the wave is either transmitted to conductive structures or reflected back to probe. In

[2]https://www.mpi-corporation.com/wp-content/uploads/2020/02/T220-GHz.jpg

TU Bibliothek WIEN Your knowledge hub
Die approbierte gedruckte Originalversion dieser Diplomarbeit ist an der TU Wien Bibliothek verfügbar
The approved original version of this thesis is available in print at TU Wien Bibliothek.

general there is a mix, so a part gets transmitted and a part reflected. The amount of transmission or reflection is then measured and provides information of the involved materials underneath the probe. Passive probe measurements involve scanning the active areas of a powered device, using the probe as a pickup for electrical signals. Here usually only the transmission from the active device area to the probe is measured.

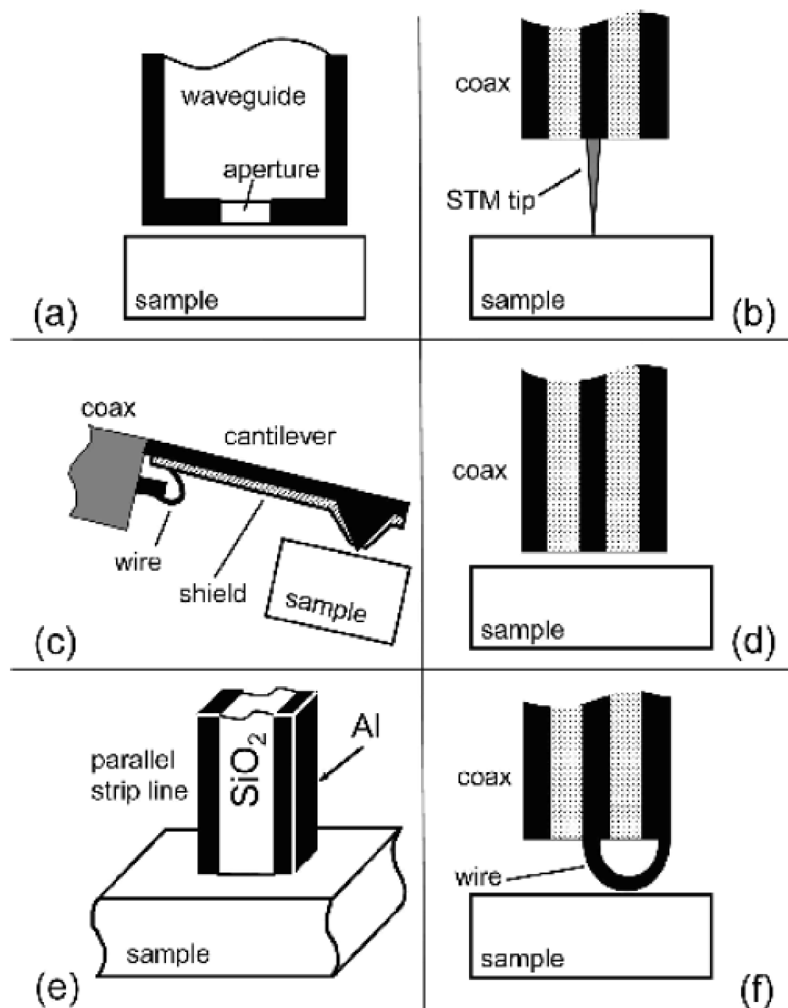

Figure 2.6: Different RF measurement probes: (a) aperture in a waveguide, (b) STM tip, (c) AFM tip, (d) open end of coaxial line, (e) parallel stirp transmission line, (f) magnetic loop [15].

The most basic probes measure by pointing the apertures of waveguides onto a certain area of a sample (Figure 2.6 (a),(d) and (e)). The outgoing wave interacts with whatever is beneath the aperture and the part that gets reflected back along the waveguide is indicative of certain material properties. Alternatively there can be an active circuit underneath the probe and the probe picks part of the signals in the active area. The resolution for these kinds of probes is in the same range as the aperture and they can be implemented easily. Practically any waveguide shape is suitable as long as they are designed to carry only the desired propagation modes.

Die approbierte gedruckte Originalversion dieser Diplomarbeit ist an der TU Wien Bibliothek verfügbar
The approved original version of this thesis is available in print at TU Wien Bibliothek.
TU WIEN Bibliothek Your knowledge hub

Similar probes use an open ended coaxial cable as the waveguide. There are different attachment configurations for these probes that define the measurement quantity and resolution. Figure 2.6 (b) and (f) show two examples. Firstly, a sharpened wire or needle (i.e made of tungsten) which is pressed into the inner coaxial conductor. Such a setup is often employed to measure voltage [16] or current distributions in power devices. Figure 2.7 shows such a configuration to measure the electrical fields in proximity to the fingers of a GaN HEMT [17].

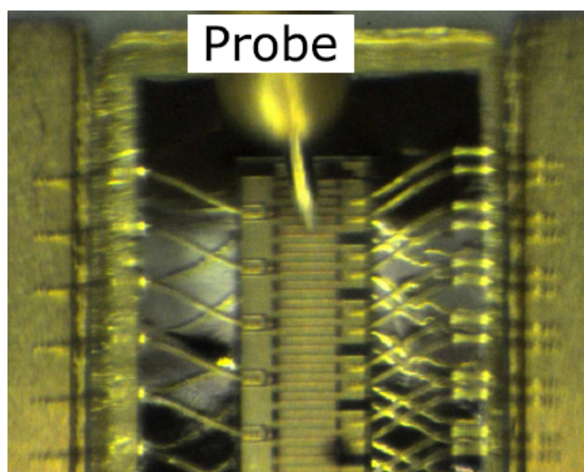

Figure 2.7: Measurement setup with a tungsten tip that is pressed into the inner conductor of a coaxial cable to measure electrical fields in a GaN HEMT [17]

The second widely employed attachment is a loop, either as a wire or manufactured on a substrate, that acts as a magnetic field probe as depicted in Figure 2.8. It shows an example for a probe that operates up to 30 GHz to measure magnetic fields of waveguide structures [18]. Such a measurement on a microstrip line is depicted in Figure 2.9.

The resolution of these probes is on the same scale as the smallest design dimension that interacts with the sample, i.e. the tip radius of the sharpened needle or effective area of the loop. This can range from single to hundreds of micrometres. It also depends on the distance to the sample surface since they are coupled to the DUT by electric or magnetic fields and lose the locality of the measurement at greater distances.

Die approbierte gedruckte Originalversion dieser Diplomarbeit ist an der TU Wien Bibliothek verfügbar
The approved original version of this thesis is available in print at TU Wien Bibliothek.
TU WIEN Bibliothek Your knowledge hub

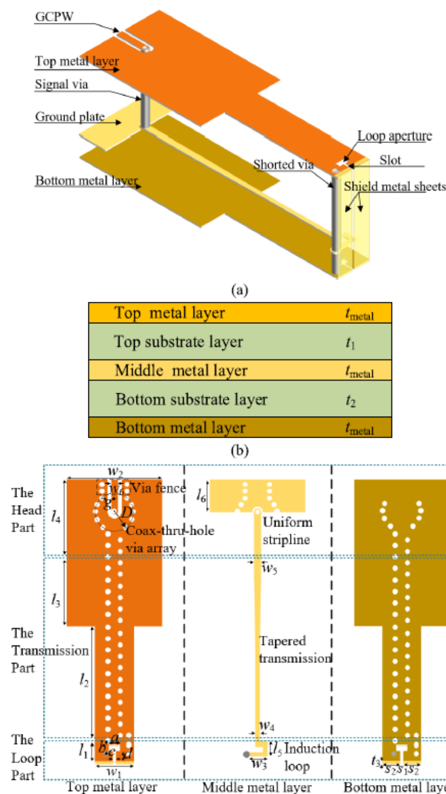

Figure 2.8: Magnetic loop probe manufactured on a multilayer PCB [18].

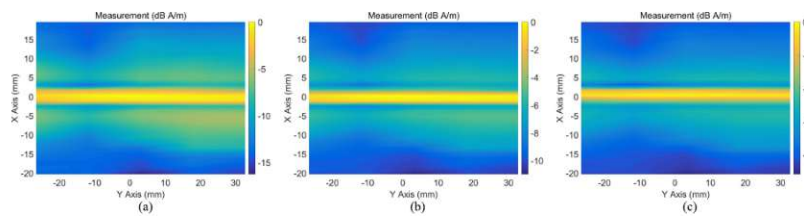

Figure 2.9: Measured magnetic field distribution of a microstrip line at (a) 5, (b) 15 and (c) 25GHz [18].

Die approbierte gedruckte Originalversion dieser Diplomarbeit ist an der TU Wien Bibliothek verfügbar
The approved original version of this thesis is available in print at TU Wien Bibliothek.
TU WIEN Bibliothek Your knowledge hub

2.2 Cantilever-based probing

The last basic type of probe, that has gained a lot of traction in the last two decades, is the conductive cantilever probe. Its origin lies with the atomic force microscope (AFM) where the optical lever method is used to measure topography on the nanometre scale. Chapter 4.6 gives a detailed explanation on how this method works and how it is employed to position such a probe based on changes in topography. AFM probes feature a conical or pyramid shaped tip that is attached to a cantilever. These cantilevers are typically made from silicon or silicon-nitride and can be sputtered or (vapour-) plated with conductive materials like gold or platinum to enable electrical measurements. Tip radii for highly specialized probes can be in the range of single atoms but conventional probes feature tip radii of 5-20nm.

Two kinds of these probes are dominant for microwave measurements, because they work on the principle that only the tip of the probe has significant interaction with sample and the rest of the probe (the cantilever beam) can be neglected or compensated by differential measurements. Figure 2.10 shows the first one, a shielded cantilever [19][20][21]. These are usually custom made by researchers and are often tailored to specific needs.

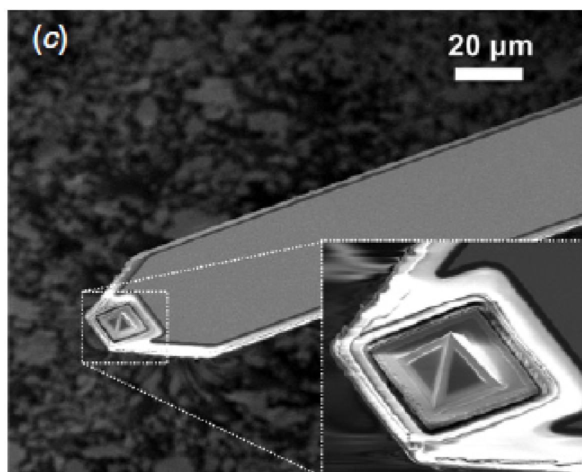

Figure 2.10: SEM image of electrically shielded cantilever probe [19].

Figure 2.11 shows the other kind that is often used. It is a conductive cantilever, in this case made from platinum foil, that has a very long tip (compare this probe to the dimensions in Figure 2.10). This long tip minimizes the electrical interaction of the cantilever beam with the sample. It has been successfully employed in many forms of measurements and can be used with any standard AFM. Because they offer the same properties as classical AFM probes, they can be used in the same way to map topography on the nanoscale.

Die approbierte gedruckte Originalversion dieser Diplomarbeit ist an der TU Wien Bibliothek verfügbar
The approved original version of this thesis is available in print at TU Wien Bibliothek.
TU Wien Bibliothek Your knowledge hub

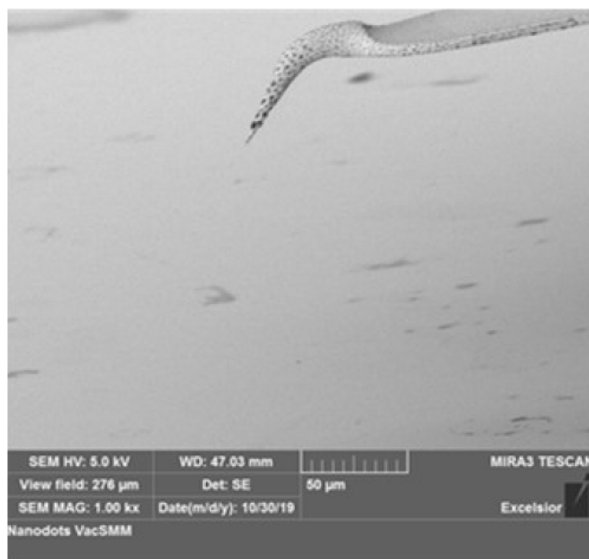

Figure 2.11: SEM image of a Rocky Mountain Nanotechnology 25Pt300B probe [29].

Many different electrical and mechanical measurements can be combined with the AFM. Conductive AFM (C-AFM) [22], Kelvin Probe Force Microscopy (KPFM) [23][24], Electrostatic Force Microscopy (EFM) [25] and Scanning Microwave Microscopy (SMM) [26] for electrical properties, Magnetic Force Microscopy [27] for magnetic properties and Force Spectroscopy [28] for mechanical properties are examples of a multitude of extensions available to the AFM platform.

2.2.1 RF Measurement principles

Extensive research has produced many different measurement techniques that can be employed to measure a multitude of electrical and material properties with cantilever-based microwave measurements. Some examples are the mapping of voltage distributions [16][26][30], current distributions [8], doping concentration distributions [9][31], resistivity [32][33] and permittivity [34][35][36], or charge distributions [37].

The details to these kinds of measurements vary, but the basic setup is always similar. Figure 2.12 (a) shows this basic setup that consists of a conductive cantilever that is interfaced to a vector network analyser (VNA) by a waveguide. Tip-to-sample distance, the measurement frequency and sample material properties influence the capacitive coupling and therefore the local impedance at the tip-sample interface. This translates to different magnitudes of reflection or transmission of electrical waves. Depending on the measurement quantity (the reflected wave, the transmitted wave or both) the sample, or structures on it, may also be connected to the VNA via different probes. To improve the sensitivity for purely passive samples with an active probe (measurement of reflection, no RF excitation of the sample) many implementations also feature a half wavelength resonator (Figure 2.12 (b)) or interferometric extension to enhance their measurement sensitivity (Figure 2.12 (c)). The principle is to find a resonance

Die approbierte gedruckte Originalversion dieser Diplomarbeit ist an der TU Wien Bibliothek verfügbar
The approved original version of this thesis is available in print at TU Wien Bibliothek.
TU WIEN Bibliothek Your knowledge hub

which depends on the tip-sample impedance and select the measurement frequency to be slightly off this resonance. When the impedance at the tip changes the frequency of resonance shifts by a small amount and the change in reflection coefficient is enhanced depending on the Q-factor of the resonance (Figure 2.13).

Usually a calibration and/or model fit is done to calculate a desired measurement quantity from these reflection/transmission coefficient maps.

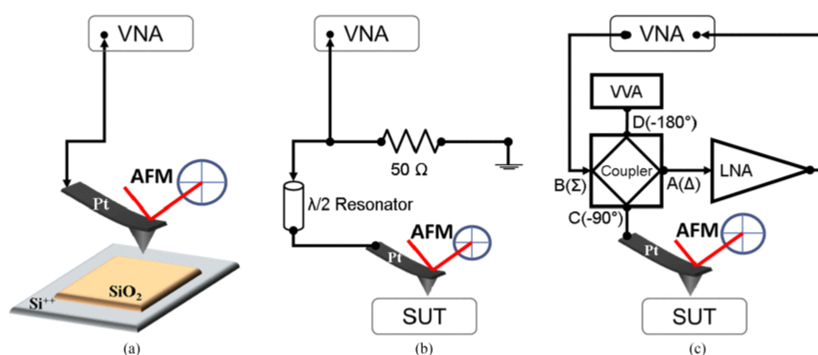

Figure 2.12: (a) Basic RF measurement setup with conductive cantilever, interfaced VNA and AFM for positioning, (b) with additional half wavelength resonator or (c) interferometer [38].

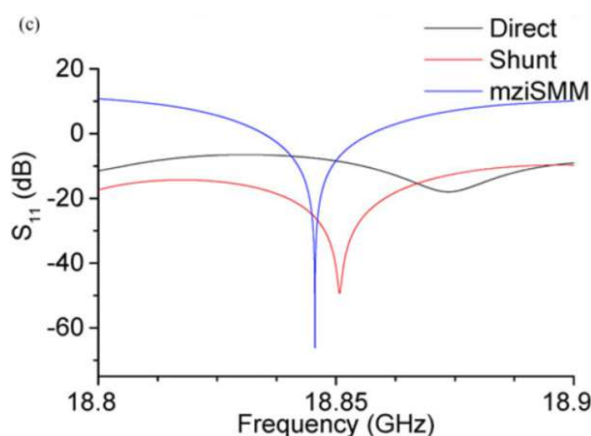

Figure 2.13: Comparision of direct, resonator and interferometric interface to VNA. (mziSMM stands for Mach Zehnder Interferometer Scanning Microwave Microscopy) [38].

Die approbierte gedruckte Originalversion dieser Diplomarbeit ist an der TU Wien Bibliothek verfügbar
The approved original version of this thesis is available in print at TU Wien Bibliothek.
TU WIEN Bibliothek Your knowledge hub

2.2.2 Scanning Microwave Microscopy (SMM)

SMM is a technique that allows the measurement of many electrical material properties on the nanoscale, even for buried structures. Recently cantilever-based probes are most commonly employed, although coaxial probes with attached tips were also frequently used in the past. When a cantilever probe is used, it is often combined with an atomic force microscope since the topographic information of the sample can be collected at the same time. One of its key features is, that it is not only limited to surface interactions like most of the other electrical measurement techniques that use the AFM platform, and can therefore be used on passivated devices (i.e. KPFM that maps surface potentials/charges [24], but has limited penetration depth).
The basic idea for SMM has already been described above. A sharp tip is in contact with (or at defined height above) a sample. The tip is connected to a VNA by a waveguide which measures the changes in the reflection coefficient at the tip to sample interface. There are many derivatives of this technique that measure different electrical properties such as Scanning Capacitance Microscopy (SCM) [39] and Scanning Microwave Impedance Microscopy (SMIM) [37]. An interferometric method or a resonant circuit as depicted in Figure 2.12 and 2.14 can be used to enhance sensitivity. Heterodyne setups can be used to extend the measurement capabilities [40].

As the name suggests the measurement is carried out in a scanning fashion and is therefore grouped with the Scanning Probe Microscopes. The lateral resolution is defined by the geometry of the tip and its distance to the sample structure that is to be measured, which is why this technique is often performed in contact to the sample surface. Imaging on the nanoscale is possible with very sharp cantilever tips in contact to structures on the sample surface. Passivation of the device surface naturally increases the measurement distance and is therefore a limiting factor.

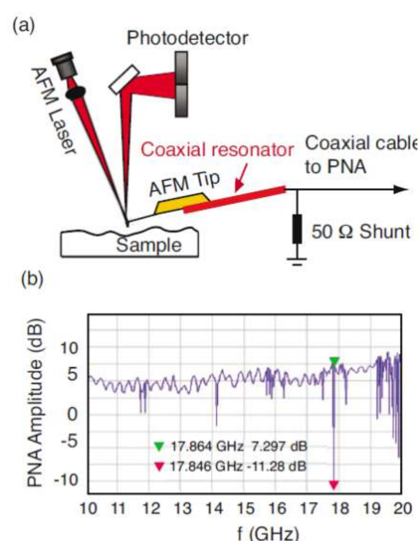

Figure 2.14: (a) Schematic drawing of the SMM setup. (b) Typical PNA frequency sweep with connected AFM. The resonance which is used for the measurements is located at f=18GHz and has a width of 2x19MHz = 38MHz and a depth of ≈18dB [41]

Die approbierte gedruckte Originalversion dieser Diplomarbeit ist an der TU Wien Bibliothek verfügbar
The approved original version of this thesis is available in print at TU Wien Bibliothek.
TU WIEN Bibliothek Your knowledge hub

2.2.3 Imaging of subsurface structures

Microwave measurements are not the only available method that can map subsurface structures, but they can be employed more easily than other popular methods, which are explained in detail in [42]. Figure 2.16 shows an overview. It is clear from the second column (maximum penetration depth reported) that any technique that features more than 100 nm of penetration is limited by the involved technology. SEM is difficult to implement, because it needs a high vacuum, has limited sample size and requires difficult sample preparation. Ultrasonic measurements usually need a coupling medium and/or must be in constant contact with the sample surface, which will degrade the cantilever tip over time. Kelvin Probe Force Microscopy (KPFM) is promising, but a maximum penetration depth of 400 nm is not enough to map features underneath a passivation layer that might exceed a micrometer. In contrast a scanning microwave microscope (SMM) setup presented in [43] can image metal lines that are buried beneath 2300 nm of dielectric via a reflection coefficient measurement as shown in Figure 2.15. Other examples of subsurface imaging using SMM can be found in [44] and [45].

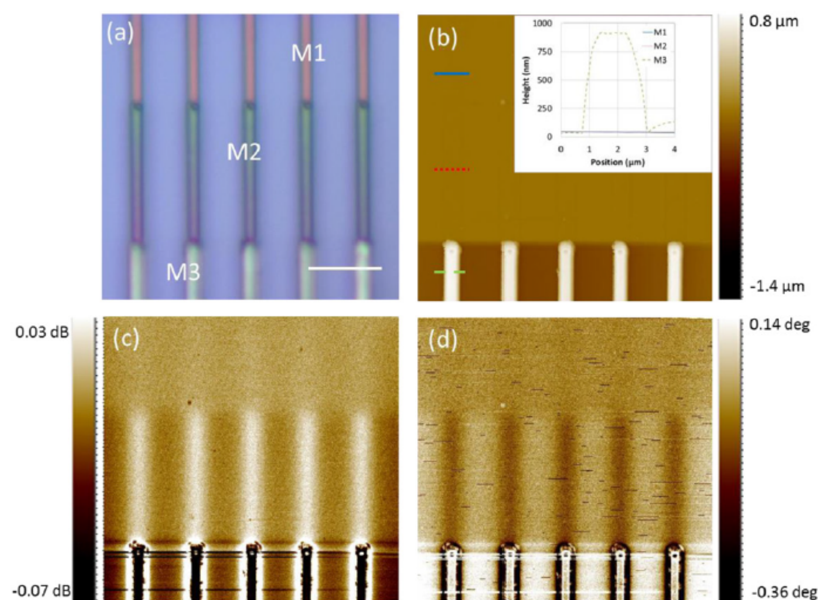

Figure 2.15: (a) Optical image of test structure, M3 bare on surface, M2 beneath 800nm of oxide, M1 beneath 2300nm of oxide, (b) AFM topography image, (c) reflection coefficient amplitude and (d) phase. First order flattening has been applied to images (b)-(d) [43].

Die approbierte gedruckte Originalversion dieser Diplomarbeit ist an der TU Wien Bibliothek verfügbar
The approved original version of this thesis is available in print at TU Wien Bibliothek.
TU WIEN Bibliothek Your knowledge hub

Imaging method reviewed		Maximum depth penetration reported	Best reported subsurface lateral resolution	Physical quantity measured	Mechanism of subsurface contrast formation
Optical (s-SNOM and TERS)		~100 nm	<30 nm	Backscattered light from the tip apex region	Both amplitude and phase changes due to local changes in dielectric properties
SEM		Up to few μm	~10 nm	Secondary electrons emitted from the sample	Positive or negative charge accumulation in subsurface interface causing changes in electric field between sample and detector
SPM	AM-AFM	~20 nm	~10 nm	Amplitude-phase-distance curves	Indentation of the tip into the sample during tapping
	DC-biased AM-AFM	<100 nm	~100 nm	Phase lag in cantilever oscillations	Energy dissipation in the sample due to local variation in capacitance and resistance
	KPFM	400 nm	Depends on depth of features	Capacitance Gradient	Variations in the dielectric constants of the subsurface features and the matrix
	EFM	<1.6 nm	~200 nm	Electrostatic force between the probe and the sample	Variation in dielectric constant between different subsurface domains/charge accumulation in subsurface interfaces
	Ultrasonic tip excitation (UAFM, CR-FM)	165 nm	<20 nm	Variations in amplitude and phase of cantilever vibrations at or near contact resonance	Variation in stiffness between subsurface features and matrix/ indentation of tip into the sample during vibrations
	Ultrasonic sample excitation (UFM, AFAM, CR-FM)	960 nm	~5 nm	Variations in amplitude and phase of cantilever vibrations at or near contact resonance	Variation in stiffness between subsurface features and matrix/ Indentation of tip into the sample during vibrations
	Multimodal AFM	70 nm	<10 nm	Variations in amplitude and phase of the cantilever vibrations at higher flexural modes	Increased penetration of the cantilever into the sample due to excitation of higher modes
	Ultrasonic sample + tip excitation (MSAFM, HFM, SNFUH)	960 nm	<5 nm	Variations in amplitude and phase of surface acoustic standing waves resulting from nonlinear interaction between probe and sample excitations	Still Unknown: could be attributed to variation in viscoelastic properties/ internal friction/density

Figure 2.16: Overview of the maximum penetration depth and lateral resolution achieved with optical, electron and scanning porbe microscopies for subsurface imaging [42].

Die approbierte gedruckte Originalversion dieser Diplomarbeit ist an der TU Wien Bibliothek verfügbar
The approved original version of this thesis is available in print at TU Wien Bibliothek.
TU WIEN Bibliothek Your knowledge hub

2.3 Probe positioning

The spatial resolution of microwave measurements is on the same scale as the part of the probe that interacts with the sample (i.e. tip, loop or aperture) and this is the driving factor in determining the needed probe positioning accuracy. This can range from many micrometres for GSG probes to single nanometres for cantilever-based probes. Thus the positioning strategy is highly depended on the employed probe.

Lateral probe positioning is usually done manually or semi-automatically with the aid of camera setups and computer vision algorithms, especially in contact-based probing scenarios, where a landing pad or device section is directly contacted. The accuracy is within micrometres for hand positioning, using stages that can be moved with micrometre-screws, and can be less than a micrometre for camera-based automatic setups. It can become unfeasible to do this for structures in the sub-micrometer range, depending on the size of the probe and the structures to be probed, since the structure and interacting probe section are too small to reliably position in this way. Especially cantilever-based probes are difficult to position by hand, because the tip of the cantilever can be hidden beneath the cantilever beam. In applications where a lateral positioning accuracy smaller than a micrometer is necessary, it is achieved by accurately measuring the probe position during a scanning operation. Based on the results of line or area scans the final position is then calculated and matched to the measurement results. Any of the above-mentioned techniques to map a certain characteristic (i.e. topography with AFM or electrical quantities with SMM) can be used for a lateral position estimation.

Vertical probe positioning is most commonly done by driving the probe towards the sample surface until contact is detected, either by visual affirmation - GSG probes leave scratch marks, smaller probes may visually bend - or by discontinuities in a measurement quantity. Electrical contact can often be directly observed, as well as a discontinuity ("snap-in") in the measurement of the optical lever method when attractive forces overcome repulsive forces and the cantilever snaps to the sample surface. Based on this detection of contact the probe can then be retracted to a certain height, if the measurement is to be contactless or differential in the distance to the sample. Again, depending on the probe size the demanded vertical accuracy ranges from micrometres to nanometres. Bigger probes are actuated with micrometre-screws or motorized stages that often offer sub-micrometre resolutions. Cantilever-based probes are commonly used in commercial AFMs, or custom setups that employ the same actuation principles, where either the probe or the sample is positioned vertically with piezoelectric actuators that offer practically infinite resolution. The limiting factor for positioning with piezos is almost always the position sensor in a feedback control loop, or model for feed-forward control, to compensate their non-linear dynamics.

With the probes and measurement techniques presented in this chapter a defined position in all spatial dimensions can be established. Lateral positioning can be done either by topographic information and/or with scan-based measurements of electrical properties. Vertical position and material properties strongly influence the capacitive coupling between tip and sample, and therefore the impedance, which in turn influences

TU Bibliothek Your knowledge hub WIEN
Die approbierte gedruckte Originalversion dieser Diplomarbeit ist an der TU Wien Bibliothek verfügbar
The approved original version of this thesis is available in print at TU Wien Bibliothek.

reflection and transmission coefficients. Thus a lateral and vertical positioning by measurement of these coefficients is expected to be possible. But all of the presented methods need to be in contact with the sample surface at least temporarily (to define a vertical position) and often also need topographic information for lateral measurements, especially in scan-based approaches to keep the tip at a constant vertical offset, even if the quantity of interest itself can be measured contactless. This significantly limits their application in high volume measurements (probe degradation) and measurements on flat (passivated) surfaces, as well as samples where the probe itself may distort the electrical measurement.

The next chapter describes the general approach to position a probe laterally and vertically without having to contact the sample, based on changes in the reflection coefficient of a microwave measurement.

Die approbierte gedruckte Originalversion dieser Diplomarbeit ist an der TU Wien Bibliothek verfügbar
The approved original version of this thesis is available in print at TU Wien Bibliothek.
TU WIEN Bibliothek Your knowledge hub

CHAPTER 3

Proposed positioning strategy and evaluation system

This chapter discusses the general approach to reach the goals of this work, a contactless probe positioning method in all spatial dimensions based on microwave measurements, and how to verify them. First a basic setup to conduct RF measurements is discussed. Then a strategy is proposed to position the probe in all dimensions. Additionally a method of verification of this position by different measurement systems and methods are presented. An overview of the proposed measurement setup and its major system components concludes this chapter.

3.1 System description and requirements

Figure 3.1 shows a sketch of a basic RF measurement setup. A sharp, conductive tip is positioned very close to or in contact with a sample surface. This tip is connected to a RF source with a waveguide. The RF source voltage V_{RF} and the reflected voltage V_r are measured using directional couplers. The sample can be grounded, floating, at a reference potential or also excited by a different source. The tip forms a capacitor with the underlying material structure via air and/or the dielectric path to the nearest conductor (assuming it is not directly in contact with a conductive surface). Depending on the state of connection it is now possible to measure different quantities: the reflection coefficient at the tip sample interface and the transmission coefficient from each RF source to the measurement devices of V_r and V_{RF}.

The goal of this work is to develop a positioning strategy where no direct contact to the sample is permitted. Thus a fixed connection to specific structures for excitation is not possible, which is why an active probe measurement is preferred, where the reflection coefficient at the tip-sample-interface is the defining measurement quantity and no separate sample excitation with additional probes is necessary. Therefore, in this work, the sample is not connected to an extra RF source and no measurement of transmission is conducted, although a DC source is connected to provide a tip-sample

Die approbierte gedruckte Originalversion dieser Diplomarbeit ist an der TU Wien Bibliothek verfügbar
The approved original version of this thesis is available in print at TU Wien Bibliothek.
TU WIEN Bibliothek Your knowledge hub

bias that is often needed during microwave measurements. This measurement of the reflection coefficient depends on the impedance of the capacitive tip-sample interface and is a function of the geometry of the tip and sample, and the permittivity, as well as the resistivity of the involved sample materials. It is expressed as the complex relation between the measured reflected voltage V_r and the measured source voltage V_{RF}.

To be able to record these changes the reflection coefficient has to be measured accurately at high frequencies (GHz range). Typically this is done with a vector network analyser that doubles as the RF source and measurement equipment.

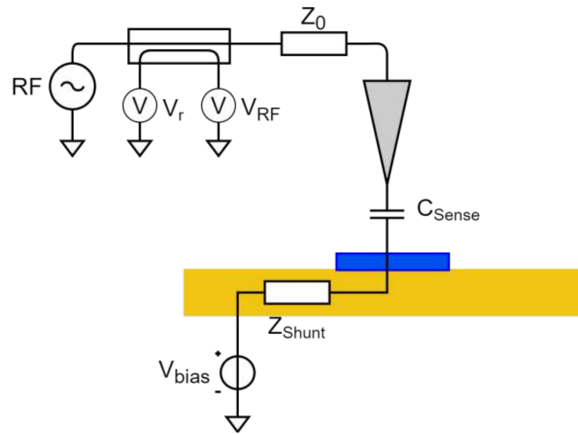

Figure 3.1: Basic RF measurement setup, a sharp tip close to the sample surface is coupled via a capacitance to the underlying materials and the reflection coefficient is measured.

3.1.1 Sample properties

Changes in the reflection coefficient are primarily caused by a change in the capacitive interface between the tip and sample and can originate from either topography changes, which directly change the distance between the tip and the sample, or material changes, under the assumption that the materials are of different permittivity. When preparing a sample it is crucial to check that both quantities (topography and permittivity) do not change in a continuous manner at the same time, since such a change in the capacitive interface cannot be clearly distinguished. The only instances in which such a combined change is allowed is when it happens at the exact same location, i.e. the beginning or end of a structure of different material. Figure 3.2 depicts all allowed changes to topography and permittivity (different colors).

An example of an allowed change is a pad buried under flat passivation (black) or a metal structure on top of bulk material, like a contact pad (blue), or a simple topographical step/slope as a result of an etching process (yellow).

Die approbierte gedruckte Originalversion dieser Diplomarbeit ist an der TU Wien Bibliothek verfügbar
The approved original version of this thesis is available in print at TU Wien Bibliothek.
TU WIEN Bibliothek Your knowledge hub

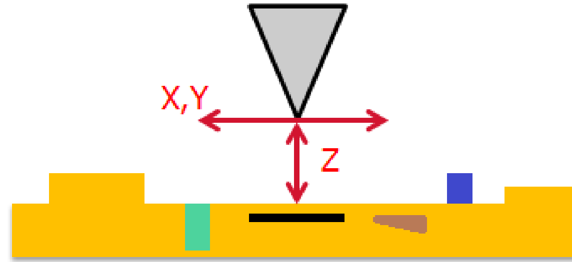

Figure 3.2: Allowed changes of material and topography. Different colours mean different materials. Changes may happen only in material OR topography. Except when they change at exactly the same time.

3.1.2 Positioning performance

The initial tip position is established manually with a camera based setup. This should place the tip within a few micrometer of the target location. After this initial positioning the tip is placed using only the RF measurement information, laterally with sub-micrometer and vertically with nanometer resolution. The positioning should be as fast as possible to enable high volume measurments and therefore the involved actuators and sensors should be neither a limitation to resolution, nor bandwidth.

To do this the system has to offer a vertical and lateral position measurement on the nanoscale. This is achieved by a stiff and compact build, to ensure that no unwanted resonances occur at lower frequencies. All axes are actuated with piezoelectric actuators, which offer high bandwidth and near infinite resolution. Driving piezos at high frequencies is difficult, since they act like a non-linear capacitor with hysteresis. The limiting factor in bandwidth for actuation is therefore the low-pass that is created by a drivers source resistance and the capacitive load of the piezo. A simple way of handling the piezos non-linearity is to use it in a feedback control loop with a position sensor. The used sensors therefore need to fulfil the nanometer resolution requirements in all axes, although the vertical axis is more critical than the lateral ones, and offer high enough bandwidth to not be the limiting factor in a control loop.

Die approbierte gedruckte Originalversion dieser Diplomarbeit ist an der TU Wien Bibliothek verfügbar
The approved original version of this thesis is available in print at TU Wien Bibliothek.
TU WIEN Bibliothek Your knowledge hub

3.2 Positioning Strategy

Controlling the reflection coefficient to a certain value at a fixed lateral position on a known material is equivalent to controlling the tip to sample distance (the vertical position), since no other property can change the capacitive interface. Therefore every different material has a certain tip to sample distance assigned when scanning an area while the reflection coefficient is controlled to a fixed value. Figure 3.3 shows a sketch of the expected change in vertical tip position when scanning over different materials while controlling the reflection coefficient to a certain target value. This information can directly be used for a lateral positioning.

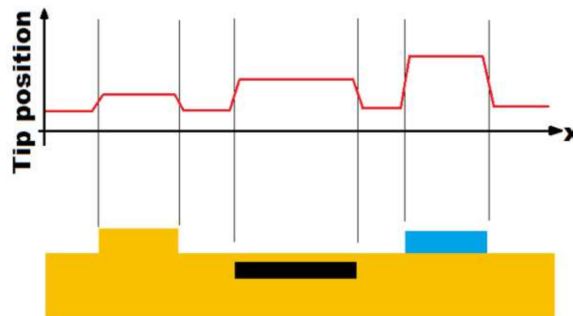

Figure 3.3: Expected change of tip position depending on material and topography changes. Topography changes (without material changes) should map directly and material changes should map according to calibration.

3.2.1 Calibration of materials

The first task of the proposed strategy is to record a calibration curve that maps the reflection coefficient over the tip to sample distance for different material compositions. It is expected that the reflection coefficient increases for larger distances, since a greater distance means worse capacitive coupling and the cantilever acts as an open end to the connecting waveguide, which would mean close to ideal reflection. With increasing distance the resolution of the measurement should also get worse, because the assumption that only the sharp tip has meaningful interaction with the local sample surface no longer holds. Therefore a non-linear connection between the tip to sample distance and the measured reflection coefficient is expected. The calibration is done on sample areas that can be safely reached with just a camera-based coarse positioning and that are large enough that coupling to different materials at greater tip to sample distances can be neglected. Assuming single micrometer uncertainty in the camera-based positioning and up to a few micrometre possible vertical separation, such an area should be many square micrometres in size. A large electrode, bulk substrate areas free of structures, or a large buried metal pad are exemplary choices. With such a recording each expected material has a known, unambiguous reflection coefficient-to-distance relation assigned.

The material that provides the worst capacitive interface always needs to be calibrated, to set a baseline that may not be exceeded. This determines the lowest reflection coefficient value that guarantees no contact between the tip and the sample.

Die approbierte gedruckte Originalversion dieser Diplomarbeit ist an der TU Wien Bibliothek verfügbar
The approved original version of this thesis is available in print at TU Wien Bibliothek.
TU WIEN Bibliothek Your knowledge hub

3.2.2 Vertical positioning

The vertical position can be directly controlled using the calibration curves when the material underneath the tip is known. Figure 3.4 shows the control scheme. z_d denotes the desired tip to sample distance, Γ_d the desired reflection coefficient mapped by the calibration, z the actual tip to sample distance, achieved with the piezo in a feedback loop, and Γ_m the measured reflection coefficient. The same controller can be used for material identification, if the material underneath the tip is unknown. Setting a target Γ_d results in a certain height z which can be related to the calibration curves to identify the material.

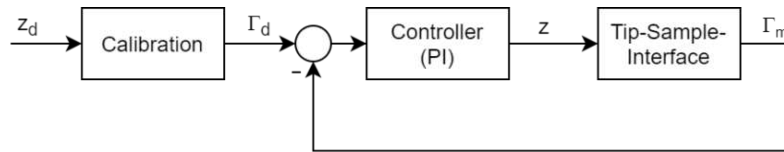

Figure 3.4: Control scheme of the vertical cantilever tip position. A calibration maps a vertical distance to a reflection coefficient.

Since the vertical positioning part of the system is part of a cascaded control scheme it also has to offer high control bandwidth. A rule of thumb is that the inner control loop (for z) has to be at least a decade faster than the outer loop (reflection coefficient). The sensors/measurement devices and bandwidth of the high voltage amplifiers required to drive piezoelectric actuators are the limiting factors. Measurements of the reflection coefficient are assumed to happen within single milliseconds. Therefore the vertical position should have a control bandwidth of a few kHz, assuming the amplifier is able to drive the capacitive load of the piezo this fast.

3.2.3 Lateral positioning

Lateral positioning is done by using the same controller, without the calibration block, to keep the reflection coefficient at a set target during a line scan. This target is chosen in such a way that the tip does not touch the surface even on the worst capacitive coupled material. Then an area of interest is scanned. The control output (tip to sample distance z) should describe either the different materials or topography steps that pass underneath the tip during the scan. This information is used to position the tip laterally at a desired location in an iterative way. A practical example would be to position the tip in the centre of a trace, which only requires one line scan. A square pad would need two perpendicular scans and if it is rotated an additional third scan in either direction is necessary. In general, more complex structures require more lateral positioning effort.

Die approbierte gedruckte Originalversion dieser Diplomarbeit ist an der TU Wien Bibliothek verfügbar
The approved original version of this thesis is available in print at TU Wien Bibliothek.
TU WIEN Bibliothek Your knowledge hub

3.3 Evaluation of position

The result of the proposed method is a well defined tip location. To verify this location another measurement system is needed. To do this an atomic force microscope (AFM) is combined with the microwave measurement. Vertical tip to sample distances can be measured by lowering the tip towards the sample until a bending of the AFM-cantilever is detected. Changes in topography can be directly mapped with an AFM in nanometer resolution to verify the lateral position for non-buried structures. Verification of the lateral position for buried structures is difficult, since another measurement principle with the same or better resolution is needed that can also penetrate a passivation layer. Additionally it would be desirable to do this with the same probe. At the present time there is no system or method that could be implemented in a compact laboratory setting that could fulfil these requirements. Instead a different measurement method is used as reference that works on the same basic principle of capacitive coupling, but uses the cantilever as a passive probe to map voltage distributions. This ensures that the presented method, with an active probe on an inactive device, can be used to position the probe for a measurement on an active device with a passive probe. Chapter 4 describes both systems in greater detail.

TU WIEN Bibliothek Your knowledge hub
Die approbierte gedruckte Originalversion dieser Diplomarbeit ist an der TU Wien Bibliothek verfügbar
The approved original version of this thesis is available in print at TU Wien Bibliothek.

3.4 System Overview

Three systems are needed to implement everything that has been discussed until now and are shown in a simplified manner in Figure 3.5.

The first system is the RF measurement system. The setup consists of a conductive cantilever that is positioned above a sample and is interfaced with a waveguide. The sample needs lateral and the cantilever vertical actuation. All axes are piezo actuated for fine positioning and have a position sensor with a resolution of single nanometers. Coarse positioning is done manually with the help of a camera.

The second system is the AFM which is used to verify the positioning strategy. It consists of a laser beam that is directed at the cantilever, which is mounted at an angle, from where it deflects onto a position sensitive detector via a mirror.

The third system is a control unit that consists of a PC which provides a user interface and is used to program a real time system that handles the necessary sensor readouts and control tasks.

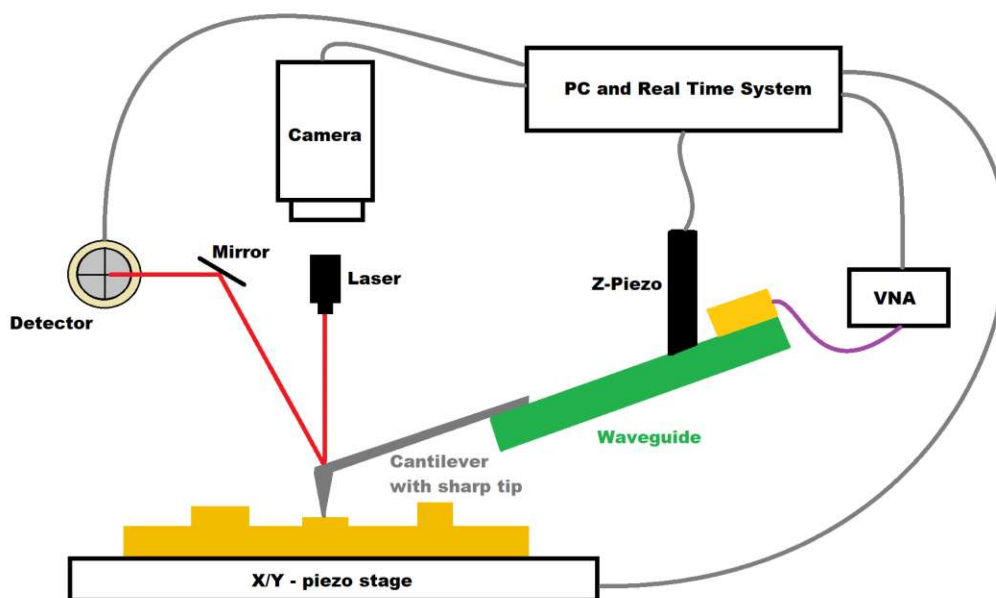

Figure 3.5: Simplifed measurement setup. A combination of AFM and RF measurements via a conductive cantliever that is interfaced to a VNA. A host PC and real time system are used for controlling the individual systems.

Die approbierte gedruckte Originalversion dieser Diplomarbeit ist an der TU Wien Bibliothek verfügbar
The approved original version of this thesis is available in print at TU Wien Bibliothek.
TU WIEN Bibliothek Your knowledge hub

CHAPTER 4

Theory

This chapter introduces the electrical background for transmission lines, waveguides and their termination, as well as a quick overview of scattering parameters and how this terminology is used in RF measurements. After that follows a short introduction on interferometry based on the method used in this work. Those are the key concepts to understand how scanning microwave microscopy works. Then the intended verification methods - atomic force microscopy and a novel approach to model based sensing of voltage distributions - are discussed.

4.1 Transmission Line Model

In classical electric engineering lengths of conductive material are often characterised as a concentrated two port model that is described by the telegrapher's equations, which are a direct result of the maxwell equations. These are a set of coupled partial differential equations that are derived by splitting the transmission line into infinitely small two port components that are described by the distributed resistance R', the distributed inductance L', distributed capacitance C' between two conductors and the distributed conductance G' of the material between the two conductors. The following equations and descriptions are, with minor adaptions, taken from the lecture scripts of "Wellenausbreitung" and "Elektrodynamik" at TU Wien [46][47] and "Microwave and RF design, Volume 2 - Transmission Lines" by Michael Steer [48]. Figure 4.1 shows the model of the infinitesimal small section of a transmission line and equation (4.1) describes the coupled partial differential equations corresponding to the model.

Die approbierte gedruckte Originalversion dieser Diplomarbeit ist an der TU Wien Bibliothek verfügbar
The approved original version of this thesis is available in print at TU Wien Bibliothek.
TU WIEN Bibliothek Your knowledge hub

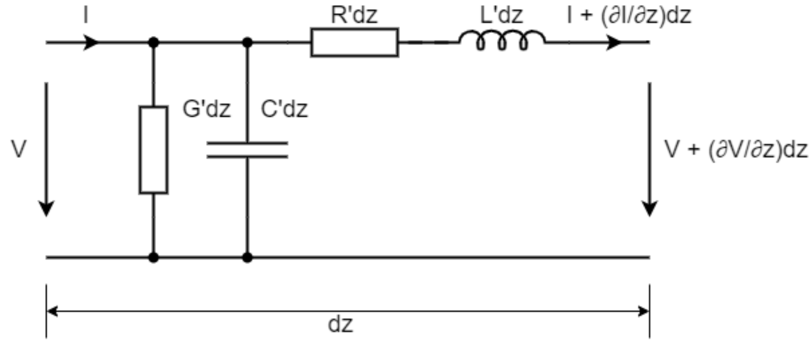

Figure 4.1: Infinitesimal small section of a transmission line

$$\frac{\partial V(z)}{\partial z} = -Z' \cdot I(z), \quad \frac{\partial I(z)}{\partial z} = Y' \cdot V(z) \tag{4.1}$$

$$Z' = (R' + j\omega L'), \quad Y' = (G' + j\omega C') \tag{4.2}$$

Those equations can be combined to have only one independent variable in each, the telegrapher's equation:

$$\frac{\partial^2}{\partial z} V(z) = Y'Z'V(z), \quad \frac{\partial^2}{\partial z} I(z) = Y'Z'I(z) \tag{4.3}$$

These are a special case of the wave equation:

$$\left(\nabla^2 - \frac{1}{c^2}\partial_t^2\right)\omega = -f \tag{4.4}$$

where we limit to one spacial dimension and the homogenous case:

$$\left(\partial_z^2 - \frac{1}{c^2}\partial_t^2\right)V(z,t) = 0 \quad \left(\partial_z^2 - \frac{1}{c^2}\partial_t^2\right)I(z,t) = 0 \tag{4.5}$$

and look only the at steady state of sinusoidal signals to eliminate the time dependency:

$$V(z,t) = \Re[\underline{V}(z)\sqrt{2}e^{j\omega t}], \quad I(z,t) = \Re[\underline{I}(z)\sqrt{2}e^{j\omega t}] \tag{4.6}$$

The underlines for complex numbers are neglected for easier readability. Substituting equation (4.6) into equation (4.5) results in equation(4.3) and with the propagation constant (α as attenuation and β as change of phase):

$$\gamma = \alpha + j\beta = \sqrt{Z'Y'} = \sqrt{(R' + j\omega L')(G' + j\omega C')} \tag{4.7}$$

a possible solution to equation (4.3) is:

$$V(z) = V_f e^{-\gamma z} + V_r e^{\gamma z}, \quad I(z) = I_f e^{-\gamma z} + I_r e^{\gamma z} \tag{4.8}$$

Where the indices f denote a forward propagating wave (away from the source) and r a backwards propagating wave (towards the source) and the solution is the superposition

Die approbierte gedruckte Originalversion dieser Diplomarbeit ist an der TU Wien Bibliothek verfügbar
The approved original version of this thesis is available in print at TU Wien Bibliothek.
TU WIEN Bibliothek Your knowledge hub

of these two waves at any given point along the transmission line.

Another important parameter of a transmission line is its characteristic impedance:

$$Z_0 = \frac{V_f}{I_f} = \frac{-V_r}{I_r} = \frac{R' + j\omega L'}{\gamma} = \sqrt{\frac{R' + j\omega L'}{G' + j\omega C'}} \tag{4.9}$$

Let z = 0 now denote the end of the line. The superposition of the incident and the reflected wave that form the voltage and current at a generic load Z_L are:

$$V(0) = V_L = V_f + V_r, \quad I(0) = I_L = I_f + I_r \tag{4.10}$$

Since voltage and current at any point on the line are related by Z_0 this can be rewritten to:

$$I(0) = I_L = \frac{V_f}{Z_0} - \frac{V_r}{Z_0} \tag{4.11}$$

and therefore:

$$Z_L = \frac{V(0)}{I(0)} = \frac{(V_f + V_r)}{(\frac{V_f}{Z_0} - \frac{V_r}{Z_0})} \tag{4.12}$$

Solving this for V_r results in equation 4.13 where the voltage reflection coefficient at the end of a transmission line, that is terminated with Z_L, is defined as Γ (load reflection coefficient).

$$V_r = \frac{(Z_L - Z_0)}{(Z_L + Z_0)} V_f, \quad \Gamma = \frac{V_r}{V_f} = \frac{(Z_L - Z_0)}{(Z_L + Z_0)} \tag{4.13}$$

Note that the substitution from before can also be done for $\frac{I_r}{I_f}$ which results in $-\Gamma$. There are some special cases for a line that is terminated with certain values for Z_L:

- Open circuit: no termination impedance is attached to the transmission line, it is therefore infinite. Solving for Z_L = inf results in $\Gamma = 1$, a perfect reflection of the voltage wave and a shift in 180 degrees in the current, which forces the superimposed current at the termination to be zero, as expected for infinite impedance.
- Short circuit: A perfect 0Ω termination results in Γ = -1, the voltages at the end cancel each other to zero as expected and $I_r = I_f$ so all the incident current travels back along the transmission line in phase.
- Match: the load impedance matches the characteristic impedance of the line $Z_0 = Z_L$ and Γ is zero, therefore no reflected wave exists. This is often the desired case.

Die approbierte gedruckte Originalversion dieser Diplomarbeit ist an der TU Wien Bibliothek verfügbar
The approved original version of this thesis is available in print at TU Wien Bibliothek.
TU WIEN Bibliothek Your knowledge hub

4.2 Waveguides

In this work two special waveguides are used. Waveguides are an abstraction of the presented transmission line where any kind of structure that can satisfy the time independent wave equation (Helmholtz equation) may be used to guide an electromagnetic wave along a given path (in all spatial dimensions). They are constrained by boundary conditions and can support different modes of propagation at different frequencies. The first is a coaxial cable where the assumption of R' = G' = 0 is made for easier calculation. L' can be calculated via the magnetic vector potential difference to:

$$L' = \frac{\mu}{2\pi} ln \left(\frac{D}{d}\right) \tag{4.14}$$

and C' by integrating over the electric field from the inner to the outer conductor to:

$$C' = \frac{2 \cdot \pi \cdot \epsilon}{ln \left(\frac{D}{d}\right)} \tag{4.15}$$

which together forms the characteristic impedance of the coaxial cable to:

$$Z_0 = \frac{1}{2\pi} \cdot \sqrt{\frac{\mu}{\epsilon}} \cdot ln \left(\frac{D}{d}\right). \tag{4.16}$$

This impedance is defined by the diameters d of the inner and D of the outer conductor and the dielectric material in between. These cables often come with a characteristic impedance of $50\,\Omega$ or $75\,\Omega$. Depending on the geometry the coaxial waveguide can carry the transverse electric magnetic mode (TEM, all frequencies) and transverse electric (TE), as well as transverse magnetic (TM) modes, at higher frequencies. It is usually operated under the cut-off frequency of the TE_{11} mode which is the first higher mode. This is also where the frequency limitations of the different connectors that were presented in Chapter 2 originate.

The second waveguide is used to guide the electromagnetic wave from the coaxial connector on the RF-PCB to the cantilever. This is a Grounded Coplanar Waveguide (GCPW). The structure is shown in Figure 4.2.

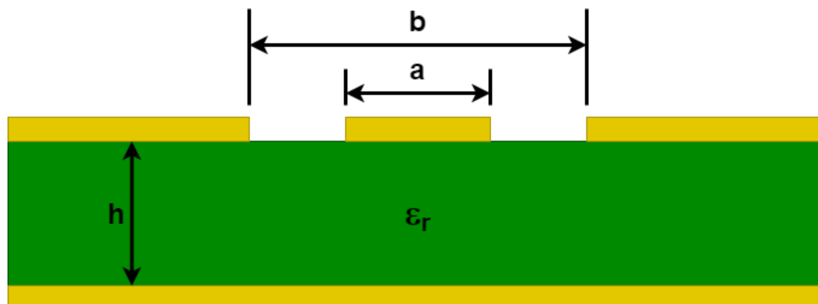

Figure 4.2: Grounded coplanar waveguide structure. Gold is conductor material and green is dielectric.

Die approbierte gedruckte Originalversion dieser Diplomarbeit ist an der TU Wien Bibliothek verfügbar
The approved original version of this thesis is available in print at TU Wien Bibliothek.
TU WIEN Bibliothek Your knowledge hub

Calculating this waveguide's characteristic impedance is a lot harder. Most of the calculators found on the internet or in dedicated programs use the equations that are presented in the "Transmission Line Design Handbook" by Brian C. Wadell [49] and "Coplanar Waveguide Circuits, Components and Systems" by Rainee N. Simons [50]. The characteristic impedance Z_0 is in these books defined for a quasi-static TEM propagation mode as:

$$Z_0 = \frac{60\pi}{\sqrt{\epsilon_{eff}}} \frac{1}{\frac{K(k)}{K(k')} + \frac{K(k_1)}{k_1'}} \tag{4.17}$$

$$k = \frac{a}{b}, \quad k_1 = \frac{tanh\left(\frac{\pi \cdot a}{4h}\right)}{tanh\left(\frac{\pi \cdot b}{4h}\right)} \tag{4.18}$$

$$k' = \sqrt{1-k^2}, \quad k_1' = \sqrt{1-k_1^2} \tag{4.19}$$

$$\epsilon_{eff} = \frac{1 + \epsilon_r \frac{K(k')}{K(k)} \frac{K(k_1)}{K(k_1')}}{1 + \frac{K(k')}{K(k)} \frac{K(k_1)}{K(k_1')}} \tag{4.20}$$

K(k) is the complete elliptic integral of the first kind, a is the track width, b = (a + gaps) and h the thickness of the dielectric.
The dimensions used in this work to achieve a 50 Ω GCPW are a track width of 590 μm, 100 μm gaps and 406 μm dielectric thickness with an ϵ_r of 3.55.

4.3 Scattering Parameters

Scattering parameters or S-parameters describe the ratio of backward and forwards propagating waves at a port of a system in amplitude and phase. Figure 4.3 shows a two port network and equation (4.21) describes the S-Matrix. S_{XY} is the complex relation between the exiting power wave b_X at port X and the incident power wave a_Y at port Y, while all ports other than Y are terminated with the characteristic impedance of the network.

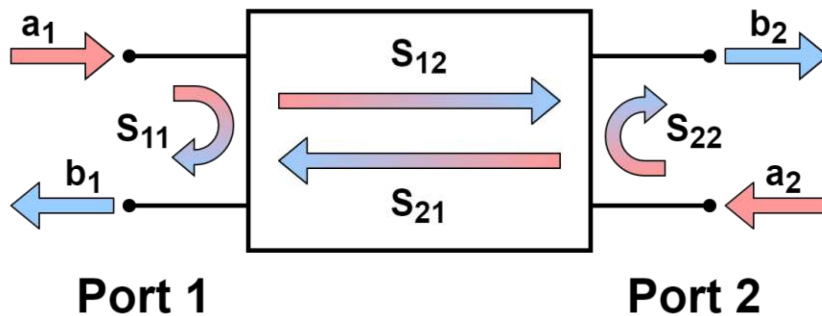

Figure 4.3: Schematic of a two port S-Parameter measurement.

$$\begin{bmatrix} b_1 \\ b_2 \end{bmatrix} = \begin{bmatrix} S_{11} & S_{21} \\ S_{21} & S_{22} \end{bmatrix} \begin{bmatrix} a_1 \\ a_2 \end{bmatrix} \tag{4.21}$$

Die approbierte gedruckte Originalversion dieser Diplomarbeit ist an der TU Wien Bibliothek verfügbar
The approved original version of this thesis is available in print at TU Wien Bibliothek.
TU Wien Bibliothek Your knowledge hub

4.4 Vector Network Analyser measurement principle

The main measurement system in this work is a vector network analyser:

"Vector network analyzers (VNAs) are test instruments that measure electrical network parameters. They are essential for radio frequency (RF) and microwave component analysis of various passive and active devices including filters, antennas, and power amplifiers. A network analyzer conducts component characterization tests. Network analyzers provide calibrated stimulus signals to the RF network or device under test (DUT) and measure the vector response over the frequency with phase and amplitude information. A VNA captures transmission (transmission coefficient, insertion loss, gain), reflection (reflection coefficient, VSWR, return loss), and impedance measurements, as well as the s-parameters S11, S12, S21, S22." - Keysight Techologies FAQ (https://www.keysight.com/gb/en/products/network-analyzers.html)

Figure 4.4 shows the internal functional setup of a generic two port VNA. The concept is based on a superheterodyne receiver. A RF-source drives one of the test ports at a time. Part of this driving power is coupled out to a mixer with a directional coupler and is there mixed with the signal of a tuneable local oscillator (LO) which produces a signal with two superimposed oscillations $f_{RF} + f_{LO}$ and $f_{RF} - f_{LO}$. The signal is then low pass filtered to cut off the higher frequency part. This down conversion can involve many mixer stages and the resulting fixed intermediate frequency (IF) signal is then filtered with a narrowband filter, amplified and sampled. The sampled signal is then processed provide amplidute and phase information of the measured voltages. The signal is mixed again with another LO signal at the intermediate frequency and a 90 degree phase shifted version of it, which are low pass filtered again to produce typical IQ (in-phase and quadrature) signals that are used to determine $amplitude = \sqrt{I^2 + Q^2}$ and $phase = arctan(\frac{Q}{I})$ of the signal. The same process is done at all relevant measurement ports while switching the source from port to port.

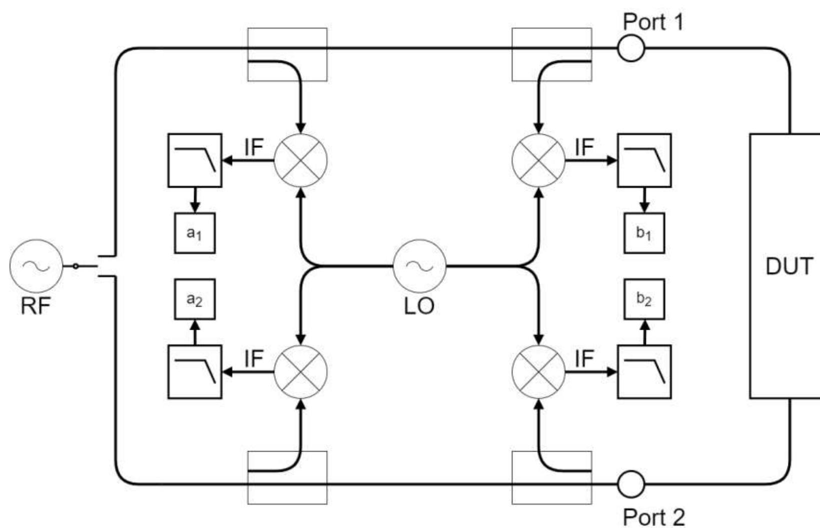

Figure 4.4: Simplified block diagram of a 2-Port VNA measurement.

Die approbierte gedruckte Originalversion dieser Diplomarbeit ist an der TU Wien Bibliothek verfügbar
The approved original version of this thesis is available in print at TU Wien Bibliothek.
TU WIEN Bibliothek Your knowledge hub

Any physical component between a VNA port and the load/DUT, i.e. a cable, can be described as a two port network as schematically shown in Figure 4.5. The last component/network in this series is terminated with the load reflection coefficient:

$$\Gamma_{L,n} = \frac{(Z_L - Z_{0,n})}{(Z_L + Z_{0,n})} \tag{4.22}$$

The input reflection coefficient $\Gamma_{in,n}$ of this last two port network can be written as:

$$\Gamma_{in,n} = S_{11} + \frac{S_{12}S_{21}\Gamma_{L,n}}{1 - S_{22}\Gamma_{L,n}} \tag{4.23}$$

The same can be done for every component in the path from the load back to the VNA port where the final input reflection coefficient $\Gamma_{in,1}$ is measured. If one can assume ideal cables, connectors and waveguides then $\Gamma_{in,1} = \Gamma_{L,n}$, because all characteristic impedances are ideally matched and there are no reflections except at the load, so all S_{11}'s and S_{22}'s are zero and all S_{12}'s and S_{21}'s are one. This is of course not the case in a real system, but many VNAs feature post processing aids that can remedy this issue in the form of a calibration. Such a calibration shifts the plane of reference to a desired point in the interconnecting parts, i.e. the end of a cable or waveguide element. This works under the assumption that the path to this reference plane can be described as a static relation at a given frequency.

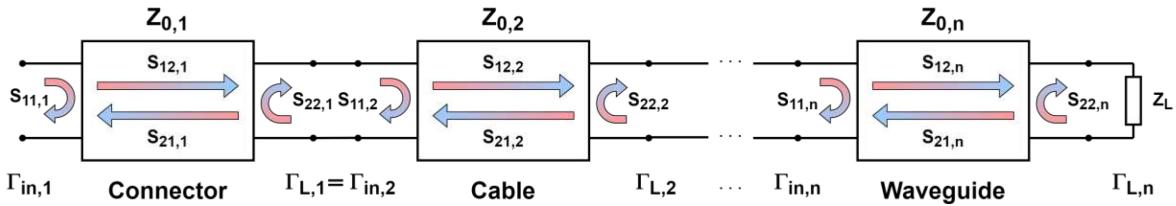

Figure 4.5: Input reflection coefficient of a series of two port networks that is terminated with a generic load.

4.5 Interferometric RF measurements

Interferometry is a measurement method that uses interference of two or more waves to gather information about differences in the path that the waves have travelled. This is commonly expressed in a phase shift between the waves that causes constructive or destructive interference, meaning that the waves at the measurement location are either adding up or are cancelling each other out. A measurement device that uses this principle is called Interferometer. It is a versatile and widely spread technique with many applications.

In this work a Michelson Interferometer is used to enhance the sensitivity of a Scanning Microwave Microscope. A Michelson Interferometer is typically used in optics and is shown in Figure 4.6 with a laser setup, but the principle works with all types of waves (optical, mechanical, electromagnetic, etc.). It features a single source that emits a wave to a component that splits the incident wave into two equal parts and sends them

Die approbierte gedruckte Originalversion dieser Diplomarbeit ist an der TU Wien Bibliothek verfügbar
The approved original version of this thesis is available in print at TU Wien Bibliothek.
TU WIEN Bibliothek Your knowledge hub

along two different paths. At one end of those paths one of the split waves interacts with a perfect reflector and travels back to the splitter. The wave on the other path encounters some sort of shift on its way. This can be caused by different materials, a longer or shorter path, a not perfect reflector or other disturbances. Nevertheless it does get reflected back to the splitter and possibly encounters the same shifts again (or others if the path is not the same for back and forward propagating waves). The same component that split the wave now combines the two parts again and they interfere (add up) and are directed to a detector. Depending on the shifts that happen in the second interferometer arm the resulting wave at the detector can be anything from the original wave (no resulting shifts in phase or amplitude at the point of recombination) to no detection (180 degrees phase shift with no amplitude shift) to anything in between, especially when the loss in the paths was not the same.

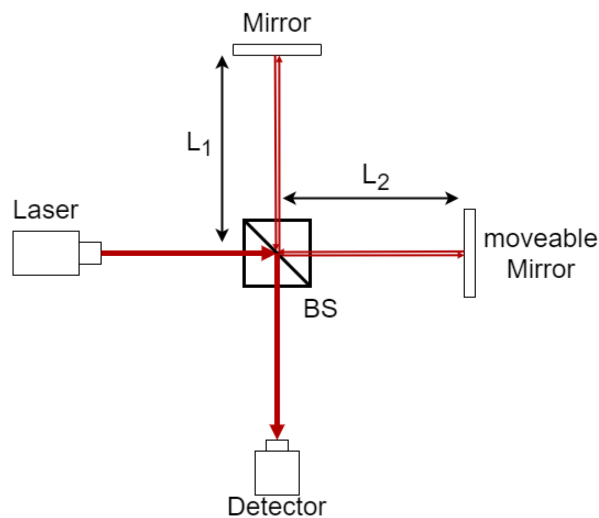

Figure 4.6: Block diagram of an optical Michelson Interferometer.

The way this technique is used in this work is that a 50:50 power splitter is connected to the single measurement port of the VNA and splits the outgoing wave. One path off the splitter ends in the measurement setup with the sharp tip and sample interface, where the reflection depends on the capacitive coupling and the materials involved, as this forms the termination of the transmission line to the interface and defines the load reflection coefficient. The other path features a phase shifter and an attenuator, which is shorted. The tip sample interface has high impedance (in relation to the characteristic impedance of 50 Ω of the transmission line) and therefore is a (not perfect) open termination. An open and a short termination of a transmission line behave basically the same, except there is a 180 degree phase shift difference between them (Γ and $-\Gamma$). The adjustable interferometer arm is tuned to cancel the two reflected waves out as best as possible at a given measurement frequency. Figure 4.7 shows an adapted image from [51] which displays this setup as it is used in this work (without the adjustable attenuator).

Die approbierte gedruckte Originalversion dieser Diplomarbeit ist an der TU Wien Bibliothek verfügbar
The approved original version of this thesis is available in print at TU Wien Bibliothek.
TU WIEN Bibliothek Your knowledge hub

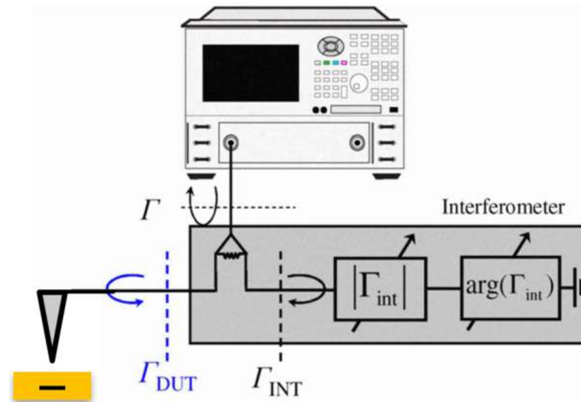

Figure 4.7: Interferometric setup in this work with a power splitter and phase shifter. Adapted grapic from [51]

4.6 Atomic Force Microscopy

Atomic Force Microscopy (AFM) is a measurement technique to map the topography of a given sample. The basic setup is shown in Figure 2.14. It consists of a reflective cantilever with a sharp tip that is in contact with a sample surface. A laser is focused on the front end of the cantilever and deflected to a position sensitive optical detector, usually a four quadrant photo detector. When the tip is scanned over the sample surface and topography changes, the cantilever has to bend to accommodate this change. The bending results in a shift in the deflected laser beam that can be detected in the vertical axis of the detector. In the same manner different surface roughness cause different twists in the cantilever that are recorded on the horizontal axis of the detector.

The sample or the cantilever is usually mounted on a piezoelectric actuator (piezo) that controls the force with which the cantilever tip is pressed onto the surface. A controller keeps the vertical deflection signal at the optical detector constant by either moving the sample or the cantilever, depending on which of the two is actuated. The controller signal then mirrors the topography and the force between tip and sample is kept constant. Another method to do this is to oscillate the tip at the cantilevers mechanical resonance and demodulate the resulting deflection oscillation with a lock-in-amplifier. The amplitude and phase can then again be used to control the piezo and measure topography. The topographic information is used in this work to implement a lift mode, where the tip is scanned along the surface once to measure topography and again at a constant distance from the surface, and for verification of the RF tip positioning.

The control output mirrors the topography, but the controller has a limit on how fast it can track an error between the deflection target and the increase or decrease in the actual deflection signal caused by sudden topography changes. Topography information is only correct where the control error is zero, or sufficiently low. This is the reason why a careful choice of scanning speed is important. The controller has a limited bandwidth and thus needs a minimum time, depending on the magnitude of change in topography, to react and control the error back to zero. Choosing a suitable scan

TU Bibliothek Die approbierte gedruckte Originalversion dieser Diplomarbeit ist an der TU Wien Bibliothek verfügbar
WIEN Your knowledge hub The approved original version of this thesis is available in print at TU Wien Bibliothek.

speed is not only crucial in AFM, but all SPM measurements, where a measurement quantity is controlled to provide information about the sample, since higher scanning tip velocities can be too fast for the error correction to complete and provide less reliable results.

4.7 Model-Based RF Voltage Sensing

A novel technique to measure voltage distributions in active devices without the need to directly contact the active part of a device is presented in [53] and used in this work as a reference to judge the quality of the final contactless lateral positioning method. It uses differential RF voltage measurements to map voltage distributions of passivated active devices with high resolution and accuracy.

The core concept is that the conductive cantilever is used as a passive probe and the device is excited by the VNA via a GSG-Probe. The method presented in [53] uses the tip sample distance relation to the involved capacitive coupling to fit a non-linear capacitance model, that can be used to calculate the voltage distribution across the device. For this, at every point in the measurement plane, the cantilever tip is moved towards the sample until contact is detected and then retracted again. Along this surface approach the S_{12} parameter is recorded (transmission coefficient between the active device area and the passive probe). It is then fitted to a non-linear capacitance model. Equation (4.24) describes the measured voltage U_m over the measurement distance z, that consists of a constant part U_0, a linear part U_l and a non-linear part U_n. The capacitance model is described in Equation (4.25). C_c is a constant and R_{eff} is an effective tip size, d denotes the passivation thickness and ϵ_r the relative permittivity of the passivation:

$$U_m(z) \propto C_{1,n}(z) \cdot U_n + z \cdot U_l + U_0 \tag{4.24}$$

$$C_{1,n}(z) = C_c \cdot ln\left(1 + \frac{R_{eff}}{z + \frac{d}{\epsilon_r}}\right) \tag{4.25}$$

The advantage over similar techniques that measure absolute values or differential between two points is, that the long range linear part U_l (coupling to the cantilever beam/cone) can be eliminated. This reduces crosstalk and enhances sensitivity for the non-linear part U_n, which represents only the local sample interactions with the tip.

Figure 4.8 shows two corresponding transmission coefficient S_{12} measurements, where a metal pad beneath 500 nm of passivation is excited with 26 GHz, one on the pad (blue) and one 3 μm off the pad on grounded bulk silicon (red).

Die approbierte gedruckte Originalversion dieser Diplomarbeit ist an der TU Wien Bibliothek verfügbar
The approved original version of this thesis is available in print at TU Wien Bibliothek.
TU WIEN Bibliothek Your knowledge hub

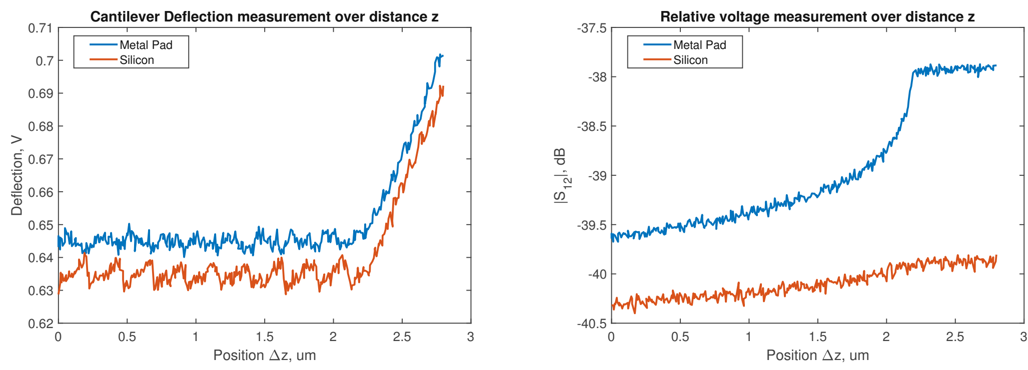

Figure 4.8: (a) Deflection measurement and (b) transmission coefficient magnitude $|S_{12}|$ measurement over the position z with the passive probe on a metal pad and silicon, 3 μm beside the pad.

Die approbierte gedruckte Originalversion dieser Diplomarbeit ist an der TU Wien Bibliothek verfügbar
The approved original version of this thesis is available in print at TU Wien Bibliothek.
TU Bibliothek Your knowledge hub WIEN

Die approbierte gedruckte Originalversion dieser Diplomarbeit ist an der TU Wien Bibliothek verfügbar
The approved original version of this thesis is available in print at TU Wien Bibliothek.
TU WIEN Bibliothek Your knowledge hub

CHAPTER 5

Implementation

This chapter discusses the implemented measurement setup and its components in detail.

5.1 System Overview

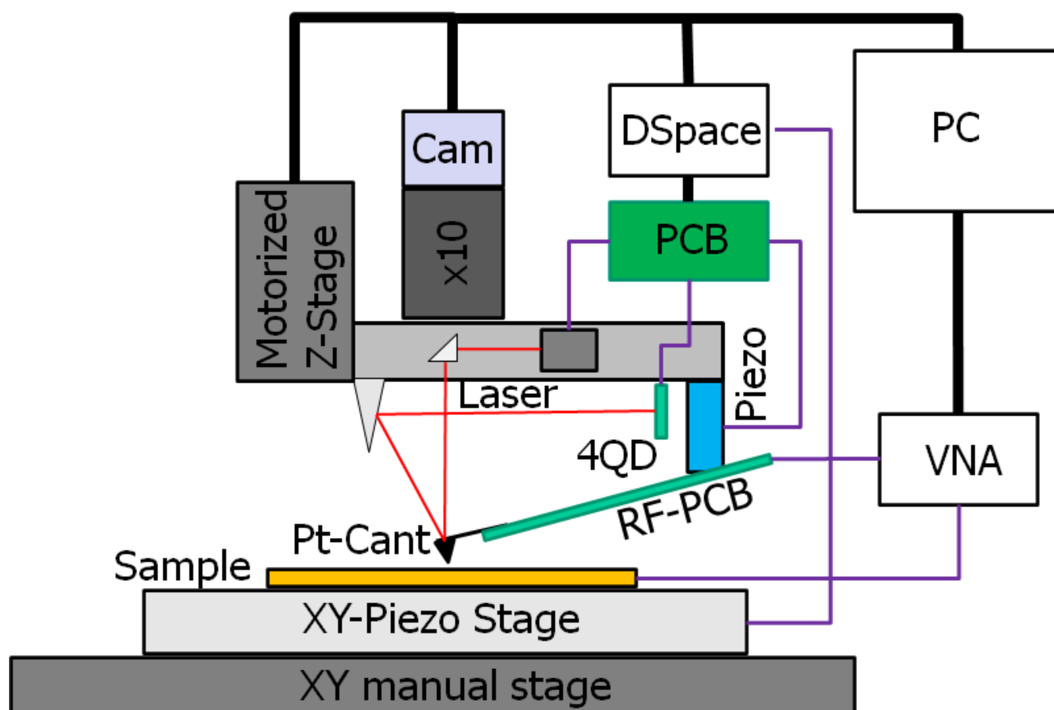

Figure 5.1: Block diagram of the developed test setup.

Figure 5.1 shows a block diagram of the implemented system. The measurement sample or DUT is placed on a 3D-printed sample holder, which is mounted on an piezoelectrically actuated dual axis stage (NPoint NPXY100-100) for fine lateral positioning and is magnetically held in place. This stage features a maximum 100 μm travel in both axes and is driven by a commercial controller (NPoint LC402). This controller also provides the lateral position measurement to the central real time system (DSpace MicroLabBox) which in turn provides the reference position input for the stages. Amplification to the high voltages that are needed for the piezoelectric actuation of the stages is done by the controller. The NPoint stage is mounted on two manual stages that provide lateral coarse positioning via micrometer screws with an overall travel range of 25 mm (Thorlabs M1). A conductive cantilever with a long tip (Rocky Mountain Nanotechnology 25Pt300C) acts as a probe slightly above the sample. A SEM image of the cantilever is shown in Figure 5.2.

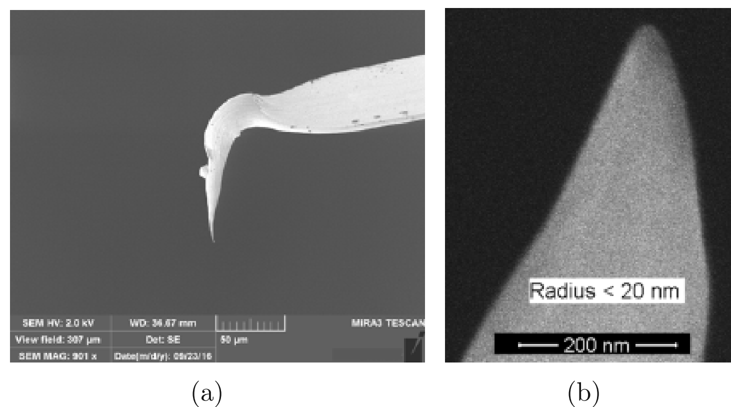

(a) (b)

Figure 5.2: (a) SEM images of the whole conductive cantilever with long tip [54] and (b) of its tip[1].

The cantilever is fixed onto an RF-PCB which acts as a grounded coplanar waveguide with a characteristic impedance of 50 Ω, shown in Figure 5.3. The RF-PCB is connected via SMA to a VNA (Rohde and Schwarz ZNA26 4-Port).

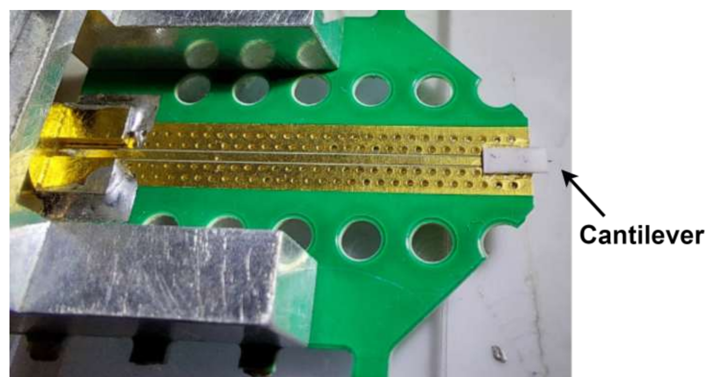

Figure 5.3: RF-PCB with SMA connector, waveguide and cantilever chip.

[1] https://storage.googleapis.com/wzukusers/user-34656922/images/5c5af10b7b7ba4rcmQWG/rmnano3_d400.PNG

Die approbierte gedruckte Originalversion dieser Diplomarbeit ist an der TU Wien Bibliothek verfügbar
The approved original version of this thesis is available in print at TU Wien Bibliothek.
TU Bibliothek Your knowledge hub WIEN

Vertical fine positioning of the RF-PCB, and thus the cantilever tip, is done by flexure guided piezo actuation (Thorlabs PC4WMC2) as shown in Figure 5.4. The vertical position is measured with four strain gauges in a full bridge configuration mounted on the sides of this piezo.

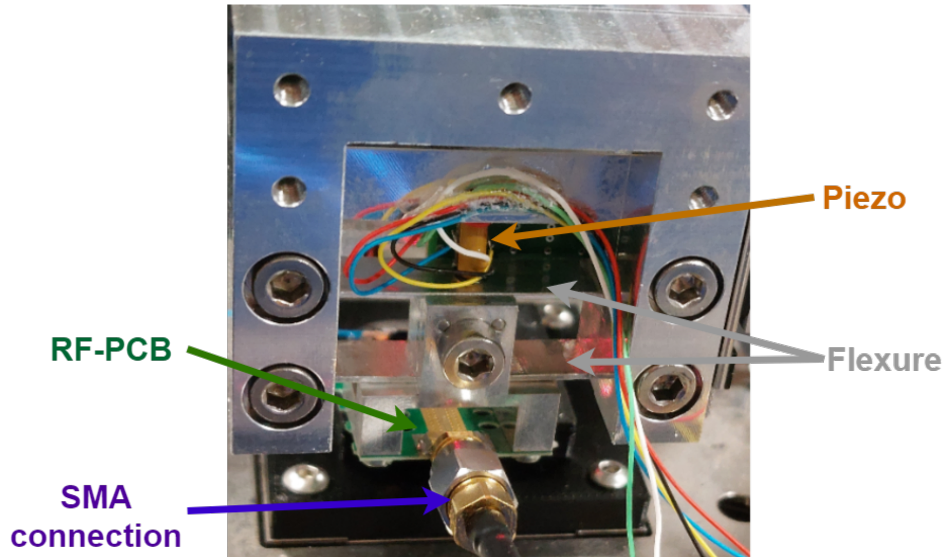

Figure 5.4: Flexure with piezoelectric actuator and screwed on RF-PCB.

The custom AFM utilizes the laser module of a Bruker Multimode 8 measurement head on an aluminium mount and is shown in Figure 5.5. It consists of a laser diode (Thorlabs LP637P5) with a collimator and adjustable focus lenses. The emitted laser beam is deflected by a 90 degrees mirror to the cantilever where it is deflected to a freely adjustable mirror, which deflects the beam onto a four quadrant photo detector (QPD, First Sensor QP5.8-6-TO5). The QPD is mounted on, and moved vertically with, a miniature manual stage (Edmund Optics Micro Series B). The laser module can be tilted by two screws to aim the laser beam at the front of the cantilever.

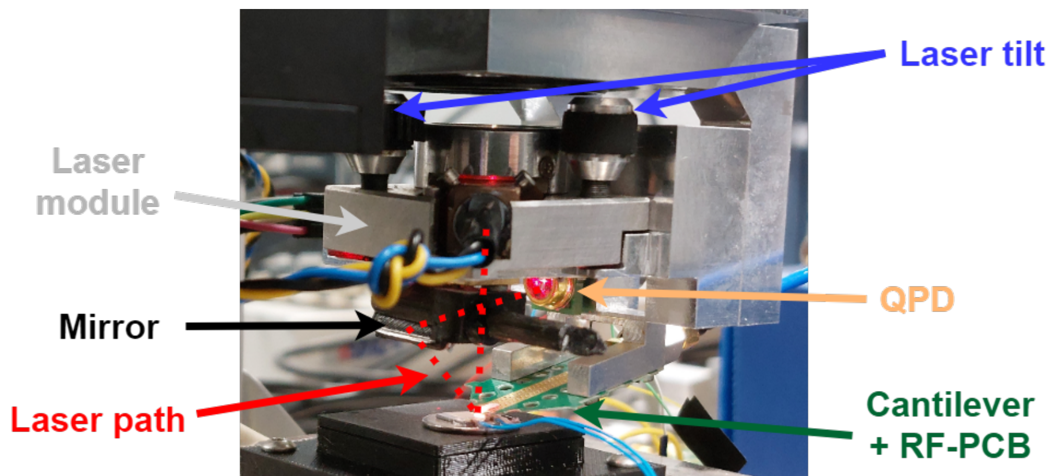

Figure 5.5: Assembly of the AFM measurement head.

Die approbierte gedruckte Originalversion dieser Diplomarbeit ist an der TU Wien Bibliothek verfügbar
The approved original version of this thesis is available in print at TU Wien Bibliothek.
TU WIEN Bibliothek Your knowledge hub

The AFM head is mounted on a motorized stage (Thorlabs M1) that acts as the coarse vertical stage and is mounted on an aluminium post. A camera is positioned over the AFM head to provide visual guidance and assist in the coarse positioning of the cantilever, as well as the aiming of the laser beam. The camera is an industrial monochrome camera (The Imaging Source DKU23UM021) which is fixed to the top of a 10x objective (Sony) and connected to the PC via USB. The camera can be moved in all spatial dimensions decoupled from the rest of the system. The complete physical setup is shown in Figure 5.6.

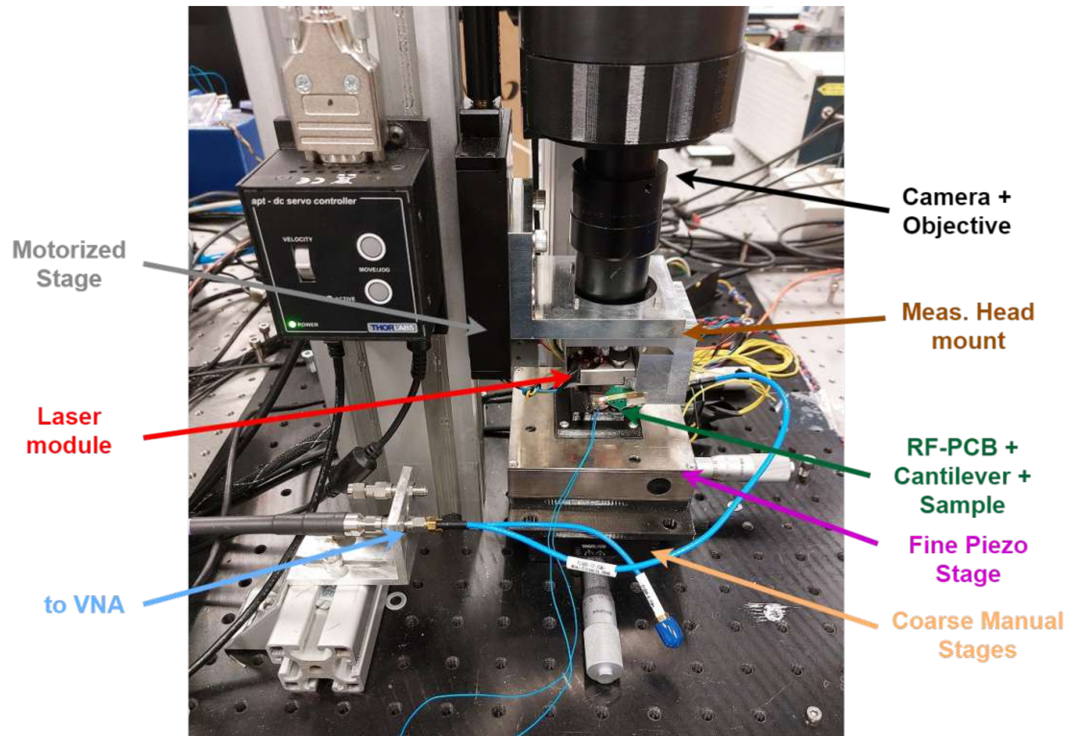

Figure 5.6: Complete physical measurement setup.

The QPD, piezo strain gauges and laser diode are connected to a custom PCB that provides driving circuitry for the laser diode and measurement circuitry for the sensors, as well as an SMA interface for all relevant signals. The motorized stage, the nPoint controller, the camera and the VNA are connected to the PC via USB. A high voltage amplifier (Falco Systems WMA-300) is used to drive the vertical positioning piezo. Since the DSpace outputs can only handle 8 mA a custom driver circuit is needed for the 50Ohm input of this amplifier.

The system is controlled primarily with a DSpace MicroLabBox real time system that is programmed via Matlab/Simulink. Control parameters for the real time system and the motorized stage are managed with a GUI that was programmed with the Matlab App Designer. That same GUI is also used to configure the VNA, to calculate measurement results and to display and save them. Figure 5.7 shows a screenshot of the GUI.

Die approbierte gedruckte Originalversion dieser Diplomarbeit ist an der TU Wien Bibliothek verfügbar
The approved original version of this thesis is available in print at TU Wien Bibliothek.
TU WIEN Bibliothek Your knowledge hub

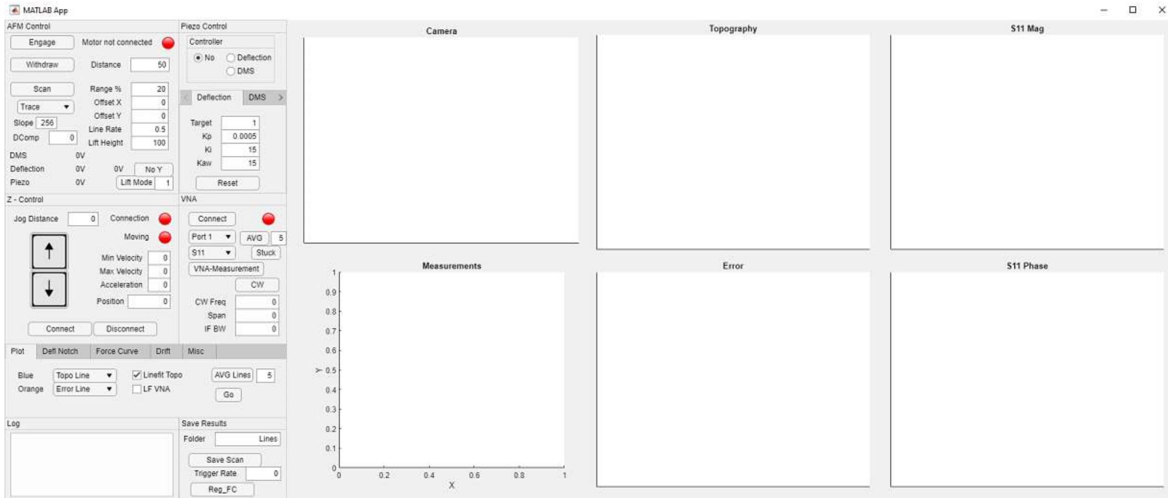

Figure 5.7: GUI to control the system and perform measurements.

5.2 Probe and VNA interface

The used probe is a platinum cantilever (Rocky Mountain Nanotechnology 25Pt300C). It has a 80 μm long tip with a tip radius of less than 20 nm. It is used because of its very long and steep conical tip, which helps to mitigate capacitive coupling of the cantilever beam to the sample. This improves the sensitivity to the local interactions at the end of the tip, which results in a better microwave measurement resolution by reducing crosstalk to surrounding structures. Careful placing of the cantilever on the RF-PCB is needed to ensure good contact between the cantilever and the 590 μm wide centre trace of the grounded coplanar waveguide. The waveguides dielectric is a high frequency, low loss material that is rated to 40 GHz (Rogers 4003c). It is 406 μm thick and the gap between the centre trace and surrounding ground is 100 μm to achieve a characteristic impedance of 50 Ohm, to minimize reflections at the SMA interface (Amphenol RF 901-10512-2) that connects to the VNA. A double row via fence helps to provide mode free propagation and a reduction of radiation loss along the PCB [55]. As seen in Figure 5.6 a panel with an adaptor connects a coaxial cable from the VNA (black) to a highly flexible cable (blue) to relief stress and to decouple the system from disturbances along the cable connection. Some of the following measurements also include an interferometric setup. This setup is placed between the panel and the RF-PCB. It consists of a power splitter (Suhner 4901.19.A) and a short terminated phase shifter (Pasternack PE8247).

5.3 Vector Network Analyser

The measurement device for all S-parameter measurements is a vector network analyser (Rohde and Schwarz ZNA26 4-Port). This analyser features a frequency range of 100 MHz to 26.5 GHz at an output power range of -80 dBm to +17 dBm. All measurements are conducted without post processing calibration. The standard settings are chosen to 1 kHz IF bandwidth for noise suppression, 26 GHz measurement frequency

Die approbierte gedruckte Originalversion dieser Diplomarbeit ist an der TU Wien Bibliothek verfügbar
The approved original version of this thesis is available in print at TU Wien Bibliothek.
TU Bibliothek WIEN Your knowledge hub

to decrease impedance when capacitive coupled and 0 dBm output power (without a power calibration). If not stated otherwise the measurements presented in this work are recorded using the Continous Wave (CW) configuration of the VNA, triggered via a digital output of the DSpace MicroLabBox.
The active, excited, physical port for all measurements is port 1 when discussing reflection coefficients (active probe), and port 2 when discussing transmissions to a passive probe on port 1. Figure 5.8 shows the two configurations (red: outgoing waves, blue: incident waves).

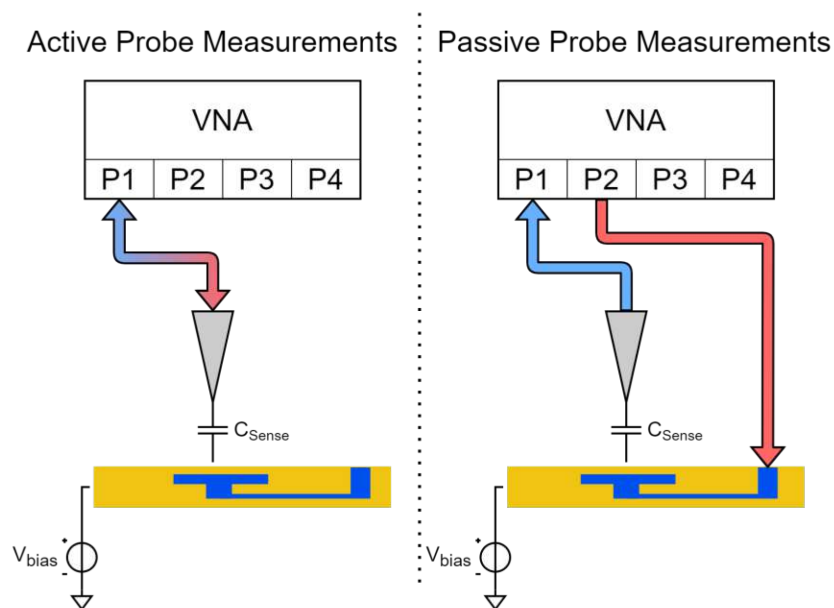

Figure 5.8: Physical VNA connections for active probe (reflection coefficient) and passive probe (transmission coefficient) measurements, red arrows depict the measured outgoing waves and blue arrows measured incident waves at the VNA ports.

Die approbierte gedruckte Originalversion dieser Diplomarbeit ist an der TU Wien Bibliothek verfügbar
The approved original version of this thesis is available in print at TU Wien Bibliothek.
TU WIEN Bibliothek Your knowledge hub

5.4 Samples

There are four main samples used throughout this work. Evaluation of topography is done on an interdigital capacitor structure. Figure 5.9(a) shows this sample and (b) shows a microscope image of the structures. The fingers structures are 200 nm thick and 5 μm wide with a 5 μm pitch. They are made of gold and are structured on a silicon bulk substrate that is conductively glued onto a stainless steel disk. Both finger rows and the bulk are on floating potential. This sample is also used for differential measurements and to test control algorithms since it features the harshest conditions of all samples, where topography and material changes drastically at the same time.

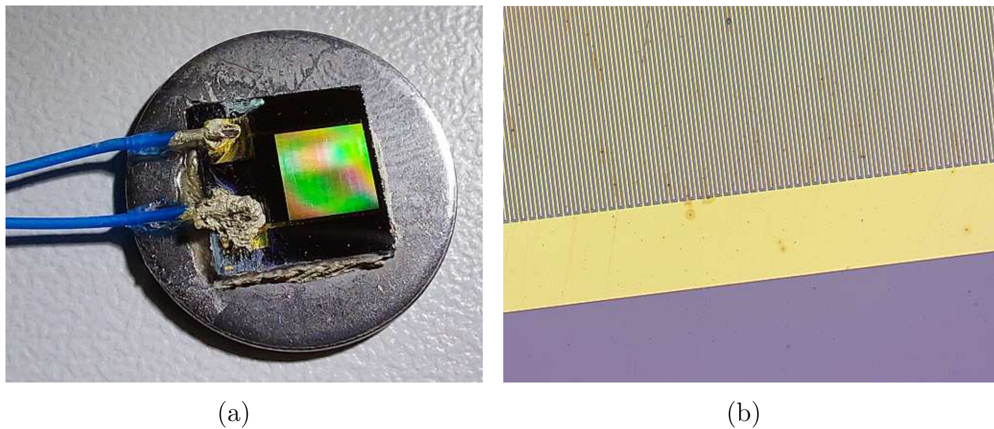

(a) (b)

Figure 5.9: (a) Interdigital capacitor sample with contact wires on stainless steel disk,(b) microscope enhanced picture of gold electrode and finger structure (yellow) on bulk silicon (purple).

Scanning Microwave Microscopy is evaluated on a dopant calibration sample from Infineon. It consists of three sections that feature stripes and p-n-junctions of different dopant concentrations and no topography except for mesa dot structures. The part used in this work are stripes of different widths and dopant concentration combinations, which are arranged in a cross-shaped manner [56] and shown in Figure 5.10.

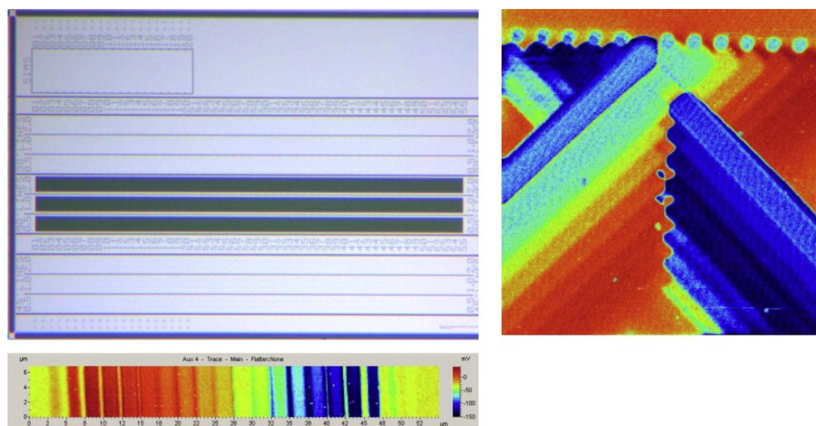

Figure 5.10: Dopant calibration sample from Infineon [56].

Die approbierte gedruckte Originalversion dieser Diplomarbeit ist an der TU Wien Bibliothek verfügbar
The approved original version of this thesis is available in print at TU Wien Bibliothek.
TU WIEN Bibliothek Your knowledge hub

The sample is also glued conductively to a stainless steel disk, which has a wire attached to define a tip-sample bias voltage. This is done because a DC bias has considerable influence on the reflection coefficient measurements on such a sample. A topographic fault is used as a landscape marker to find the same spot for measurements again. The sample is shown in Figure 5.11(a) with a microscope enhanced image in (b).

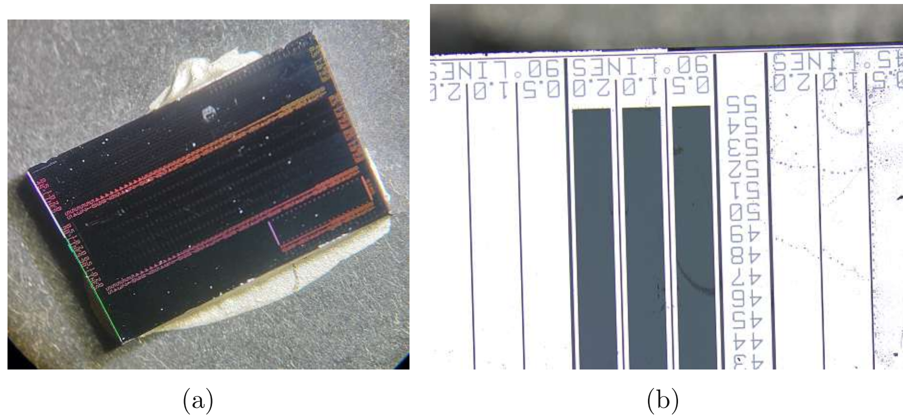

(a) (b)

Figure 5.11: (a) Dopant calibration sample on stainless steel disk,(b) microscope picture of different measurement areas.

SMM is also investigated on topographically flat samples with different metal structures buried beneath layers of passivation. Figure 5.12 shows sketches of these samples. Metal pads, a resistor structure and an interdigital capacitor are on the same sample and are connected to a landing pad to contact the shown traces. The inductor in Figure 5.12(b) is on a different sample, where the actual passivation thickness is unknown. It is used together with the Infineon sample to test and evaluate the implemented SMM.

Characterisation of differential measurements and implementation of the final measurement technique and position strategy are conducted on the samples in Figure 5.12(a) and the interdigital capacitor sample without passivation in 5.9.

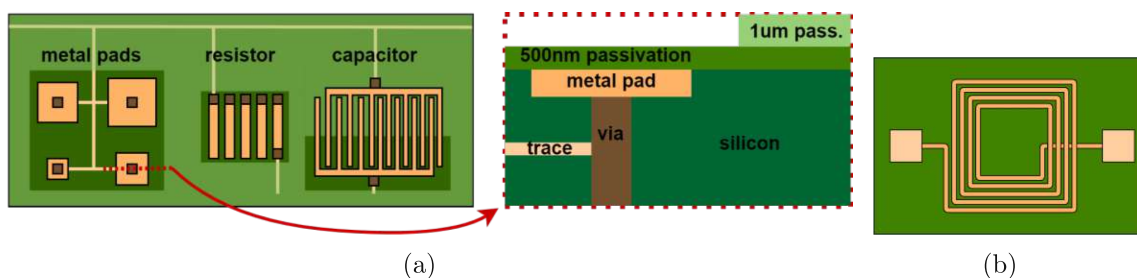

(a) (b)

Figure 5.12: Sample for tests of SMM on buried structures. (a) Metal pads of different sizes with vias in the middle (left), resistor structure with vias (middle), interdigital capacitor (right) and a cross-section of one pad. Two different thicknesses of passivation are present. (b) Metal inductor structure with contact pads on silicon beneath passivation.

Die approbierte gedruckte Originalversion dieser Diplomarbeit ist an der TU Wien Bibliothek verfügbar
The approved original version of this thesis is available in print at TU Wien Bibliothek.
TU Bibliothek WIEN Your knowledge hub

5.5 Real Time System

The real time system (DSpace MicroLabBox) is used to control all the (piezoelectrically actuated) fine stages and to trigger VNA measurements at precise locations. The main application runs at a sample rate of 30 kHz and it is programmed and controlled with a Matlab/Simulink model and can be configured during live operation via .NET libraries. These are also used to grab data from the real time system with the user application. The main functionality of this system is to control either the position signal of the strain gauges, that are attached to the vertical piezo or to control the deflection signal of the QPD, that detects a bending of the cantilever. Figure 5.13 shows the control loop. It also samples and saves all relevant signals depending on the measurement mode that is currently in use. Both controllers (strain gauge and deflection) are online tuneable PI controllers. Additionally it is responsible to generate the reference trajectory for lateral fine positioning. It also rasterizes the scanning and probing trajectories and defines and executes trigger points for VNA measurements. Signal conditioning is implemented to make the system more robust to outside influences (i.e. filters and averaging for noise suppression).

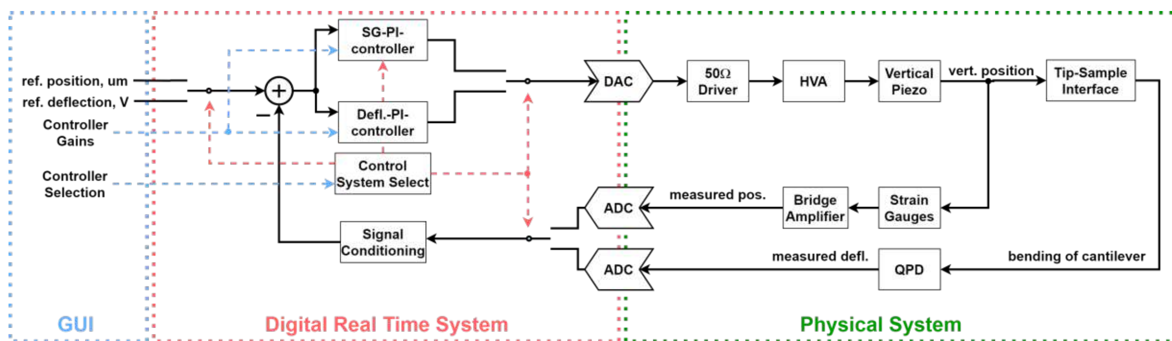

Figure 5.13: Vertical position control schemes based on strain gauge signal or cantilever deflection signal.

5.6 Sensor Characterisation

There are four signals that are monitored during operation. The vertical and lateral position, the cantilever laser deflection and the reflection coefficient at the tip to sample interface. Reflection coefficient measurements are performed by the VNA and lateral position measurement is included with the LC402 controller, so they do not need to be characterised.

The vertical position sensor is implemented in the form of four strain gauges that are glued to the vertical piezo in a full bridge configuration. An accurate measurement is necessary because piezoelectric actuators are non-linear devices that exhibit a hysteresis between the applied voltage and the piezo elongation [57]. The bridge circuit is supplied with its own channel from a laboratory power supply to minimize noise and its bridge voltage is amplified with an instrumentation amplifier (AD8429). Figure 5.14(a) shows the characterisation of the strain gauges and the amplifier. The blue curve shows

Die approbierte gedruckte Originalversion dieser Diplomarbeit ist an der TU Wien Bibliothek verfügbar
The approved original version of this thesis is available in print at TU Wien Bibliothek.
TU WIEN Bibliothek Your knowledge hub

the expected piezo hysteresis and the red curve shows the output signal of a capacitive distance probe that was targeted at the bottom of the RF-PCB fixture. It shows the expected linear relation to the strain gauges. The bridge amplifier output voltage swing is about 1.3065 V when the piezo is excited with a 140 V, 1 Hz sinusoidal signal, which is equal to 9.699 μm elongation of the piezo. The strain gauges sensitivity is therefore $9.699/1.3065 = 7.42\,\mu\text{m/V}$.

The strain gauge noise characterisation is depicted in Figure 5.14(b). The system was left unactuated and the SG signal is recorded. An overall measurement noise of $0.606\,mV_{rms}$ can be identified, which equals $4.9\,nm_{rms}$ with the sensitivity stated above. This noise is $2\,LSB_{rms}$ of the ADC which is very close to the noise floor of the real time system. The SG signal has an adjustable hardware offset via the instrumentation amplifier and is chosen to always provide a positive SG signal.

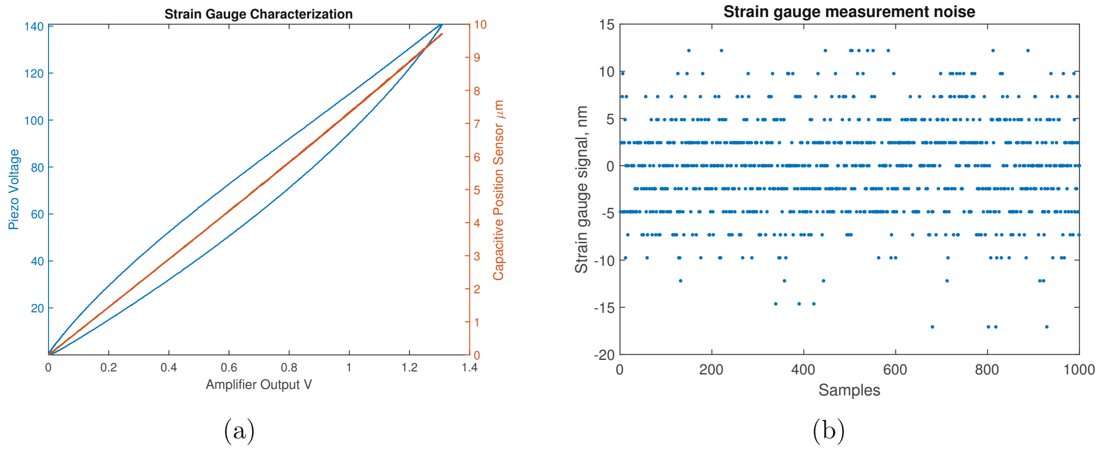

Figure 5.14: (a) Strain gauge sensitivity analysis (red) and piezo hysteresis (blue), (b) Characterisation of strain gauge noise. A $4.9\,nm_{rms}$ or $2\,LSB_{rms}$ noise level is measured.

Evaluation of the QPD is necessary to approximate the forces between the cantilever tip and the sample surface during contact. Figure 5.15(a) shows a simplified rendition of a laser beam hitting the detector. The deflection signal is calculated with the measured photocurrents $I_{A,B,C,D}$ in the horizontal X and vertical Y direction via transimpedance amplifiers and summing/subtraction amplifiers.

$$X = \frac{I_A + I_C - I_B - I_D}{I_A + I_C + I_B + I_D}, \; Y = \frac{I_A + I_B - I_C - I_D}{I_A + I_C + I_B + I_D} \tag{5.1}$$

In this work only the Y component is of interest and relates directly to a vertical bending of the cantilever. Such a bending is usually characterised with a force curve as shown in Figure 5.15(b). To record such a curve the cantilever is driven towards the sample surface until the so called snap-in is detected where attractive forces overcome repulsive forces between the tip and the sample surface. The snap-in is used in this work to determine the distance between a measurement starting position and the sample

Die approbierte gedruckte Originalversion dieser Diplomarbeit ist an der TU Wien Bibliothek verfügbar
The approved original version of this thesis is available in print at TU Wien Bibliothek.
TU Bibliothek Your knowledge hub WIEN

surface. The tip is then driven a little further, to get into the linear region of the curve, until a predefined threshold is reached. The probe is then retracted again and snaps off the surface when adhesion forces are overcome. There is a lot of information that can be extracted from such a force curve, like stiffness moduli [58] and surface adhesion properties [59], but for the characterisation only the linear region is of interest, which shows the sensitivity of the four quadrant photo detector. In this implementation the sensitivity is around 25 mV/nm, depending on the exact mirror and detector position, which changes every time a new probe is used and the laser is readjusted.

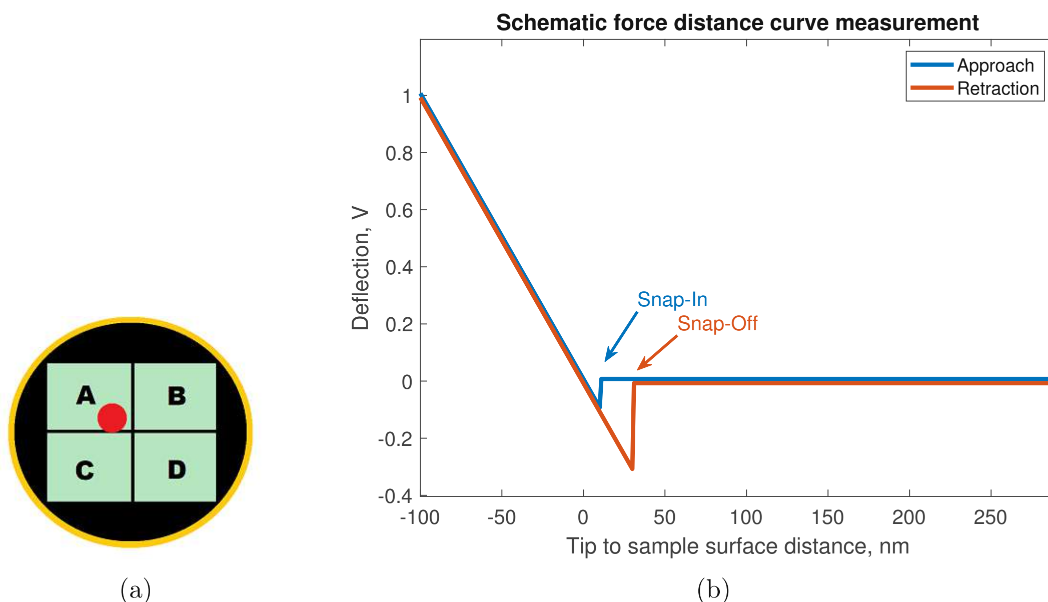

(a) (b)

Figure 5.15: (a) Working principle of a deflection measurement in AFM. The laser dot is usually larger than depicted. (b) Schematic force distance curve measurement with snap-in and snap-off.

Die approbierte gedruckte Originalversion dieser Diplomarbeit ist an der TU Wien Bibliothek verfügbar
The approved original version of this thesis is available in print at TU Wien Bibliothek.
TU WIEN Bibliothek Your knowledge hub

Die approbierte gedruckte Originalversion dieser Diplomarbeit ist an der TU Wien Bibliothek verfügbar
The approved original version of this thesis is available in print at TU Wien Bibliothek.
TU Bibliothek WIEN Your knowledge hub

CHAPTER 6

Evaluation of measurement capabilities

This chapter presents the implemented measurement modes and evaluates their performance. As a quick reminder, AFM is implemented as a reference for the lateral position and SMM is implemented as the RF measurement that should be able to penetrate passivation, characterize materials and provide position information in all spatial dimensions via a calibration.
First AFM is implemented in contact mode to have a method that can provide a precise probe location. Then SMM is implemented, also in contact mode, to get a system as it is described throughout literature. Next, SMM in lift mode is evaluated to judge the sensitivity and contrast of the measurement when the tip is no longer in contact with the sample surface, which is needed as the basis for a calibration of the reflection coefficient over the tip to sample distance. Measurement drift is identified as the main limiting factor and is discussed at the end of the chapter.

6.1 Atomic force microscope in contact mode

The AFM is the reference for all topography related changes. To that end its limitations need to be investigated. As stated in Chapter 5.6 the resolution of the strain gauges that form the Z position sensor is limited by 4.9nm rms noise. This is the noise floor under which no structures can be detected any more. The resolution an AFM provides strongly depends on several parameters such as the scanning speed, the interaction force and the maximum topographical step height that is to be measured, as well as the eigenfrequencies of the vertical positioning system and how aggressively the controller is tuned. A faster scan speed gives the controller less time to react to a change in topography. Greater magnitudes of topographic changes take longer to compensate. Higher interaction forces result in greater tracking errors which decrease the time it takes to compensate the change and faster wear of the cantilever tip. Higher controller gains also decrease the compensation time but come with reduced phase margin that can lead to ringing. All of the parameters listed together result in a

certain rate of change the controller has to provide to compensate an error before the next sample point of topography. If it cannot do this in time, then the sampled point has a residual error. Additional errors can occur if the controller is able to do this but the system itself begins to oscillate, because the rate of change is near an eigenfrequency of the mechanical system. Since AFM is an imaging technique at its core such errors might be tolerable depending on what exactly is to be imaged. Faster, inaccurate measurements can still provide useful information on the general structure of the sample even though they might be missing details that could be imaged at slower speeds.

The setup presented in Chapter 5 has many degrees of freedom and since there is no single solution and many parameters to consider when tuning an AFM. Small changes in the system can have far reaching effects and require a retuning, i.e. new cantilever at not exactly the same position, therefore realignment of the mirror, which results in different sensitivity of the QPD, that effects the PI controller gains, etc. The general tuning procedure employed is to scan on the sample with the greatest change in topography used in this work, which is the one with interdigital capacitor finger structures and to tune the controller gains and maximum scan speed on this sample until no ringing can be observed in the sensor signals. This results in maximum scanning speeds of about one line per second with a scan range of 50um over the 200nm high structures. Figure 6.1 shows an example of a topography and error image on this sample.

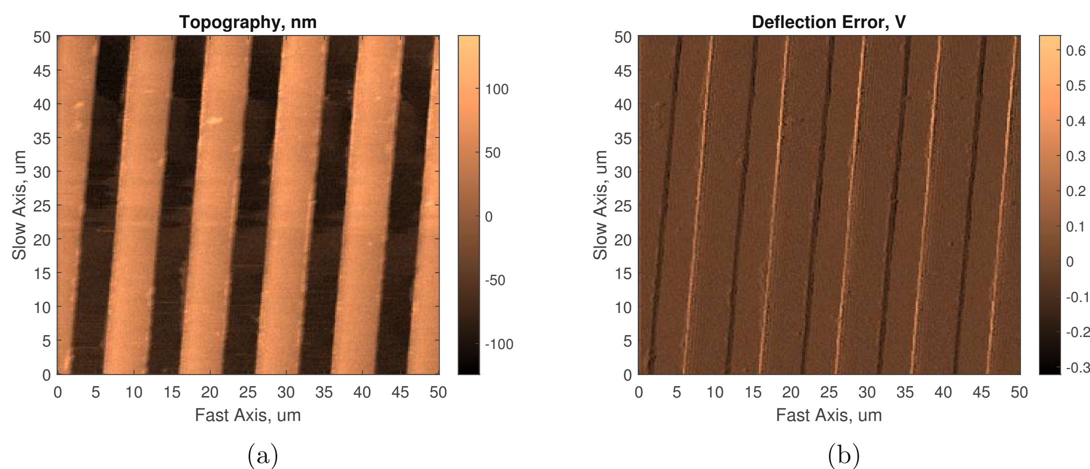

(a) (b)

Figure 6.1: AFM images of interdigital capacitor structure, (a) topography in nm and (b) deflection error in V.

To use the AFM as a reference a sufficiently low scan speed with high gains must be selected. Since the maximum possible speeds are 50um/s the scan speed for reference measurements was chosen to be a decade slower at 5um/s, at the same gains. The results of these measurements are treated as ground truth for evaluating SMM positions. The images presented in this chapter are recorded as rasterized images with 256x256 pixels, although the scan itself is continuous in every line. AFM scans are implemented with a fast axis and a slow axis and usually the axis perpendicular to the cantilever beam is selected as the fast axis. The scan trajectories in this work are continuous lines

Die approbierte gedruckte Originalversion dieser Diplomarbeit ist an der TU Wien Bibliothek verfügbar
The approved original version of this thesis is available in print at TU Wien Bibliothek.
TU WIEN Bibliothek Your knowledge hub

in the fast axis and discrete values in the slow axis. At each rasterized point in a line the relevant signals are sampled and saved. At the lines end, at the lines start or at both the slow axis gets incremented by a step, depending on the user's choice, if the signals are to be sampled in the forward or backward direction, or in an alternating fashion. This can be useful to identify an asymmetrical tip or simply to boost imaging speed at the cost of accuracy (since the tip is not perfectly symmetrical). An internal flag in the real time system is raised to indicate a finished line as soon as the 256 points are done. If only one direction is used to measure then the travel time back to the start is used for data retrieval and display. When the user application has finished reading all data of the line the flag is cleared and a new line may start at an incremented slow axis position. The step size in the slow axis is the scan range divided by 255 to get a quadratic image.

6.2 Scanning Microwave Microscopy, Contact Mode

SMM is evaluated on the dopant calibration sample with the interferometric method described in Chapter 4.5. The tuning of the interferometer is done in contact with the sample surface, but it is left slightly out of tune. If it were tuned exactly, then the Q-factor of the destructive interference get too high, the slopes get too steep and the measurement is more prone to noise. The measurement frequency is selected to be slightly off the destructive interference either of the slopes to gain resilience against noise while still maintaining high sensitivity. For the following measurements the IF bandwidth is 1 kHz, the VNA is in CW mode with an external trigger and a 256 point wide sweep is started at every line.

As mentioned before, a tip sample bias of 0.7 V is applied. This is necessary to be able to distinguish between the different dopant concentrations. [41] has a chapter dedicated to describing this relation. The basic concept is that the difference in work function of the material under test and the platinum tip together with the bias voltage influences how electron charges might be depleted. Different carrier concentrations are only distinguishable with SMM at certain bias voltages.

The measurement of contact mode SMM is done in the same way as the AFM topography scan. At each rasterized point a trigger signal is sent to the VNA and a measurement is taken. Again, the way back to the starting point of the line is used to grab the recorded data and to start a new sweep.

Figure 6.2 shows such a complete set of images consisting of AFM topographical (a) and error (b) images and SMM S_{11} magnitude (c) and phase (d) images on the dopant calibration sample. Good sensitivity and contrast is achieved with the implemented interferometric method.

Die approbierte gedruckte Originalversion dieser Diplomarbeit ist an der TU Wien Bibliothek verfügbar
The approved original version of this thesis is available in print at TU Wien Bibliothek.
TU WIEN Bibliothek Your knowledge hub

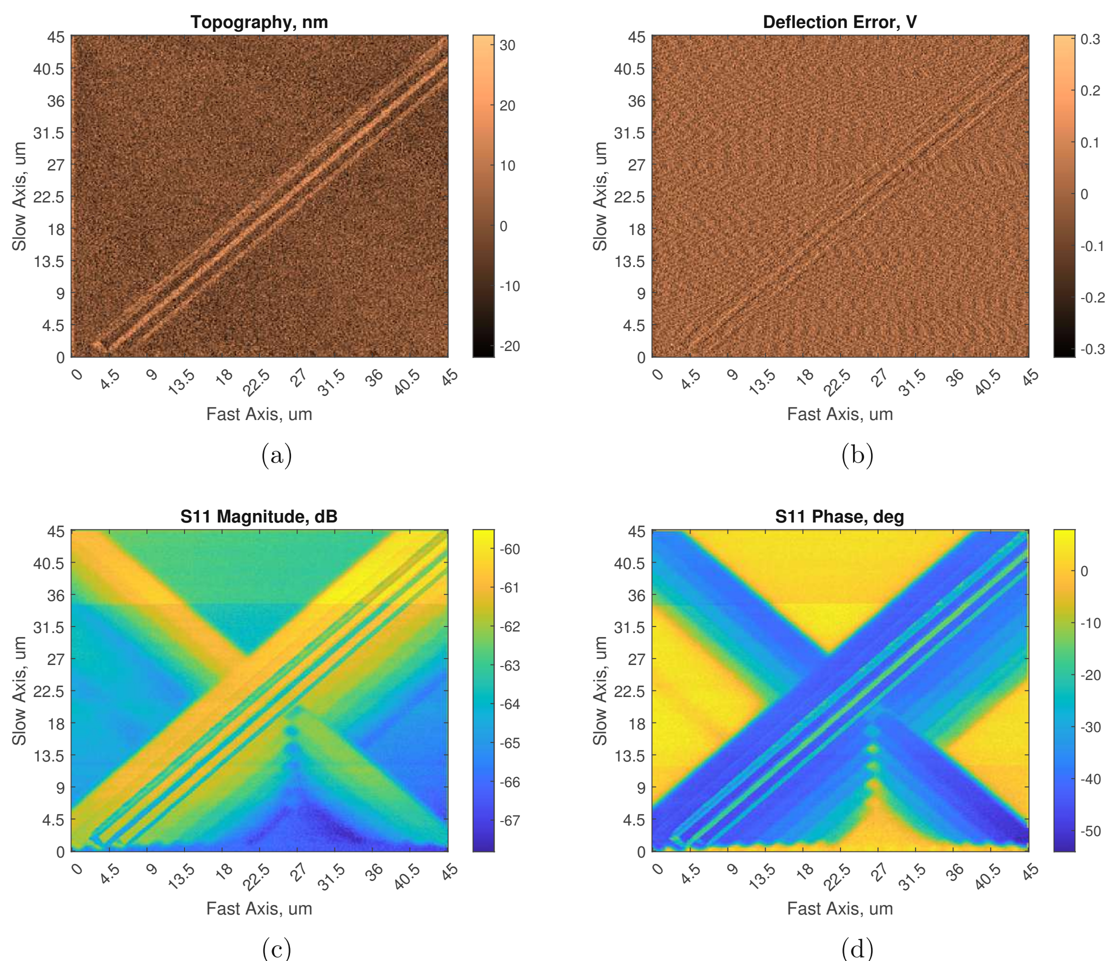

Figure 6.2: AFM and SMM images of dopant calibration sample, (a) topography in nm, (b) deflection error in V, (c) S_{11} magnitude in dB and (d) S_{11} phase in degrees.

Figure 6.3 (a) to (d) show the same measurement method on the inductor sample, that features an indefinite amount of passivation, to prove that the intended subsurface imaging qualities of SMM are also present in this implementation. There is topography present, but no direct contact to the metal spiral is made during the measurement. This is verified by measuring the reflection coefficient at the exposed contact pads in comparison to the inductor structure, which shows a lower reflection coefficient. The buried metal traces can be clearly distinguished from the bulk silicon in the middle but a significant amount of drift is present.

A typical method to eliminate slow changing properties of an image in all SPMs is to subtract a fitted plane from the measurement data. In AFM this is done to eliminate sample tilt, here the same principle is applied to eliminate the influence of the drift. Contrary to sample tilt, which has a constant slope, the measurement drift does not have a static rate of change. Therefore the applied fit is a polynomial plane fit of the 3rd order (a linear fit in every line would also work). Figure (e) and (f) show the same measurement with a this plane fit. A great improvement in contrast is observed.

Die approbierte gedruckte Originalversion dieser Diplomarbeit ist an der TU Wien Bibliothek verfügbar
The approved original version of this thesis is available in print at TU Wien Bibliothek.
TU Bibliothek WIEN Your knowledge hub

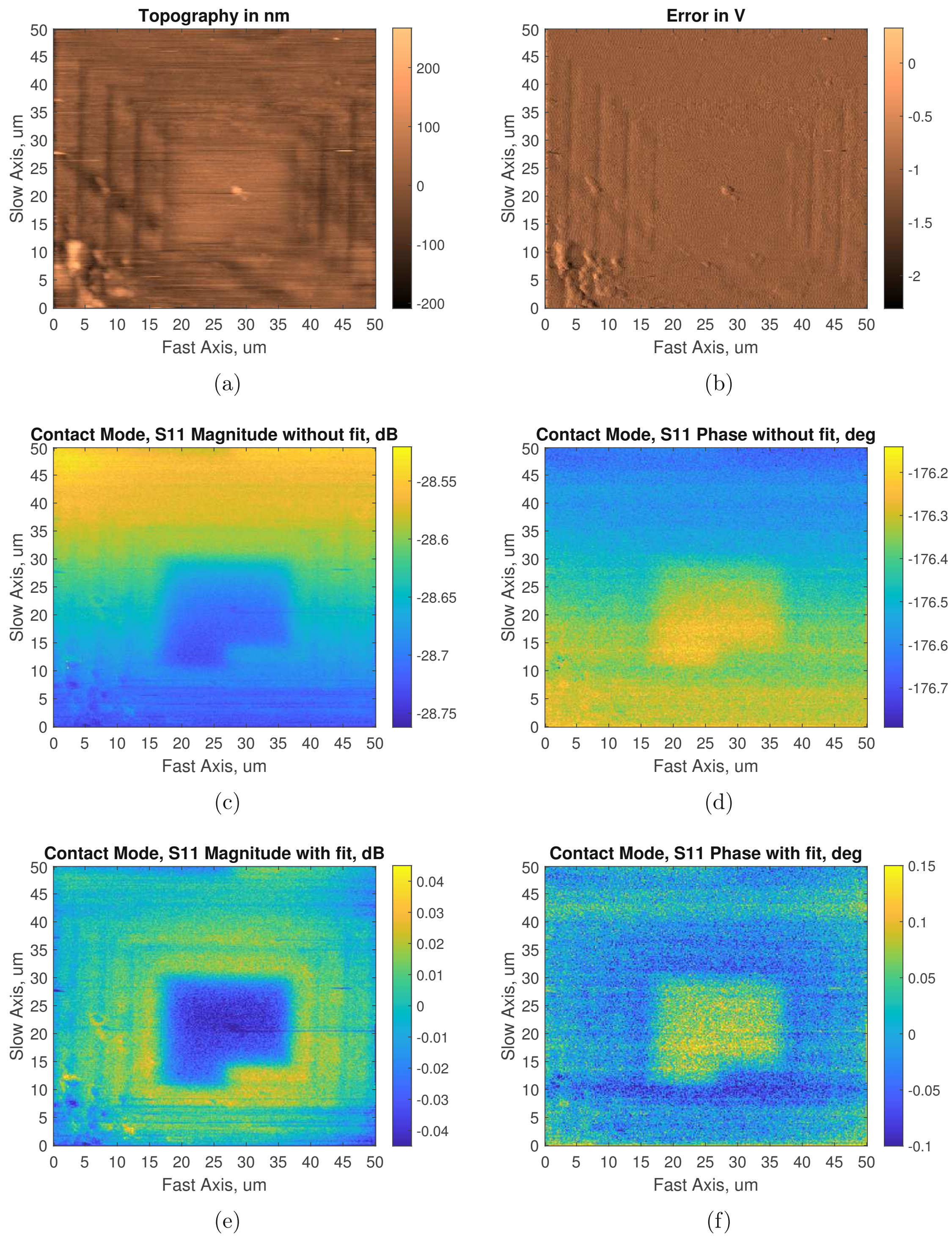

Figure 6.3: AFM and SMM images of spiral structure beneath passivtaion, (a) topography in nm, (b) deflection error in V, (c) S_{11} magnitude in dB, (d) S_{11} phase in degrees, (e) S_{11} magnitude after plane fit and (f) S_{11} phase in degrees after plane fit.

Die approbierte gedruckte Originalversion dieser Diplomarbeit ist an der TU Wien Bibliothek verfügbar
The approved original version of this thesis is available in print at TU Wien Bibliothek.
TU Bibliothek Your knowledge hub WIEN

6.3 Scanning Microwave Microscopy, Lift Mode

A lift mode for SMM is implemented to judge the dependency of the measurement on the tip to sample distance. Lift modes describe measurement modes that scan the same line twice. The first scan line collects topography information by AFM. The second scan line uses this information to follow the topography with a defined tip to sample surface distance. The expected result is the same images as before but with reduced sensitivity due to worse capacitive coupling between the tip and sample. The lift height in the presented measurements is 75 nm.

Figure 6.4 shows the same area from before on the dopant calibration sample in lift mode with and without a plane fit. The lift mode measurement is also tested on the inductor sample, since the sensitivity in the measurements presented above is already reduced by the passivation. A further reduction in sensitivity by lifting the tip could lead to a SNR that is too low to safely distinguish between different materials. These measurements are shown in Figure 6.5. While the involved materials can still be distinguished in the fitted images, the images without fit show too little contrast to identify materials by absolute values.

TU WIEN Bibliothek Your knowledge hub
Die approbierte gedruckte Originalversion dieser Diplomarbeit ist an der TU Wien Bibliothek verfügbar
The approved original version of this thesis is available in print at TU Wien Bibliothek.

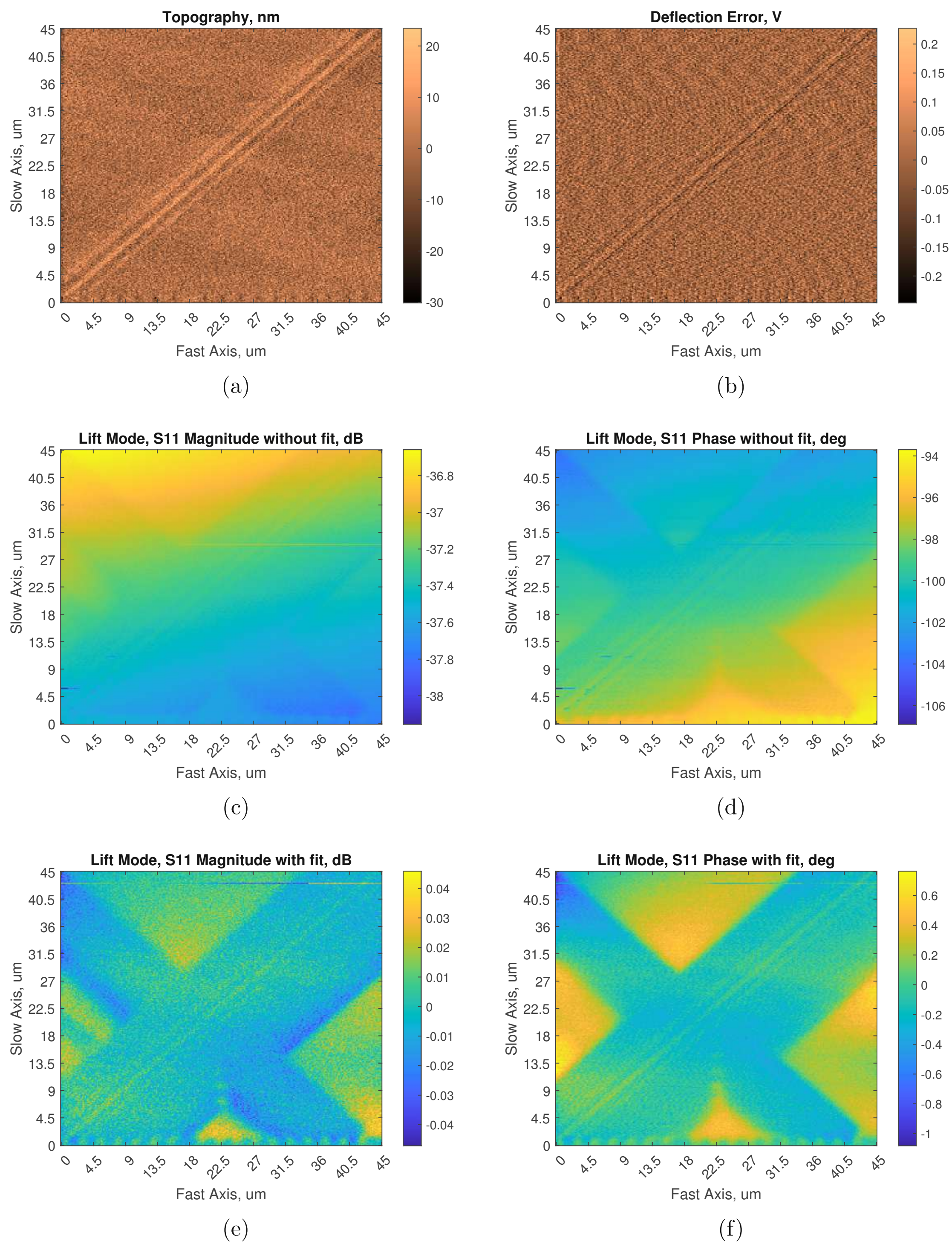

Figure 6.4: AFM and SMM images of dopant calibration sample in lift mode, (a) topography in nm, (b) deflection error in V, (c) S11 magnitude in dB, (d) S11 phase in degrees, (e) S11 magnitude after plane fit and (f) S11 phase in degrees after plane fit.

Die approbierte gedruckte Originalversion dieser Diplomarbeit ist an der TU Wien Bibliothek verfügbar
The approved original version of this thesis is available in print at TU Wien Bibliothek.
TU Bibliothek Your knowledge hub WIEN

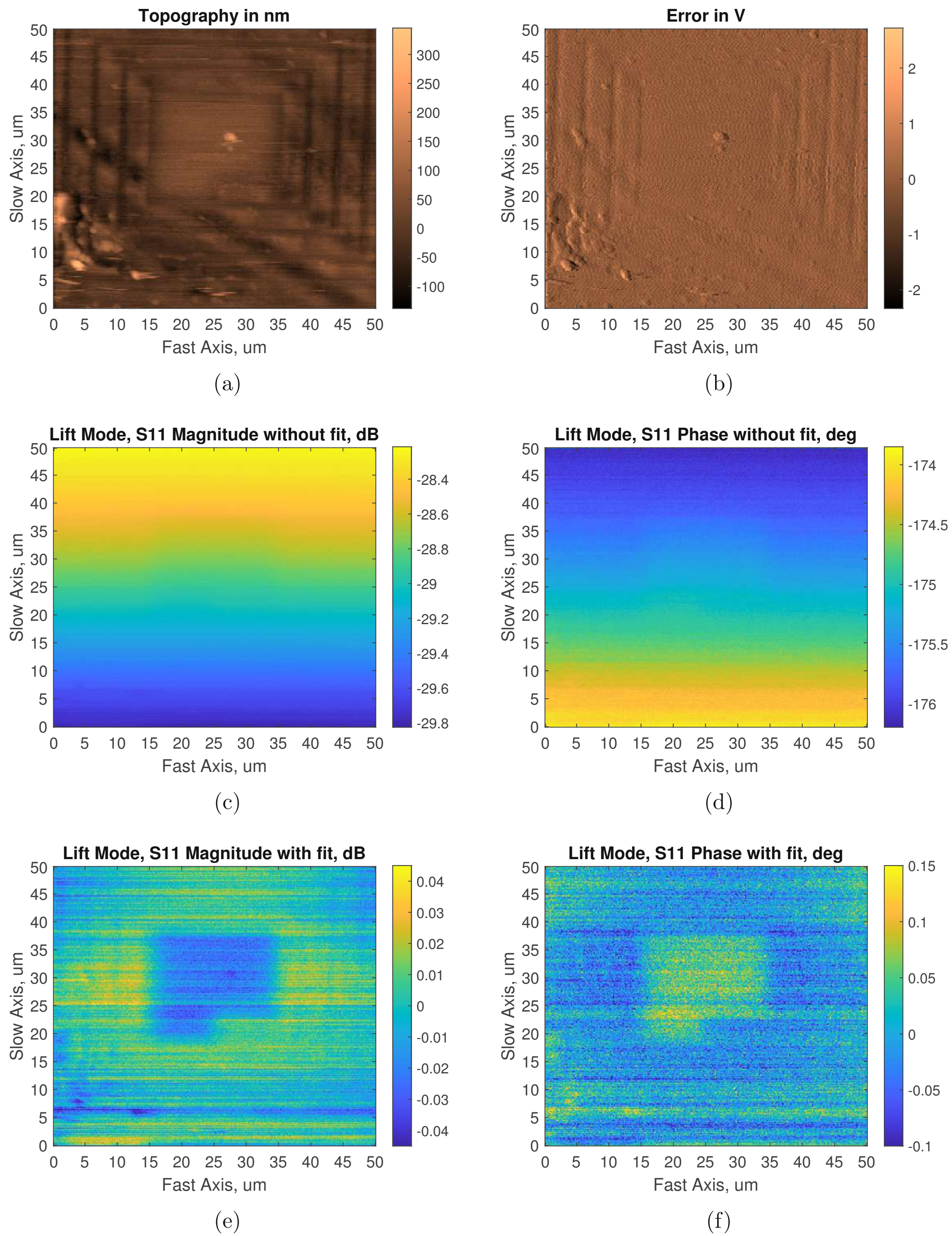

Figure 6.5: AFM and SMM images of spiral structure beneath passivtaion in lift mode, (a) topography in nm, (b) deflection error in V, (c) S11 magnitude in dB, (d) S11 phase in degrees, (e) S11 magnitude after plane fit and (f) S11 phase in degrees after plane fit.

Die approbierte gedruckte Originalversion dieser Diplomarbeit ist an der TU Wien Bibliothek verfügbar
The approved original version of this thesis is available in print at TU Wien Bibliothek.
TU WIEN Bibliothek Your knowledge hub

6.4 Evaluation of the implemented measurements and measurement drift

AFM contact mode works flawlessly within the scopes of this work. The lateral positioning accuracy goal is to be sub-micrometer which can easily be verified with the implemented AFM for non-buried structures. The vertical positioning goal is less than 100 nm and the strain gauge measurement has a noise floor well below that. From a given SMM position the piezo can be simply extended until contact is detected to verify this. SMM in contact mode works well, but the loss in sensitivity when the tip is no longer in contact with the sample in lift mode is concerning, because of the drift in these measurements, which is of greater magnitude than the remaining imaging contrast. This is not a problem when it comes to lateral positioning, since a plane fit can restore much of the supposedly lost information and the deciding criteria is the contrast between different materials. Figure 6.6 shows a cross section of the unfitted SMM lift mode measurements around the centre of the spiral (green horizontal line at 26um) and clear contrast is still achievable between the bulk silicon and the metal spiral even in lift mode. Although the individual spiral turns can no longer be resolved, a target pad of a few micrometer surrounded by bulk material should be detectable.

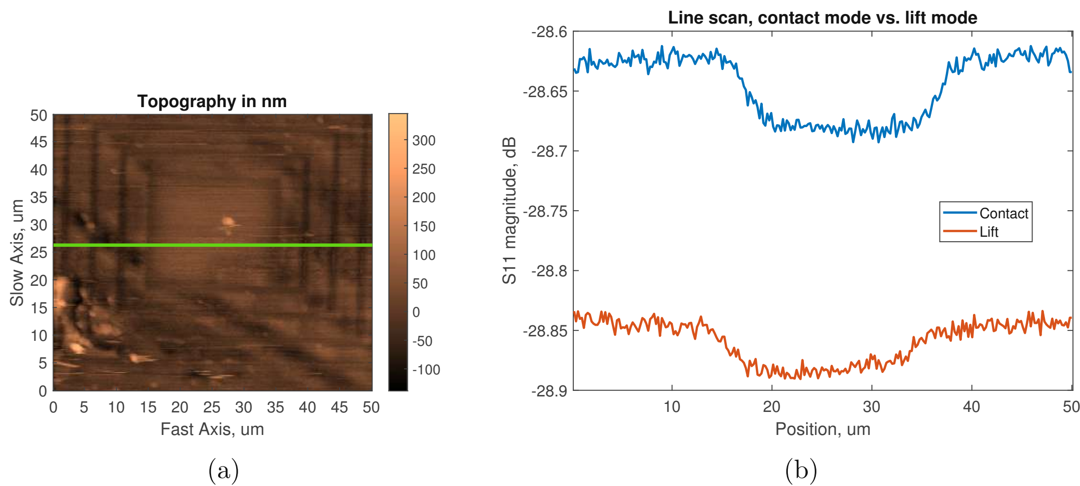

(a) (b)

Figure 6.6: (a) Topography image of the spiral inductor sample. The green line marks the position of a SMM line scan shown in (b), conducted in contact mode (blue) and lift mode (red).

The positioning strategy involves calibrating certain S_{11} values to a tip sample distance over a given material. This is not possible because of the measurement drift. The drift in the presented lift mode images is a magnitude higher than the image contrast. Figure 6.7 shows the drift over a day in the laboratory. For this measurement the tip is lifted high above the sample surface (about 1 mm-2 mm) to ensure that a change in tip sample distance is not the cause for this drift. The measurement setup is also encapsulated with a box to mitigate air fluctuations and to provide a stable temperature. Because of its location the VNA was not under the box and therefore exposed to any environmental changes that may happen in the laboratory.

Die approbierte gedruckte Originalversion dieser Diplomarbeit ist an der TU Wien Bibliothek verfügbar
The approved original version of this thesis is available in print at TU Wien Bibliothek.
TU WIEN Bibliothek Your knowledge hub

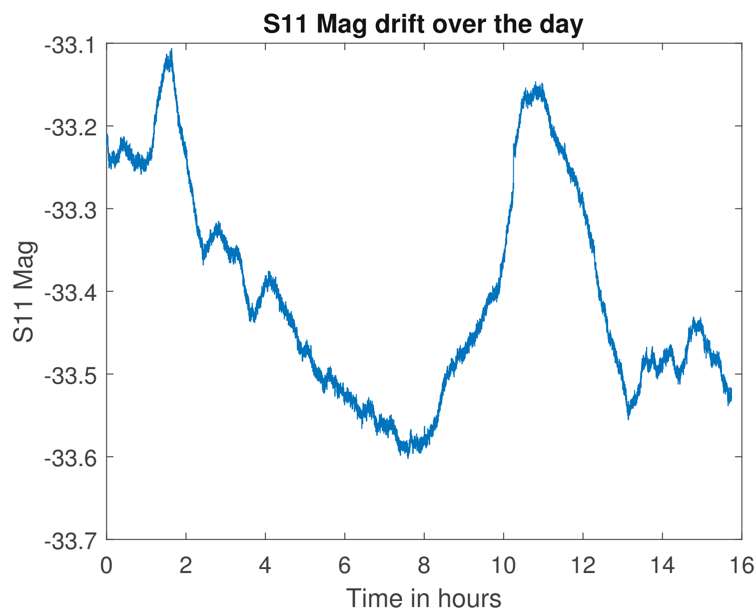

Figure 6.7: Drift of S_{11} measurement over 16 hours while tip is retracted from the sample surface.

A possible explanation for the drift might be changes in the length of the cables and therefore a shift in the tuning of the interferometer. This change could originate from changes in temperature despite the efforts taken to mitigate this, or might be an artefact of the VNA itself when the internal components heat up. It could also be a mechanical shift since the setup has moving cable connections while in use.

A solution on how to deal with this drift is already shown above, by fitting planes. Alternatively every line can be fitted individually. This is possible with the presented lift mode, where a constant tip to sample distance is maintained using information from a prior AFM scan. The final positioning strategy does not have this information (the goal is to be contactless, so no contact-based AFM scans are allowed) and can therefore only rely on the S_{11} measurements for vertical positioning. This does not work with absolute values as shown in Figure 6.8, where the blue and red line are about 10 um, or 4 min in measurement time apart, but are at the same tip to sample distance. The SMM lift mode scans at those lines have the same contrast between materials, but they do not share the same absolute values for said materials. Therefore a different approach has to be found, that is robust regarding the measurement drift, and that can assign an unambiguous quantity for each material to a defined tip to sample distance.

Die approbierte gedruckte Originalversion dieser Diplomarbeit ist an der TU Wien Bibliothek verfügbar
The approved original version of this thesis is available in print at TU Wien Bibliothek.
TU WIEN Bibliothek Your knowledge hub

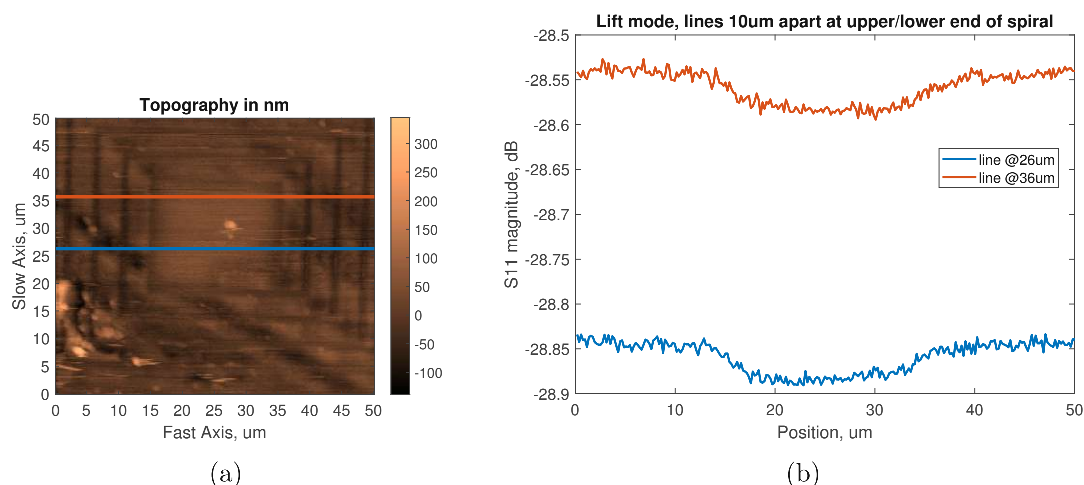

Figure 6.8: (a) Topography image of the spiral inductor sample, marked lines are (b) SMM line scans of spiral sample in lift mode at lower (blue) and upper (red) end of the center of the spiral.

The solution to this problem is inspired by the voltage sensing method presented in [53], where a differential measurement of the transmitted voltage from an excited device area to a passive probe is fitted to a non-linear capacitance model.
A differential measurement eliminates all properties that change slower than the characteristic time constant of the measurement (i.e. time between two data points) and is therefore well suited to combat drift in an otherwise unchanging system. However it also eliminates all common mode signals, which might cause different problems, when those parts are of interest.

The non-linear fit in itself is also of interest, because it describes the capacitance between the sample and the tip over their distance, which is also the defining quantity for reflection coefficient measurements.

The next chapter describes in detail how adapted differential measurements of the reflection coefficient, that are significantly faster than the shown drift, can be used to position vertically. A method based on a calibration that uses a similar non-linear model is used to implement scans, which can map the contrast in materials/topography without coming into contact with the sample surface. These scans can be used to accurately position laterally.

Die approbierte gedruckte Originalversion dieser Diplomarbeit ist an der TU Wien Bibliothek verfügbar
The approved original version of this thesis is available in print at TU Wien Bibliothek.
TU WIEN Bibliothek Your knowledge hub

CHAPTER 7

Non-invasive probe positioning

This chapter presents the final methodology of the non-invasive probe positioning strategy based on the investigations and evaluations shown until here. First differential measurements of the reflection coefficient are discussed to combat measurement drift. Then the final calibration and measurement procedure to determine tip to sample distance without touching the surface is presented and the accuracy of this measurement is verified with AFM. The procedure is employed on passivated and non-passivated structures to map changes in topography and material composition. A brief discussion on a detected unexpected property of the investigated sample structures is given to show a potential use case outside of pure positioning as an end to the chapter.

7.1 Differential measurements

The measurement drift of the reflection coefficient is greater than the contrast in the measurements, when the tip is lifted off the sample surface and thus the deciding factor why absolute measurements can not be considered suitable for this work. This section discusses how differential measurements can provide a more stable solution.

There are two major ways to combat slow changing properties in a measurement system. The first option is to simply find ways to increase the measurement speed in relation to the drift time-constants. This is a good tactic for self-contained small scale measurements that do not have to be quantitatively comparable with other measurements over time, which is not compatible to the stated goals. The second common approach are differential measurements. These are usually not the first choice, because they eliminate any common mode signal and every slow change and therefore have the inherent risk of eliminating wanted measurement quantities. But they are desirable when a measurement has to be time independent, since they are usually carried out in quick succession. The time scale on which the system changes is in the range of minutes. Therefore the differential measurement has to happen on a time

TU Bibliothek Your knowledge hub WIEN
Die approbierte gedruckte Originalversion dieser Diplomarbeit ist an der TU Wien Bibliothek verfügbar
The approved original version of this thesis is available in print at TU Wien Bibliothek.

scale at least a decade smaller than that, to ensure that drift does not cause problems again. This means the differential measurement has likely to be done in less than a second. As stated before, the maximum scan speed is about $50\,\mu$m per second and reasonable speeds with better resolution are much slower than that. Therefore the differential measurement can neither happen for the whole scan area nor for a line, but has to be to carried out for each measurement point separately before moving on to the next.

There are two major implications emerging from this. First, the scan trajectory and measurement cannot be viewed as decoupled as they were before. The investigated area has to be discretized into individual points at which the tip needs to stop and carry out the differential measurement, before moving on to the next point, or scanned with a continuous scan that is slow enough, that the whole differential measurement can be executed while the scan trajectory has not moved the tip further than the intended resolution. For sub-micrometer resolution this means either very slow scan speeds or very fast differential measurements, or possibly both. Secondly, the only degree of freedom that is left for this differential measurement is the tip to sample distance. All other quantities that could affect the measurement, like time and lateral position and therefore material composition, are fixed (or exhibit sufficiently small change). Another possible method for a differential measurement would be to change settings on the VNA, like the measurement frequency, but this would mean changing the interferometer if it is in use, or having a time-stable calibration that perfectly eliminates all waveguide elements between the VNA port and the tip, which are both not preferable if the simpler change in tip to sample distance works out.

To investigate if a differential measurement in the vertical axis can fulfill the requirements to achieve the intended goals, the relation between reflection coefficient and tip to sample distance is examined for different materials. This is done with an adapted force curve measurement, where the probe is slowly lowered towards the sample surface until contact is detected. On this surface approach the reflection coefficient, strain gauge signal and cantilever deflection signal are recorded. All reflection coefficient related measurements in this chapter are conducted without the interferometric setup (except where stated otherwise), since it has not proven to be stable over longer periods of time (hours) and sensitivity would shift with each material under test and would therefore require a lot more calibration effort.

The approach curves are recorded on the passivated sample with the four differently sized metal pads. Figure 7.1 shows these curves for the pads, the deeper buried trace and the bulk silicon around them. They show almost the same linear relation up until about the last micrometer of tip to sample distance and then descend at different non-linear rates. This is a promising result because it confirms that different materials exhibit different reflection coefficients with different rates of change even for passivated structures, so the change is not caused purely by surface interactions. A differential measurement of course depends on these rates of change as the primary measurement quantity.

Die approbierte gedruckte Originalversion dieser Diplomarbeit ist an der TU Wien Bibliothek verfügbar
The approved original version of this thesis is available in print at TU Wien Bibliothek.
TU WIEN Bibliothek Your knowledge hub

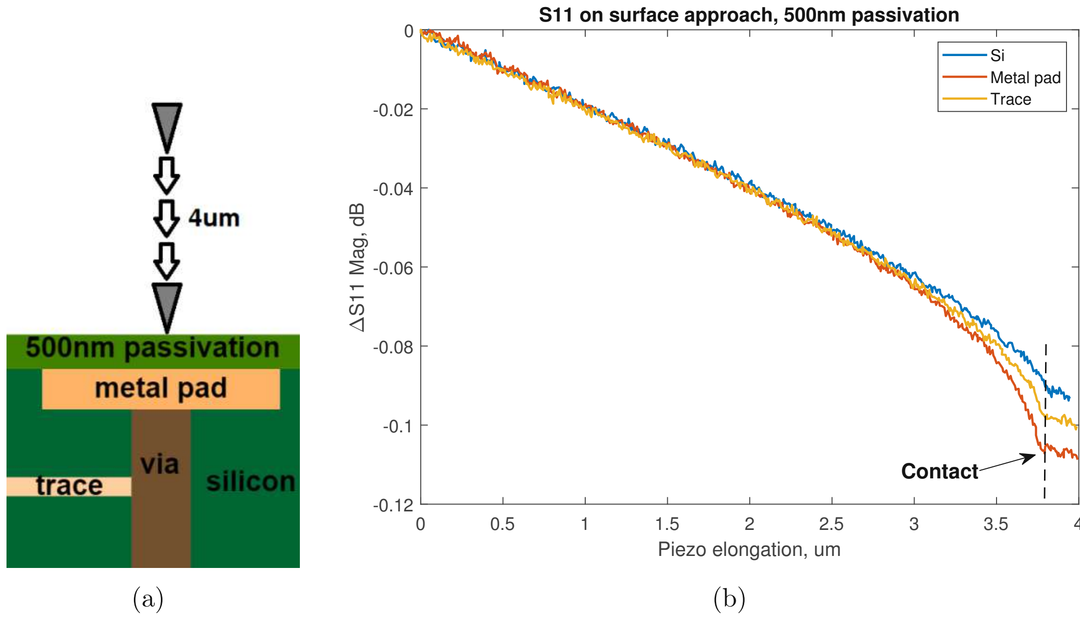

(a) (b)

Figure 7.1: (a) Sample structure and tip approach, (b) ΔS_{11} magnitude during the sample surface approach for burried metal pad (red), burried trace (yellow) and bulk silicon (blue) on a passivated sample. ΔS_{11} means, that the starting value was subtracted from the curves, so that they start at 0 dB $\Delta\left|S_{11}(z)\right|_{dB} = \left|S_{11}(z)\right|_{dB} - \left|S_{11}(0)\right|_{dB}$.

To prove that these kinds of measurements do not exhibit the same drifting behaviour the measurement is repeated in the form of a discrete area scan where at each point the whole approach curve is recorded. The curves are then fitted with the model presented in [53] with minor adaptions. C_c is a constant and R_{eff} is an effective tip size:

$$S_{11}(z) \propto C_{1,n}(z) \cdot S_{11,n} + z \cdot S_{11,l} + S_{11}(0) \tag{7.1}$$

$$C_{1,n}(z) = C_c \cdot ln\left(1 + \frac{R_{eff}}{z + \frac{d}{\epsilon_r}}\right) \tag{7.2}$$

This leads to maps of the measured reflection coefficient from which the complex non-linear $S_{11,n}$ and linear $S_{11,l}$ weighting factors of the curves are extracted. The magnitude $|S_{11,n}|$ is the measurement quantity shown in the following figures. Recording of these maps can be very time consuming. A complete approach and retraction of the cantilever tip takes about half a second so the sample rate is two samples per second. To compare it to the measurements from before that were on the scale of 10 min-60 min depending on scan speed, a 50x50 μm image with 256x256 pixels at one pixel per second takes about nine hours to record with this method. Therefore the following images have at maximum 75x75 pixels, which is about one and a half hours of recording. Figure 7.2 shows an area map of all four metal pads.

Die approbierte gedruckte Originalversion dieser Diplomarbeit ist an der TU Wien Bibliothek verfügbar
The approved original version of this thesis is available in print at TU Wien Bibliothek.
TU WIEN Bibliothek Your knowledge hub

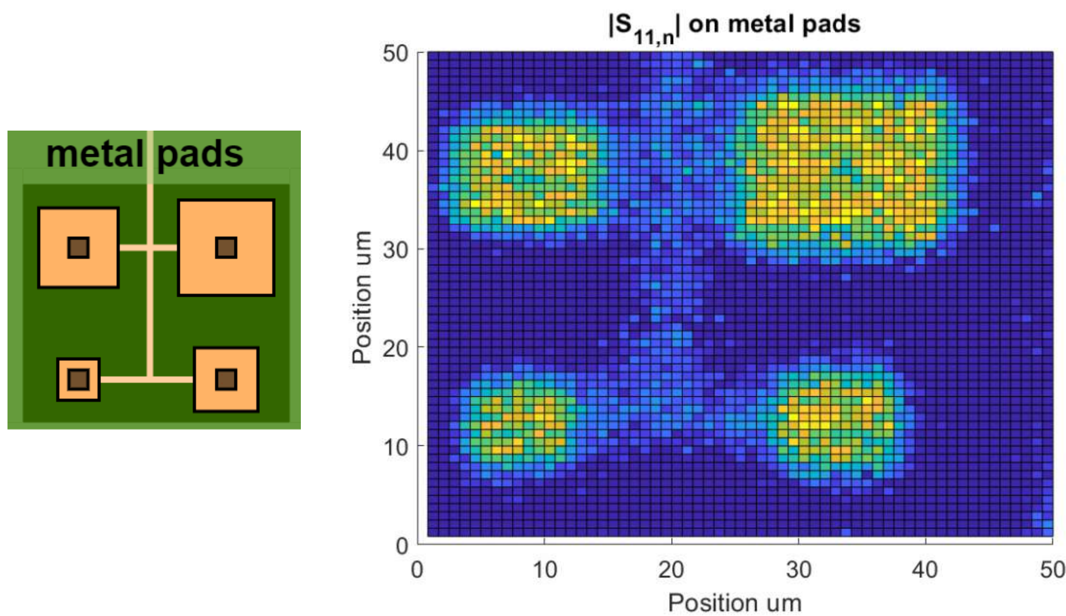

Figure 7.2: Map of non-linear weighting factor in the measured reflected coefficient on a passivated sample, where yellow, light blue and deep blue denote metal pads, trace and bulk silicon respectively.

All pads are clearly visible and good contrast to the surrounding silicon is achieved. Even the small traces that are deeper buried than the pads are visible. Figure 7.3(a) shows the 6.5um square pad on the bottom left of the structure at higher resolution. The artefacts at the bottom are due to implementation issues. Figure 7.3(b) shows a map of the metal pad on the bottom left. It is recorded with the interferometric method at 12 GHz where a destructive interference was tuned close to the maximum rated frequency of the power splitter. This shows that the omission of the interferometric setup does not result in worse measurements

Note that the colour-maps in all images are set to display the best contrast in their respective image and do not represent the same absolute measurement values. The better contrast of the image without the interferometric setup might be due to the increased measurement frequency and therefore lower impedance, which leads to greater changes in the reflection coefficient. The interferometric setup was useful for the contact mode SMM scans but is not suited for differential measurements, since the enhanced sensitivity is lost due to worse SNR (the measurement is usually 40 dB to 60 dB closer to the noise floor of the VNA on the slope of the interference).

Die approbierte gedruckte Originalversion dieser Diplomarbeit ist an der TU Wien Bibliothek verfügbar
The approved original version of this thesis is available in print at TU Wien Bibliothek.
TU WIEN Bibliothek Your knowledge hub

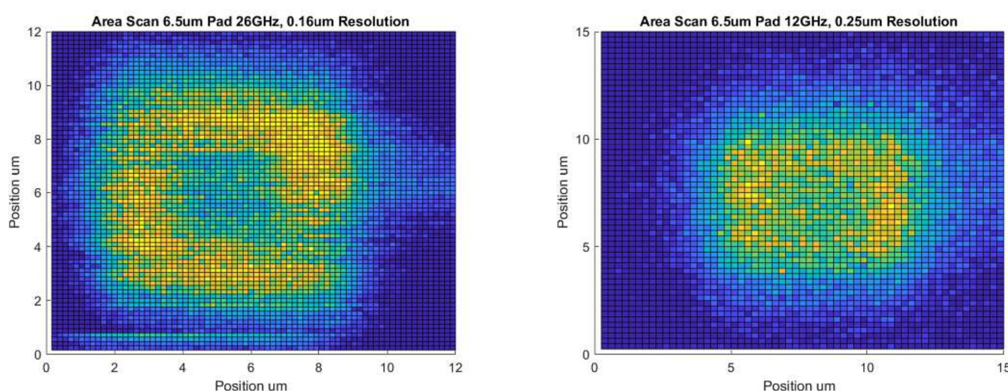

Figure 7.3: Map of non-linear weighting factor in the measured reflected coefficient on 6.5 μm square metal pad (a) at 26 GHz without and (b) at 12 GHz with interferometric method.

The influence of thicker passivation on the achievable resolution is investigated on different areas of the passivated passivated interdigital capacitor structure. Figure 7.4 indicates the measurement areas. Figure 7.5 (area A) shows the influence of a change to thicker passivation during the scan. Note that the upper electrodes (with 1 μm more passivation) can still be resolved, but the colour mapping was chosen to better distinguish the bottom fingers. This also shows the upper limit for structure size in relation to passivation. The fingers are spaced 3.2 μm apart, are 2 μm wide and the passivation in the upper area is 1.5 μm thick. Figure 7.6 (area B) shows a scan with reduced finger separation, from 3.2 μm to 1.6 μm with 1.5 μm passivation. Figure 7.7 (area C) shows the same 1.6 μm separated fingers with only 500 nm thick passivation. The Figures also feature cross-sections in (b) of the lines marked in (a).

The 3.2 μm separated fingers can be resolved as separate structures with both passivation thicknesses in all images. The 1.6 μm separated fingers can be resolved with 0.5 μm passivation, but not with 1.5 μm passivation. A general rule can be established, that the structure size should be at least double the thickness of the covering passivation for good contrast.

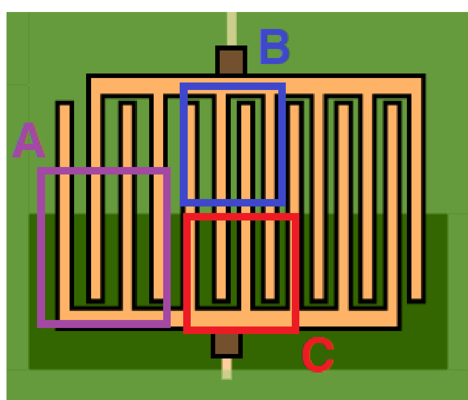

Figure 7.4: Measurement areas A, B and C on interdigital capacitor.

Die approbierte gedruckte Originalversion dieser Diplomarbeit ist an der TU Wien Bibliothek verfügbar
The approved original version of this thesis is available in print at TU Wien Bibliothek.
TU WIEN Bibliothek Your knowledge hub

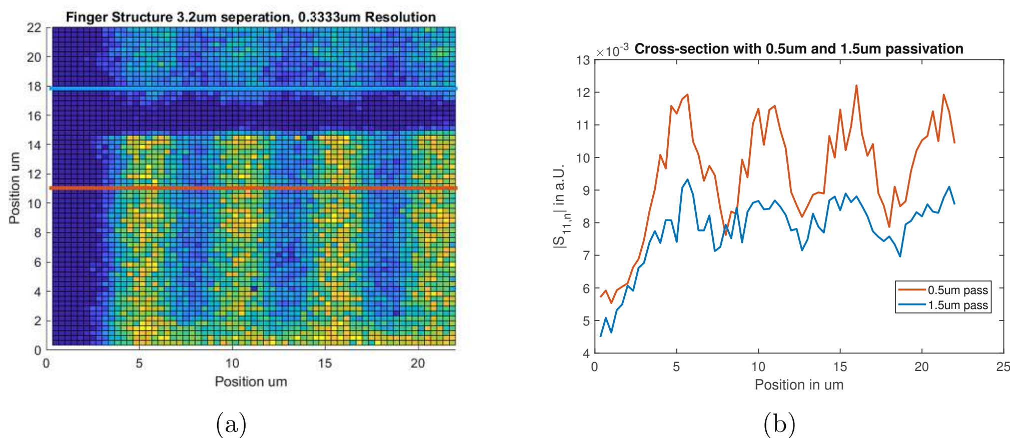

(a) (b)

Figure 7.5: Map of $|S_{11,n}|$ in area A: structures beneath 0.5 μm (bottom fingers, red cross-section) and 1.5 μm of passivation (upper fingers, blue cross-section).

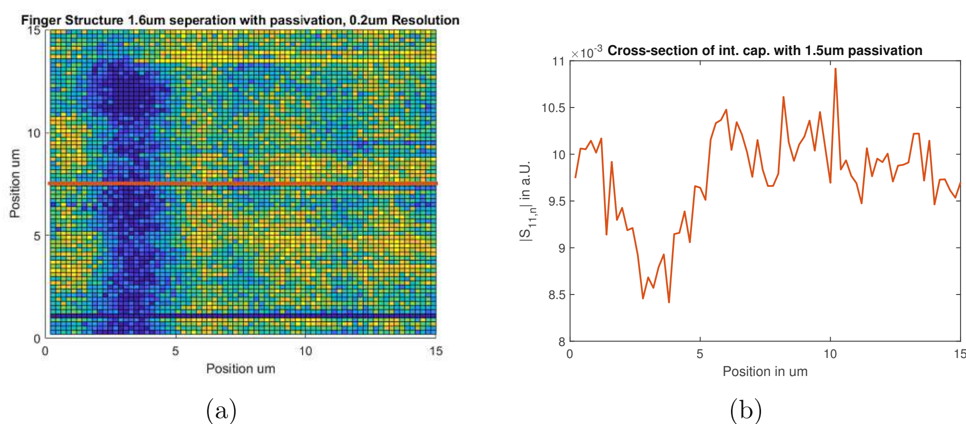

(a) (b)

Figure 7.6: Map of $|S_{11,n}|$ in area B: metal finger structure with 1.6 μm separation and 1.5 μm passivation.

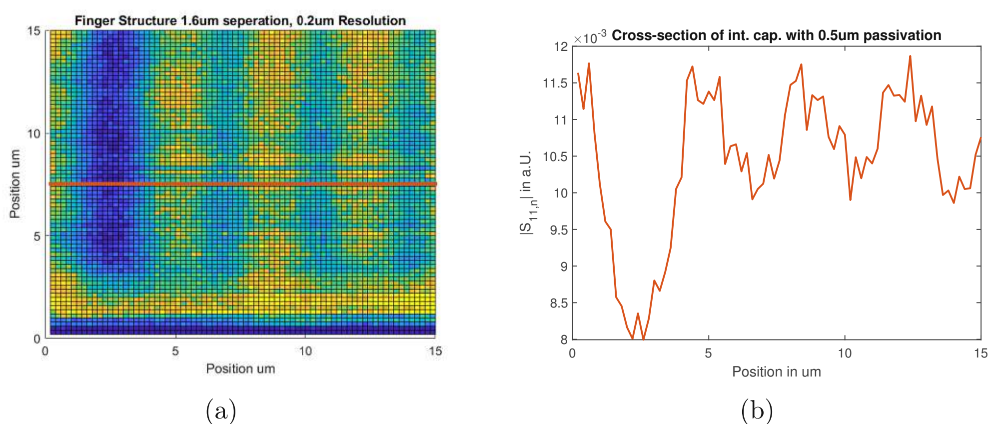

(a) (b)

Figure 7.7: Map of $|S_{11,n}|$ in area C: metal finger structure with 1.6 μm separation and 0.5 μm passivation.

Die approbierte gedruckte Originalversion dieser Diplomarbeit ist an der TU Wien Bibliothek verfügbar
The approved original version of this thesis is available in print at TU Wien Bibliothek.
TU WIEN Bibliothek Your knowledge hub

These results show that lateral positioning can be achieved using differential measurements while eliminating the drift that made the SMM scans unsuitable. From the approach curves a clear material and tip-sample-distance relation can be seen, which can be used for calibration. The only challenge left is to find a method to transform these contact based approach curves to a completely contactless measurement that, except for calibration, never has to touch the sample surface.

7.2 Contactless Differential Measurements

The approach curves shown above are able to map all the relevant information for this work, but they require the detection of surface contact via AFM to be able to reliably gather this information, which inherently needs the tip to be temporarily in contact with the surface. The question becomes now if the same curve, or a similar one that has the same information content, can be recorded without touching the surface, or when to stop the approach. This can be done by taking the idea of the differential measurement a step further to measuring the gradient of the approach curves. Figure 7.8 shows the basic idea.

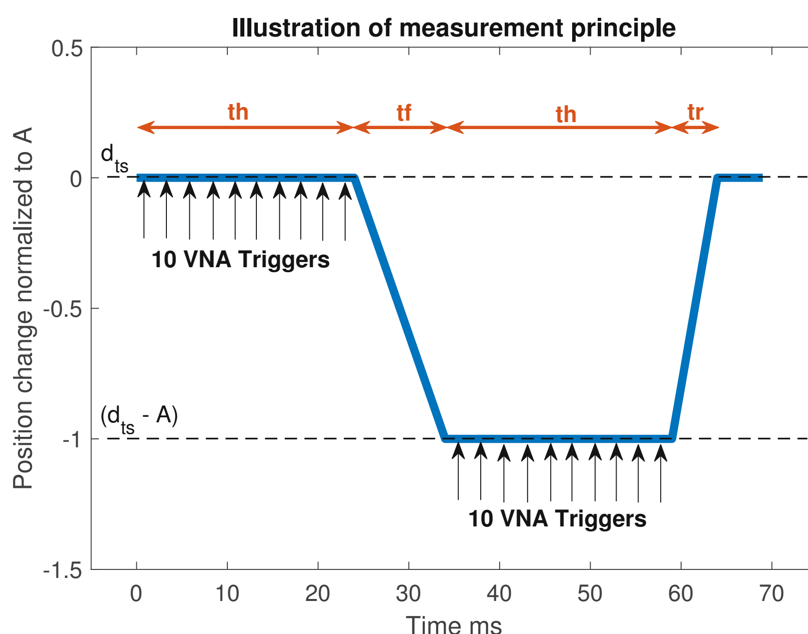

Figure 7.8: Measurement principle: Tip follows trapezoidal trajectory, 10 VNA Points are triggered at each plateau and the difference is calculated.

The tip oscillates with a trapezoidal trajectory with an amplitude A, a rise time tr, a fall time tf and a hold time th. At each of the plateaus ten VNA point measurements are triggered as fast as the chosen IF bandwidth allows (at tip to sample distances d_{ts} and $(d_{ts} - A)$). During the rise time the twenty recorded VNA points are copied to memory and then retrieved during the next measurement cycle to be further processed. The two ten point groups of the corresponding plateaus are averaged for noise suppression and the difference of these two averaged measurements $\Delta |S_{11}(d_{ts})| = |S_{11}(d_{ts})| - |S_{11}(d_{ts} - A)|$

Die approbierte gedruckte Originalversion dieser Diplomarbeit ist an der TU Wien Bibliothek verfügbar
The approved original version of this thesis is available in print at TU Wien Bibliothek.
TU WIEN Bibliothek Your knowledge hub

is calculated. This is the new measurement quantity on which all following results are based. Dividing by A results in the difference quotient of the magnitude of the averaged reflection coefficient measurements at d_{ts} and $d_{ts} - A$, which is abbreviated for readability to:

$$\Gamma_{\Delta,A}\left(d_{ts}\right) = \frac{\Delta\left|S_{11}(d_{ts})\right|}{A} = \frac{\left|S_{11}(d_{ts})\right| - \left|S_{11}(d_{ts} - A)\right|}{A} \tag{7.3}$$

Superimposed on this trapezoidal signal is a control signal that drives the controller target for the strain gauge signal, which gets updated after every measurement period. This control signal sets a certain tip to sample distance offset d_{ts} from which the differential measurement starts. By assigning a certain target value for the controller the tip can be oscillated at a constant height above the sample. Each material composition has a different height d_{ts} for the same difference quotient $\Gamma_{\Delta,A}\left(d_{ts}\right)$ target value. This is later used to map material and topography.

The following measurements, if not stated otherwise, are recorded with $A = 200\,\text{nm}$, $tf = 25\,\text{ms}$, $th = 25\,\text{ms}$, $tr = 12.5\,\text{ms}$ as the standard configuration in this chapter. Figure 7.9 shows the recorded difference quotient measurements for the approach towards the sample surface, that correspond to the gold electrode and the bulk silicon of the non-passivated interdigital capacitor sample.

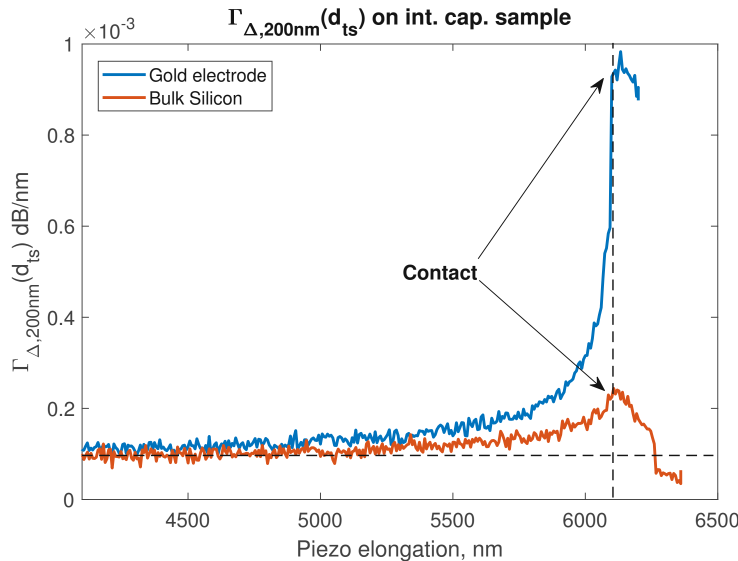

Figure 7.9: Difference quotient $\Gamma_{\Delta,200nm}\left(d_{ts}\right)$ approach curves for gold electrode and bulk silicon.

The measurement principle converts the linear approach from before to a flat, constant curve that is the same for both materials up until about a micrometre before contact, where the non-linear behaviour becomes the driving factor and the difference quotient increases with different rates for the two materials. When the tip comes into contact with the surface during this measurement the effective measurement amplitude decreases, therefore the difference between the two measurements decreases and the difference quotient falls off. This is an interesting result, since each tip to sample

Die approbierte gedruckte Originalversion dieser Diplomarbeit ist an der TU Wien Bibliothek verfügbar
The approved original version of this thesis is available in print at TU Wien Bibliothek.
TU WIEN Bibliothek Your knowledge hub

distance has a distinct difference quotient value assigned for every material composition. Additionally contact can be easily detected without having to rely on the laser setup of the AFM. Figure 7.10 shows the same measurement for the metal pad and bulk silicon of the passivated sample to demonstrate that this method also works on passivated structures.

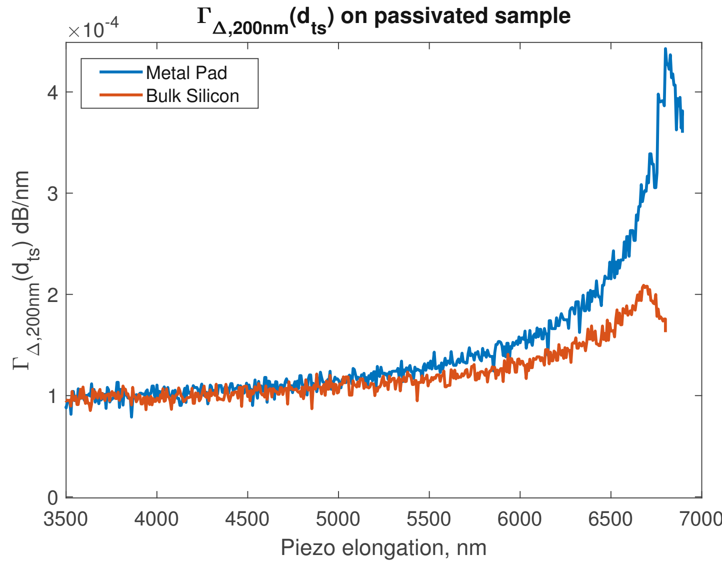

Figure 7.10: $\Gamma_{\Delta,200nm}\left(d_{ts}\right)$ approach curves for metal pad and bulk silicon under 500 nm passivation.

7.3 Vertical calibration and positioning

In this chapter the calibration and position verification is presented on the interdigital capacitor sample, for gold and bulk silicon as the best and worst possible sample structures (non-passivated conductor and pure bulk material).

To be able to tell the vertical position of the probe a calibration needs to be done. The calibration procedure is the same measurement that is described above. To effectively do this, all expected material compositions need to be accessible somewhere on the sample, with a large enough area that capacitive coupling to different materials can be neglected. One such curve is recorded for every required oscillation amplitude and then a non-linear least squares fit is applied:

$$\Gamma_{\Delta,A}\left(d_{ts}\right) = a * \left(\frac{1}{(b + d_{ts})} + \frac{c}{(d + d_{ts})}\right) \tag{7.4}$$

Because the capacitance is expected to be logarithmic (see [53]), the derivative is expected to be one over the distance. The model incorporates two contributors, the tip and the "rest" of the cantilever (i.e. cone, beam). A is the oscillation amplitude; a, b, c and d are fitting parameters that represent geometry and the involved dielectrics and d_{ts} is the tip to sample distance of the upper point of the difference measurement.

Die approbierte gedruckte Originalversion dieser Diplomarbeit ist an der TU Wien Bibliothek verfügbar
The approved original version of this thesis is available in print at TU Wien Bibliothek.
TU WIEN Bibliothek Your knowledge hub

Figure 7.11(a) and (b) show the differential measurements $\Delta\,|S_{11}(d_{ts})|$ over different amplitudes for both materials. As expected greater amplitudes show a greater overall difference along the curve and have a more pronounced non-linear part than those curves with a smaller amplitude, whose non-linear part becomes dominant closer to the sample surface. Note that in all following figures the X axis ("Start point distance to surface") is the starting position of the measurement (as illustrated in Figure 7.8). S_{11} is recorded at the two tip to sample distances d_{ts} and $(d_{ts} - A)$, therefore the shown X axis position where contact is detected and the curve starts is the amplitude value.

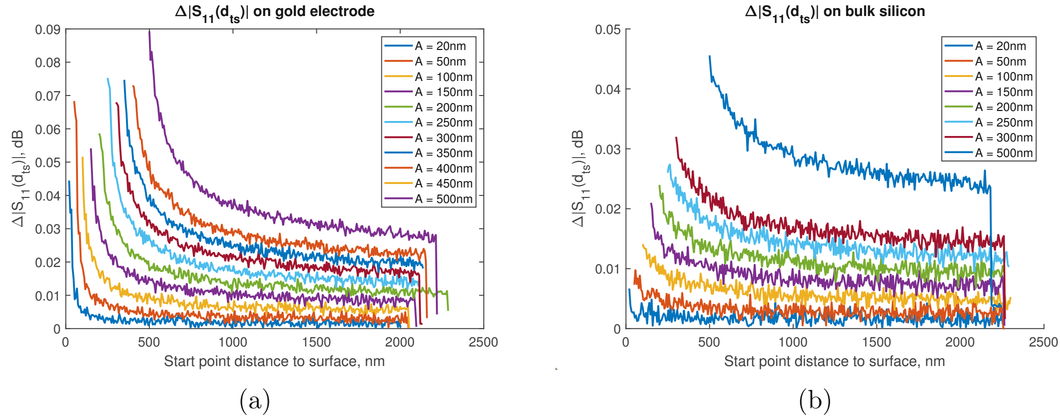

Figure 7.11: Differential measurement $\Delta\,|S_{11}(d_{ts})|$ over tip to sample distance d_{ts} on (a) gold electrode and (b) bulk silicon for different amplitudes A.

Smaller amplitudes feature a worse signal to noise ratio since the measurement noise is independent of the amplitude. Figure 7.12(a) and 7.13(a) show these same measurements, but in relation to their respective amplitude: $\Gamma_{\Delta,A}\,(d_{ts})$. Figure 7.12(b) and 7.13(b) show a zoomed section to illustrate the non-linear part more clearly. This is only a variable scaling by the used amplitude A, but it illustrates how smaller amplitudes generate a higher difference per nanometre, since the measurement can happen closer to the surface where the non-linear part is more pronounced.

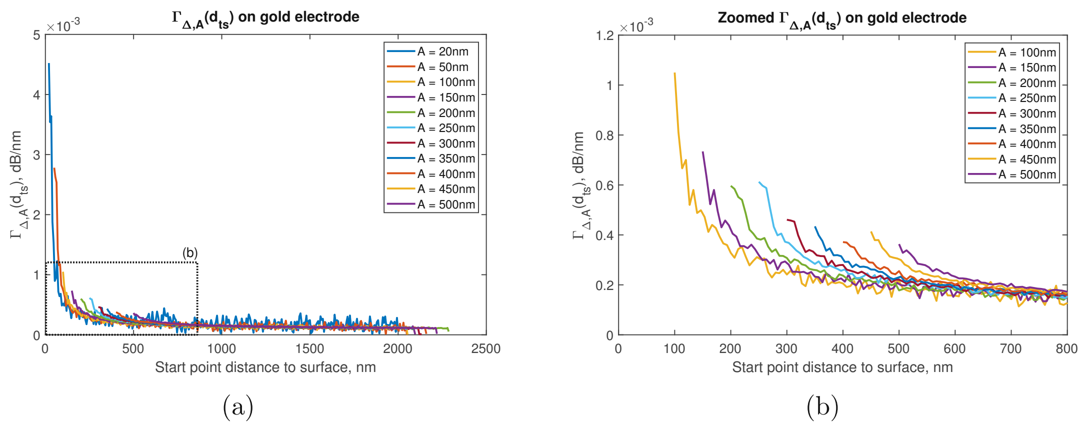

Figure 7.12: (a) Difference quotient $\Gamma_{\Delta,A}\,(d_{ts})$ over tip to sample distance d_{ts} on gold electrode for different amplitudes A and a zoomed section in (b).

Die approbierte gedruckte Originalversion dieser Diplomarbeit ist an der TU Wien Bibliothek verfügbar
The approved original version of this thesis is available in print at TU Wien Bibliothek.
TU WIEN Bibliothek Your knowledge hub

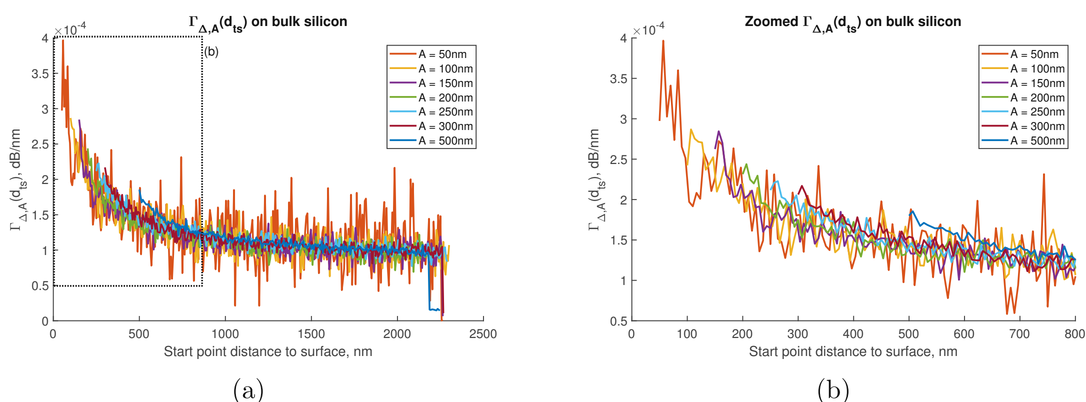

Figure 7.13: (a) Difference quotient $\Gamma_{\Delta,A}(d_{ts})$ over starting point distance of the difference measurement d_{ts} on bulk silicon for different amplitudes A and a zoomed section in (b).

It might seem that choosing a smaller amplitude is always the worse choice when studying Figure 7.11, but consider that the later presented horizontal positioning depends on an unambiguous separation of the involved materials. Larger amplitudes draw out the non-linear part and are therefore closer together when a certain target value for the scanning operation is chosen. Also, it is impossible to be in the non-linear region for both silicon and gold when the amplitude is chosen too large. Figure 7.14 shows a material comparison for $A = 200\,\text{nm}$ and $A = 500\,\text{nm}$. At $A = 200\,\text{nm}$ a certain differential quotient value can be chosen (i.e. 1.8e-4 dB/nm) that still is in the non-linear part of the blue and red curve, while the same is not possible for an amplitude of $A = 500\,\text{nm}$ (yellow and purple curves).

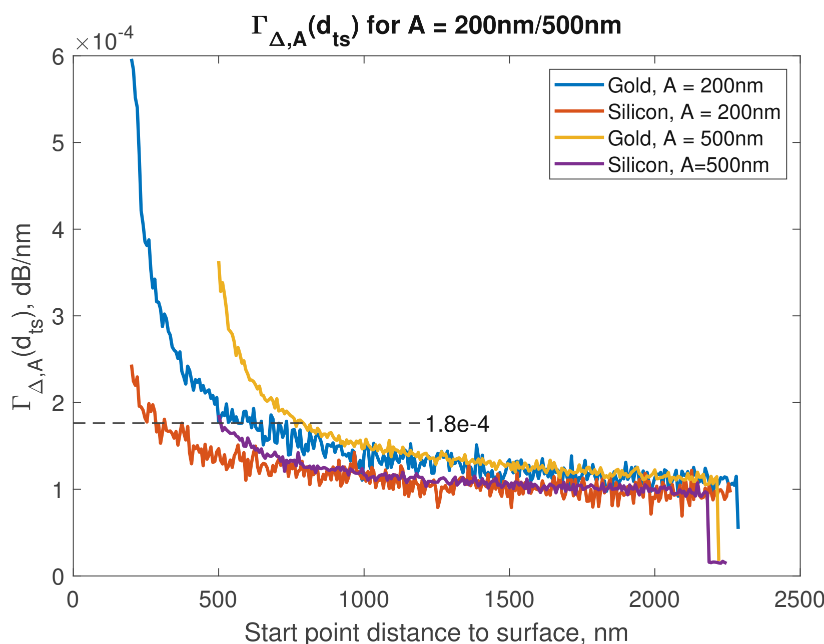

Figure 7.14: Difference quotient for $A = 200\,\text{nm}$ (blue and red) and $A = 500\,\text{nm}$ (yellow and purple) for gold and bulk silicon.

Die approbierte gedruckte Originalversion dieser Diplomarbeit ist an der TU Wien Bibliothek verfügbar
The approved original version of this thesis is available in print at TU Wien Bibliothek.
TU Bibliothek Your knowledge hub WIEN

As mentioned before those curves are approximated with a non-linear least squares fit. Figure 7.15 shows the fitted curves for gold and silicon. The presumed fitting method works well and a certain vertical position can now be dictated to the controller. Although the lowest shown position is at the oscillation amplitude value, this does not mean that this is also the lowest commandable position when oscillatong at a certain amplitude. Any position along the curve can be used as reference for a lower position by simply extending the piezo by the difference after the positioning is complete, i.e. it is possible to position the tip at 200 nm above the surface with an amplitude of A = 500 nm. Also the system can be adapted to use the lower position of the differential measurement as the offset d_{ts} to be controlled (the second measurement psotion would then be $(d_{ts} + A)$ instead of $(d_{ts} - A)$). In the current implemtation the oscillation is generated with the same functional block as the force curves, which always start at the upper position, that is why the upper position is chosen as d_{ts} in the presented results.

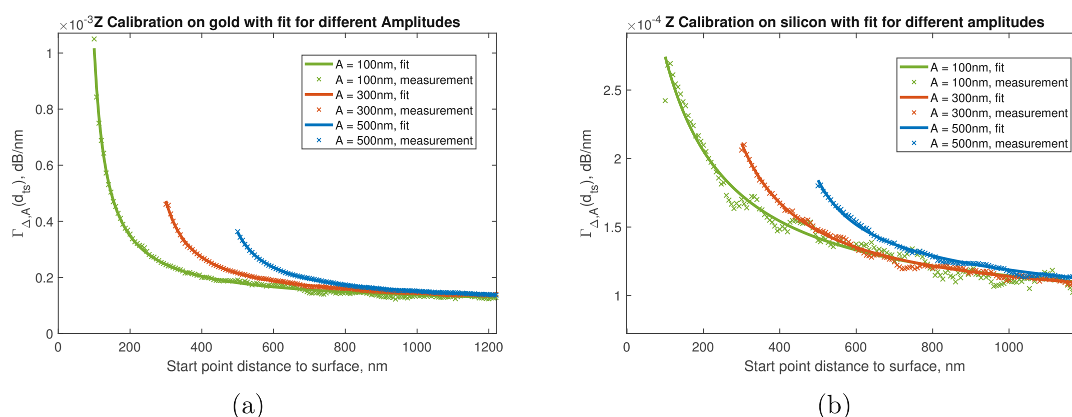

Figure 7.15: Vertical calibration on (a) gold electrode and (b) bulk silicon with fit for different amplitudes.

It might be wise to do a two part approach for the vertical positioning with two different amplitudes. A coarse positioning using a larger amplitude to be sure what material is underneath the tip, which is then followed by a fine positioning with a smaller amplitude that is able to reveal more detail.

7.3.1 Verification of vertical positioning

The verification of this vertical position is done with AFM by simply letting the controller run into a steady state and then extending the tip until contact can be detected in the deflection signal. Figure 7.16(a) shows a picture of the workflow and Figure 7.16(b) the deflection signal of such a force curve verification measurement with an oscillation amplitude of $A = 200$ nm, and a target distance of 490 nm on the gold electrode. A clear snap-in of the cantilever tip can be seen in the force curve where contact is established.

Die approbierte gedruckte Originalversion dieser Diplomarbeit ist an der TU Wien Bibliothek verfügbar
The approved original version of this thesis is available in print at TU Wien Bibliothek.
TU Bibliothek WIEN Your knowledge hub

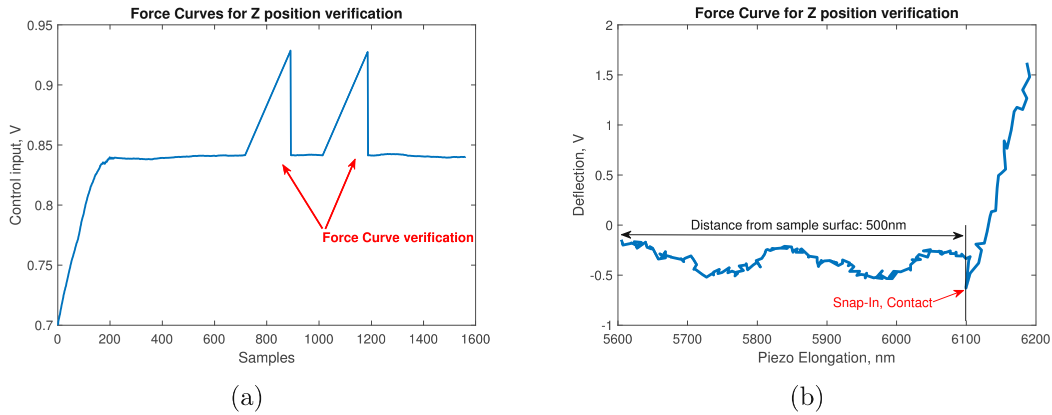

(a) (b)

Figure 7.16: (a) Strain gauge control signal during a verification measurement with amplitude $A = 200\,\text{nm}$ and target value $\Gamma_{\Delta,200nm}\,(d_{ts}) = 2\text{e-}4\,\text{dB}/\text{nm}$. Force Curves are recorded to calculate tip to sample distance. (b) Force Curve measurement to calculate tip to sample distance. Snap-in shows tip-sample contact.

It can be seen in Figure 7.16(b) that the target of 490 nm was missed by about 10 nm which is clearly within the goal of below 100 nm. To prove that this is not a coincidence, the same measurement is repeated with different target values (which are equivalent to tip to sample distances) for both sample surfaces in Figure 7.17(a) and Figure 7.18(a). The Y-axis in these plots show the absolute value of the error $|d_{ts} - d_{ts,des}|$ between the measured tip to sample distance d_{ts} and the desired distance $d_{ts,des}$. To illustrate the tip location corresponding to these desired values Figure 7.17(b) and 7.18(b) show the calibration curves with marks for the used values.

Figure 7.19(a) shows the absolute error for different amplitudes with the same target $\Gamma_{\Delta,A}\,(d_{ts}) = 2.5\text{e-}4\,\text{dB}/\text{nm}$ on the gold electrode and Figure 7.19(b) shows the expected offset distances for the amplitudes with this target.

Tables 7.1, 7.2 and 7.3 present the mean μ and standard deviation σ of the error $|d_{ts} - d_{ts,des}|$ of the respective measurements, calculated with Matlab using equation (7.5). The last column "AVG" is the average of the presented values for μ and σ in the respective table.

$$\mu = \frac{1}{N}\sum_{i=1}^{N} E_i, \quad \sigma = \sqrt{\frac{1}{N-1}\sum_{i=1}^{N} |E_i - \mu|^2}, \quad E_i = |d_{ts,i} - d_{ts,des}| \tag{7.5}$$

The mean value μ and standard deviation σ are marked in the error graphs Figures 7.17(a), 7.18(a) and 7.19(a) for their respective yellow coloured curves.

Die approbierte gedruckte Originalversion dieser Diplomarbeit ist an der TU Wien Bibliothek verfügbar
The approved original version of this thesis is available in print at TU Wien Bibliothek.
TU WIEN Bibliothek Your knowledge hub

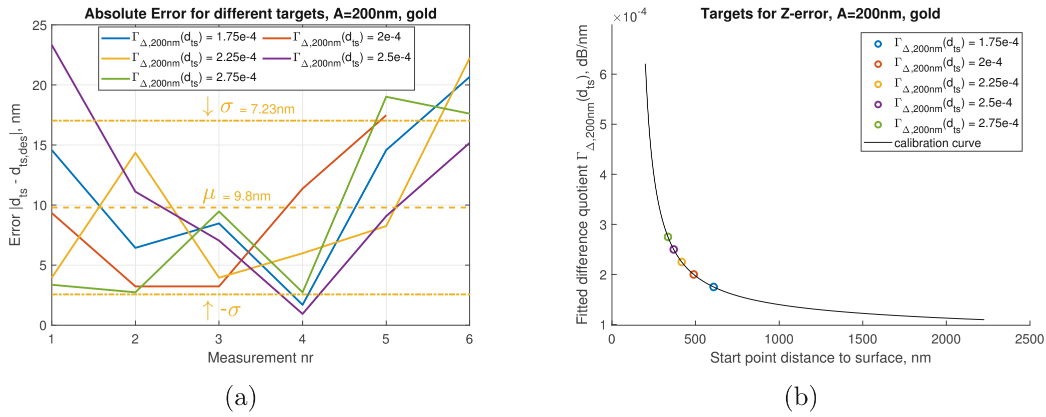

(a)

(b)

Figure 7.17: (a) Absolute distance to sample error for different targets on gold electrode with $A = 200\,\text{nm}$,(b) calibration curve with corresponding target values.

Gold, $\Gamma_{\Delta,200nm}\,(d_{ts})$	1.75e-4	2e-4	2.25e-4	2.5e-4	2.75e-4	AVG
Mean μ, nm	11.07	8.93	9.80	11.12	9.16	10.01
Std.-dev. σ, nm	6.83	6.00	7.23	7.61	7.54	7.04

Table 7.1: Mean and standard deviation of absolute error measurements on gold electrode with different targets.

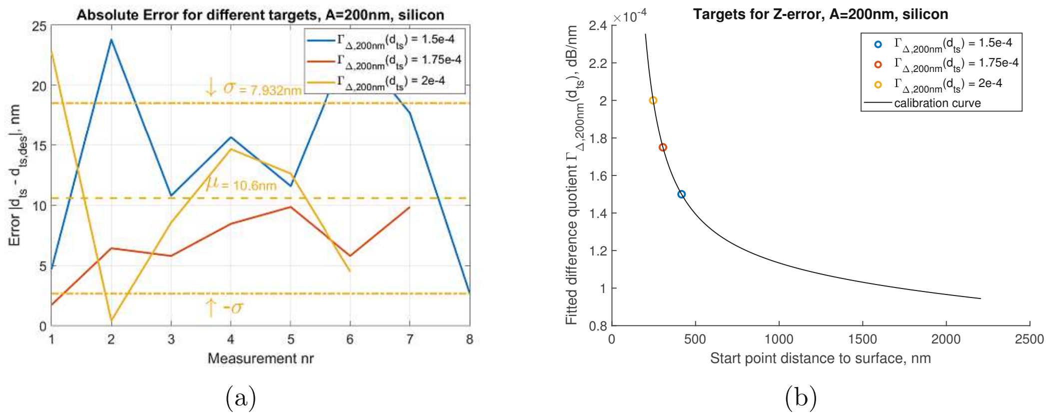

(a)

(b)

Figure 7.18: (a) Absolute distance to sample error for different targets on bulk silicon with $A = 200\,\text{nm}$,(b) calibration curve with corresponding target values.

Silicon, $\Gamma_{\Delta,200nm}\,(d_{ts})$	1.5e-4	1.75e-4	2e-4	AVG
Mean μ, nm	13.83	6.84	10.59	10.42
Std.-dev. σ, nm	7.92	2.87	7.93	6.24

Table 7.2: Mean and standard deviation of absolute error measurements on bulk silicon with different targets.

Die approbierte gedruckte Originalversion dieser Diplomarbeit ist an der TU Wien Bibliothek verfügbar
The approved original version of this thesis is available in print at TU Wien Bibliothek.
TU Bibliothek, WIEN Your knowledge hub

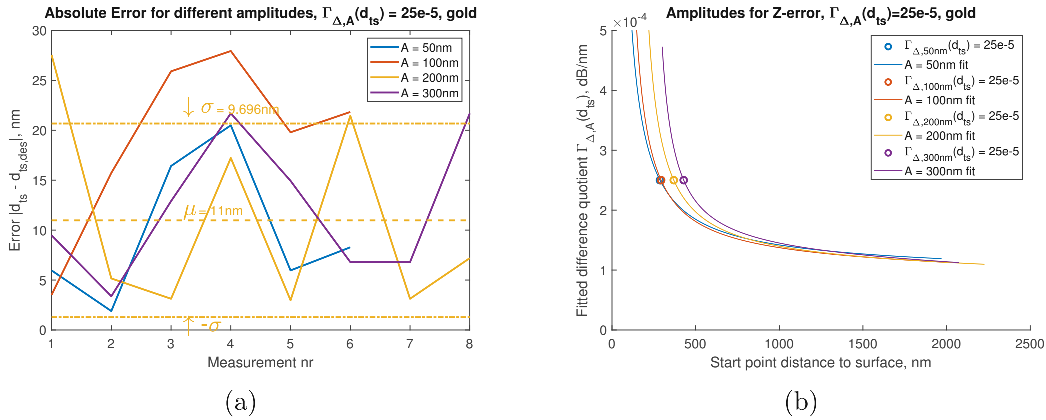

(a) (b)

Figure 7.19: (a) Absolute distance to sample error for different amplitudes on gold electrode with $\Gamma_{\Delta,A}(d_{ts}) = 2.5\text{e-}4\,\text{dB/nm}$, (b) calibration curves for $A = 50/100/200/300\,\text{nm}$ with corresponding target value.

Gold, $\Gamma_{\Delta,A}(d_{ts}) = 2.5\text{e-}4\,\text{dB/nm}$					
Amplitude A	50nm	100nm	200nm	300nm	AVG
Mean μ, nm	9.83	19.11	10.97	12.21	13.03
Std.-dev. σ, nm	7.10	8.79	9.70	6.88	8.12

Table 7.3: Mean and standard deviation of absolute error measurements on gold electrode with different amplitudes.

The absolute vertical positioning error stays within about 30 nm for any combination of $\Gamma_{\Delta,A}(d_{ts})$ target and amplitude A as long as they are chosen to be clearly on the non-linear part of the calibration curves. By choosing a suitable target value and amplitude for the task at hand, this can further be reduced to about 15 nm on the gold electrode, which is about the noise floor of the strain gauge position measurement. The higher than average mean error μ at $A = 100\text{nm}$ in Figure 7.19(a) and Table 7.3 is likely due to a calibration fault, which is observable in Figure 7.19(b)

There is no single best setting for all situations. As stated before not all target-amplitude-material combinations are available for all tasks. If materials are to be determined, a target has to be chosen that lies on the non-linear part of the calibration curves of all involved materials and those depend on the chosen amplitude, so a case by case study is recommended. When topography is to be scanned, a target farther off the surface with a smaller amplitude is advisable to minimize the risk of tip-surface-contact. If only a vertical position on a known material is of interest, then a high amplitude and a target close to the surface for highest SNR is the best choice.

Die approbierte gedruckte Originalversion dieser Diplomarbeit ist an der TU Wien Bibliothek verfügbar
The approved original version of this thesis is available in print at TU Wien Bibliothek.
TU Bibliothek WIEN Your knowledge hub

7.4 Lateral positioning

The lateral position can be defined through line scans in both horizontal axes. After coarse positioning of the cantilever tip by camera a line scan is initiated with a scan range large enough to cover the target. The controller that was used to control the offset (tip to sample distance) before, is now used to keep the difference quotient measurement at a target level. This target is chosen in such a way, that it lies on the steep slope of the worst reflective material composition with still some margin for error. Figure 7.20 shows that the target has to be in the range of 1.4e-4 to 2e-4 dB/nm for the non-passivated interdigital capacitor sample.

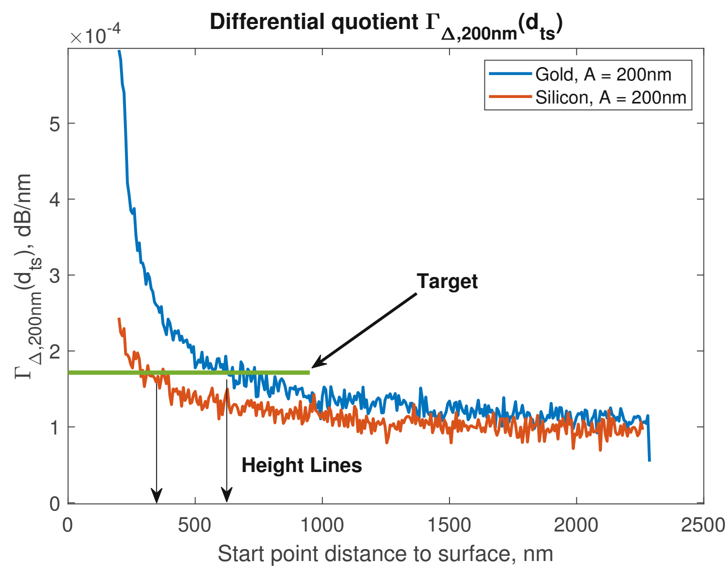

Figure 7.20: Possible target selection for lateral positioning and resulting height lines.

The points where the target line crosses the material calibration curves is the tip sample distance at which the controller tries to position the tip while scanning, depending on the current material underneath the tip. This produces height lines in the scan where each height represents a different material composition. Changes in topography and changes in material cause a transition to a different height line. Figure 7.21 shows such a scan on the interdigital capacitors finger structure together with the AFM scan as a ground truth reference. Both profiles are centred on their mean value in the Y axis.

Die approbierte gedruckte Originalversion dieser Diplomarbeit ist an der TU Wien Bibliothek verfügbar
The approved original version of this thesis is available in print at TU Wien Bibliothek.
TU WIEN Bibliothek Your knowledge hub

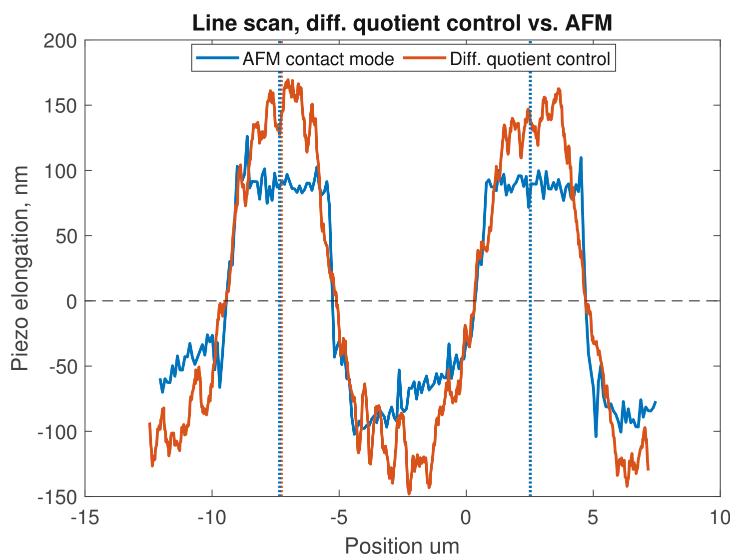

Figure 7.21: Line scan on interdigital capacitor sample with control of difference quotient at fixed target. Dotted lines mark the centre of the electrodes identified by zero crossings.

As expected the scan produces a signal that represents not only the topographical change, but also the material change when the tip transitions from gold finger to bulk silicon. The presented method can track topographical (and material) changes very closely although the step height on this sample is very high with the nominal 200 nm. A typical positioning task could be to position the tip on the centre of a finger electrode. Such a task could confidently be carried out with the required sub-micrometer accuracy by detecting the zero crossings in the above graph and calculating the centre in between. In this scan a resulting difference of 72 nm for the left, and 10 nm for the right electrode centre is observed, when compared to the AFM measurement. It has to be noted that the AFM pixel resolution in this measurement is about 100 nm and is interpolated for the zero-crossing detection. Thus the presented method lies within the pixel resolution of the AFM measurement.

To prove that this is also possible on passivated structures another line is scanned on one of the four passivated metal pads, which is nominally 15 μm by 15 μm as shown in Figure 7.22. Most of the scan looks as expected, with the trace on the left, the metal pad in the middle and a drop to silicon to the right.The unexpected dip in the centre is discussed later.

Die approbierte gedruckte Originalversion dieser Diplomarbeit ist an der TU Wien Bibliothek verfügbar
The approved original version of this thesis is available in print at TU Wien Bibliothek.
TU WIEN Bibliothek Your knowledge hub

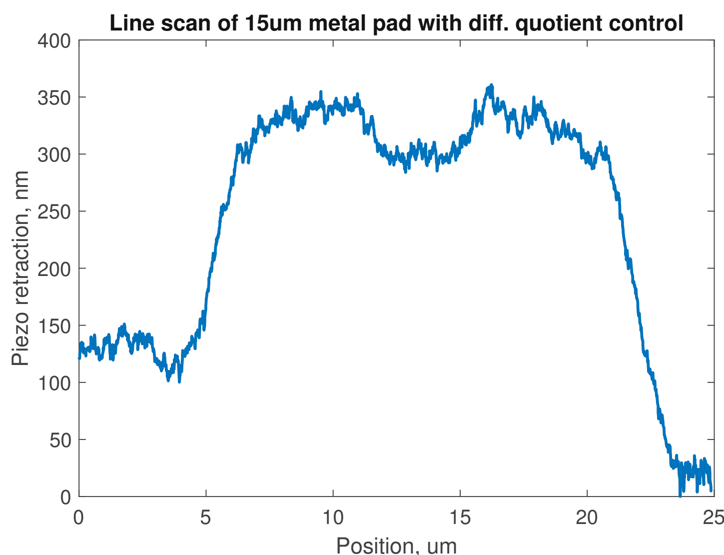

Figure 7.22: Line scan of passivated 15 μm square metal pad with diff. quotient control.

Verfication of the lateral position for buried structures, where AFM cannot be used (no topography), is conducted by a voltage sensing method (see Chapter 4.7) [53]. It is employed to scan a line of the same pad while the pad is excited by an RF voltage, that is partly transmitted to the cantilever tip. A non-linear capacitance model is fitted to the measurement data and a weighing factor that represents the local voltage at the tip is calculated. Figure 7.23 shows a normalized comparison between the two measurements. Blue is the weighting factor of the non-linear part of the measured transmitted voltage and red the piezo elongation while controlling the difference quotient to a fixed target (from 7.22).

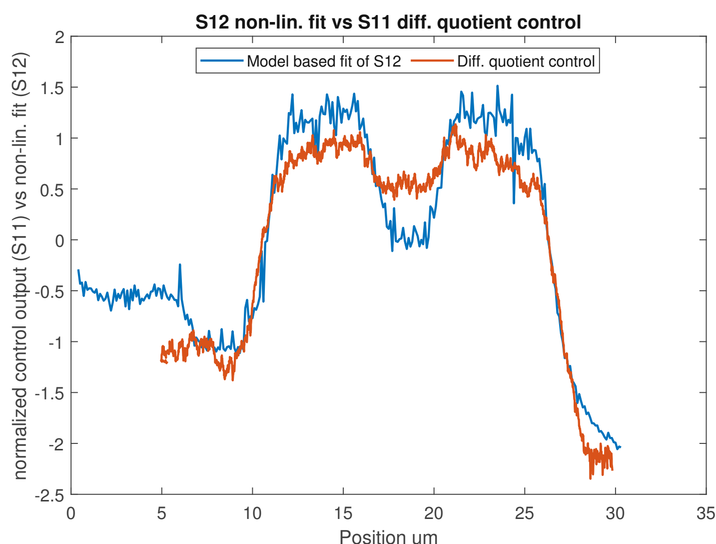

Figure 7.23: Normalized line scan on passivated square metal pad with diff. quotient control and model based voltage sensing.

Die approbierte gedruckte Originalversion dieser Diplomarbeit ist an der TU Wien Bibliothek verfügbar
The approved original version of this thesis is available in print at TU Wien Bibliothek.
TU WIEN Bibliothek Your knowledge hub

The transitions between the different material compositions in the difference quotient control perfectly track the voltage distribution in the device. Again a simple positioning task could be to find the centre of the pad by detecting the zero crossings, which results in a difference between the calculated centres of 122 nm. The resolution of the verification measurement is 100 nm, as in the AFM verification scan before. This satisfies the required sub-micrometer accuracy goal. The difference in contrast might be due to the different ranges of the measurements. The S_{12} measurement has a range of 4 μm and uses the complete approach curve to calculate the non-linear weighting factor, while the difference quotient here uses only the linear information of its 200 nm amplitude.

The employed method for scanning is reliable, yet relatively slow when compared to other scanning methods. Since a controller update happens at the fastest setting only every 33 ms (20 ms for data capturing, 5 ms rise and fall, 3 ms safety to be sure that the VNA is ready for the next measurement cycle) it needs quite some time to reach a steady state and therefore heavily limits scan speed. The scans above where recorded at 0.175 μm/s (about 3.5 min for the shown 35 μm scan) and the initial steady state (a first defined stable tip to sample distance at a target value) is reached after half a minute. Therefore a complete lateral scan consisting of at least two line scans (one in each axis) takes about 10 minutes to finish. Improvements to this could mainly be implemented at the VNA and the signal path. SCPI communication sometimes takes longer than expected and IF bandwidth could be wider, if a better SNR can be achieved. Scan speed scales almost linearly with the amount of points to be averaged (10 in this implementation) and with IF bandwidth, which directly influences the minimum time between triggers for those measurement points. An improvement up to a factor of 10 is believed to be achievable if the signal path can be optimised and/or shielded.

An unexpected error is revealed in the middle of the pad in Figure 7.22 and Figure 7.23. Such a clear dip has to be a change in the material composition, since the surface is completely flat (verified by AFM, not shown here). Coincidentally there is a via at this location (also visible in the image in Figure 7.3), that was presumed to be fully metal and at the same height as the pad. The next chapter shows that this is not a coincidence but all vias on the sample behave this way.

7.5 Faults and unexpected behaviours

Figure 7.23 shows the influence of a via in the measurement which is not expected. Figure 7.24 shows a line scan of the structure next to the metal pads, above the vias and in the middle of the structure, off the vias. These measurements are conducted using the non-linear fitting method from before, since it can perform faster line scans (that periodically need to contact the surface) with the same information (as shown above).

Die approbierte gedruckte Originalversion dieser Diplomarbeit ist an der TU Wien Bibliothek verfügbar
The approved original version of this thesis is available in print at TU Wien Bibliothek.
TU WIEN Bibliothek Your knowledge hub

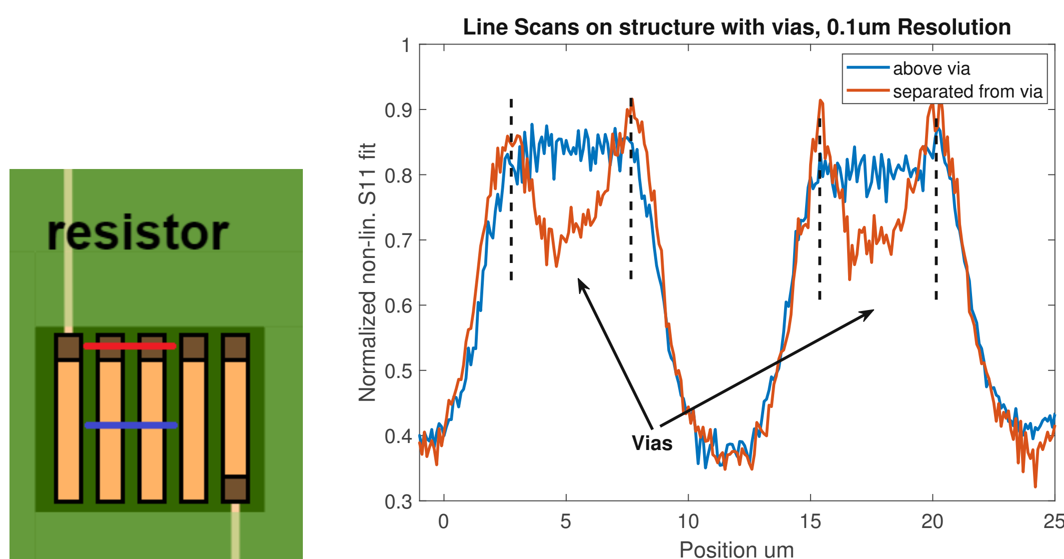

Figure 7.24: Normalized line scan on passivated resistor structure with non-linear fitting method at two different locations.

Detecting unforeseen sample properties is not the main concern of this work, but this example shows that it is possible to find faults and impurities with it. Other investigation methods are likely to be better suited for the identification of the real implications of this, since the contactless property of this measurement method is unnecessarily complex for the task. Another possible use case may be to characterize unknown devices since every distinct height line in a scan represents a different material composition.

In conclusion this work presents a measurement method that enables accurate positioning in all spatial dimensions. Lateral positioning is done by line scans, and vertical positioning by calibration and a feedback control loop of the calculated difference quotient of a differential measurement. Simple lateral positioning tasks can be carried out on passivated and non-passivated structures with sub-micrometer accuracy. The presented examples feature lateral positioning errors of ≈10-122 nm when the centre of a structure is calculated by zero-crossing detection when compared to AFM scans or voltage distribution scans, that both feature 100 nm resolution. When a suitable lateral position is found, a vertical positioning task can be conducted using fitted calibration curves. This requires knowledge of the material underneath the tip and a sensible choice of oscillation amplitude, but can generally be expected to be within 30 nm of the intended tip to sample distance, which is confirmed by detecting the snap-in in force curve measurements.

Die approbierte gedruckte Originalversion dieser Diplomarbeit ist an der TU Wien Bibliothek verfügbar
The approved original version of this thesis is available in print at TU Wien Bibliothek.
TU WIEN Bibliothek Your knowledge hub

CHAPTER 8

Conclusion and Outlook

8.1 Summary and Conclusion

The number of devices operating in the micro- and millimetre wave spectrum increases rapidly and structure sizes decrease to achieve higher device densities in production. Small, cantilever-based probes can be used without any conductive contact in high frequency measurements to probe these devices, but are difficult to position accurately, especially on passivated structures. This work presents a contactless method to position a probe in all spatial dimensions on a point of interest of known material composition, without any mechanical interaction between the probe and the DUT, to ensure mechanical integrity of the probe in high volume measurements.

The method works by detecting the changes of either topography, or material underneath a sharp tip. It is inspired by scanning microwave microscopy, but uses a differential approach to overcome difficulties with drifting measurement equipment and low sensitivity in contactless measurements. The method uses the difference in the reflection coefficient at the tip to sample interface, measured at two stand-off distances from the surface, as the measurement quantity.

A test setup is developed to implement this method, consisting of a custom AFM that is extended with SMM capabilities by interfacing a conductive cantilever with a VNA by a waveguide. Most parts of the setup are controlled with a real time system and some custom electronics. The AFM is used to verify the vertical position, by tip to sample distances that are measured with force curves, and lateral positioning performance via topography maps in contact mode. SMM is implemented in contact mode and AFM lift mode to verify the feasibility of the proposed positioning strategy. Adaptions to the microwave measurements are made to incorporate the differential nature mentioned above to combat drift. A calibration procedure is carried out on samples with and without passivation. It is used to vertically position the cantilever tip at different heights. The influence of the differential amplitude is investigated for two materials and appropriate settings for good vertical accuracy are formulated. A

Die approbierte gedruckte Originalversion dieser Diplomarbeit ist an der TU Wien Bibliothek verfügbar
The approved original version of this thesis is available in print at TU Wien Bibliothek.
TU WIEN Bibliothek Your knowledge hub

software controller is implemented to keep the differential measurement at a constant level during a line scan over two calibrated samples. This produces height lines for different materials underneath the tip, which are used to determine topographical and material features of the tested samples. These features can be used to position the tip laterally. Topography maps are used to verify measurements on non-passivated samples and a voltage distribution measurement is used to verify changes on a passivated sample. An unexpected material change is found during the tests and investigated.

Vertical positioning is performed with a typical absolute error of less than 30 nm for any of the tested configurations and an average error of 10 nm to 14 nm is found with a standard deviation less than 10 nm across all measurements. This satisfies the stated accuracy goal of less than 100 nm. A simple lateral positioning task is formulated as finding the centre of a structure. Such a task is performed with errors well below the intended sub-micrometer accuracy. Lateral errors of 10 nm, 72 nm and 122 nm are found when comparing the measurements with AFM and voltage sensing methods that feature 100 nm lateral resolution. The setup is limited in its scan speed by the required filter bandwidth of the VNA measurements to about 10 μm per minute.

In conclusion all of the set goals are achieved, although not with the exact methods that were envisioned at the beginning. Tip to sample contact is minimized to calibration only and accuracy goals have been met with a method that is robust enough for large scale, high volume measurements.

8.2 Outlook

There are many details that arose during this work that are worth investigating, which simply lie outside the intended scope. First and foremost an investigation of different cantilever tips is necessary. While the one presented in this work was chosen for its long narrow tip it is just one out of many different probe geometries and materials available. In theory any cantilever that can reduce crosstalk to surrounding structures could work (i.e. shielded cantilevers). In the same vein an investigation of probe wear (i.e. with SEM) on the quality of the measurements and calibration presented in this work is advisable before it can be applied in the field. Another point of possible improvements is the system performance during scanning operations. This could be achieved with a better signal path to increase SNR and allow faster VNA measurements, either by cutting back on the averaged points or using higher IF bandwidths. A method to increase sensitivity (and therefore SNR), that is more stable than the presented interferometric method, could boost the performance as well.

Die approbierte gedruckte Originalversion dieser Diplomarbeit ist an der TU Wien Bibliothek verfügbar
The approved original version of this thesis is available in print at TU Wien Bibliothek.
TU WIEN Bibliothek Your knowledge hub

Bibliography

[1] D. M. Mittleman, "Twenty years of terahertz imaging," *Opt. Express*, vol. 26, no. 8, pp. 9417–9431, Apr 2018.

[2] Ericsson. Ericsson mobility report november 2022. [Online]. Available: https://www.ericsson.com/4ae28d/assets/local/reports-papers/mobility-report/documents/2022/ericsson-mobility-report-november-2022.pdf (Accessed 11.12.2022).

[3] statista. Semiconductor market size worldwide from 1987 to 2022. [Online]. Available: https://www.statista.com/statistics/266973/global-semiconductor-sales-since-1988/ (Accessed 11.12.2022).

[4] MPI-AST. Failure analysis. [Online]. Available: https://www.mpi-corporation.com/ast/applications/failure-analysis/ (Accessed 11.12.2022).

[5] H. Li, F. T. von Kleist-Retzow, O. C. Haenssler, S. Fatikow, and X. Zhang, "Multi-target tracking for automated rf on-wafer probing based on template matching," in *2019 International Conference on Manipulation, Automation and Robotics at Small Scales (MARSS)*, 2019, pp. 1–6.

[6] R. Hou, M. Lorenzini, M. Spirito, T. Roedle, F. van Rijs, and L. C. N. de Vreede, "Nonintrusive near-field characterization of spatially distributed effects in large-periphery high-power gan hemts," *IEEE Transactions on Microwave Theory and Techniques*, vol. 64, no. 11, pp. 4048–4062, 2016.

[7] N. Dehghan and S. Cripps, "A novel in-situ calibration technique for a high resolution e-field probe," in *2015 IEEE MTT-S International Microwave Symposium*, 2015, pp. 1–3.

[8] S.-C. Lee and S. Anlage, "Study of local nonlinear properties using a near-field microwave microscope," *IEEE Transactions on Applied Superconductivity*, vol. 13, no. 2, pp. 3594–3597, 2003.

Die approbierte gedruckte Originalversion dieser Diplomarbeit ist an der TU Wien Bibliothek verfügbar
The approved original version of this thesis is available in print at TU Wien Bibliothek.
TU WIEN Bibliothek Your knowledge hub

[9] E. Brinciotti, G. Badino, M. Knaipp, G. Gramse, J. Smoliner, and F. Kienberger, "Calibrated nanoscale dopant profiling and capacitance of a high-voltage lateral mos transistor at 20 ghz using scanning microwave microscopy," *IEEE Transactions on Nanotechnology*, vol. 16, no. 2, pp. 245–252, 2017.

[10] STMicroelectronics, *Application Note 900*. [Online]. Available: https://www.st.com/resource/en/application_note/cd00003986-introduction-to-semiconductor-technology-stmicroelectronics.pdf (Accessed 11.12.2022).

[11] A. Imtiaz, T. M. Wallis, and P. Kabos, "Near-field scanning microwave microscopy: An emerging research tool for nanoscale metrology," *IEEE Microwave Magazine*, vol. 15, no. 1, pp. 52–64, 2014.

[12] G. Alvarez-Botero, R. Torres-Torres, and R. Murphy Arteaga, "Modeling and parameter extraction of test fixtures for mosfet on- wafer measurements up to 60 ghz," *International Journal of RF and Microwave Computer-Aided Engineering*, vol. 23, 10 2013.

[13] FormFactor. Cascade pm8 200mm manual porbe system datasheet. [Online]. Available: https://www.formfactor.com/download/pm8-data-sheet/ (Accessed 29.12.2022).

[14] K. Daffe, J. Marzouk, A. E. Fellahi, T. Xu, C. Boyaval, S. Eliet, B. Grandidier, S. Arscott, G. Dambrine, and K. Haddadi, "Nano-probing station incorporating mems probes for 1d device rf on-wafer characterization," in *2017 47th European Microwave Conference (EuMC)*, 2017, pp. 831–834.

[15] S. Anlage, V. Talanov, and A. Schwartz, *Principles of Near-Field Microwave Microscopy*, 01 2006, vol. 1, pp. 207–245.

[16] W. Fang, H. Qiu, C. Luo, L. Wang, W. Shao, E. Shao, S. Li, and Y. En, "Noncontact rf voltage sensing of a printed trace via a capacitive-coupled probe," *IEEE Sensors Journal*, vol. 18, no. 21, pp. 8873–8882, 2018.

[17] R. Hou, M. Lorenzini, M. Spirito, T. Roedle, F. van Rijs, and L. C. N. de Vreede, "Nonintrusive near-field characterization of spatially distributed effects in large-periphery high-power gan hemts," *IEEE Transactions on Microwave Theory and Techniques*, vol. 64, no. 11, pp. 4048–4062, 2016.

[18] X. He, X.-C. Li, Z.-H. Peng, Y.-X. Liu, and J.-F. Mao, "An ultrawideband magnetic probe with high electric field suppression ratio," *IEEE Transactions on Instrumentation and Measurement*, vol. 70, pp. 1–9, 2021.

[19] Y. Yang, K. Lai, Q. Tang, W. Kundhikanjana, M. Kelly, K. Zhang, Z.-x. Shen, and X. Li, "Batch-fabricated cantilever probes with electrical shielding for nanoscale dielectric and conductivity imaging," *Journal of Micromechanics and Microengineering*, vol. 22, 01 2013.

Die approbierte gedruckte Originalversion dieser Diplomarbeit ist an der TU Wien Bibliothek verfügbar
The approved original version of this thesis is available in print at TU Wien Bibliothek.
TU WIEN Bibliothek Your knowledge hub

[20] M. Tabib-Azar and Y. Wang, “Design and fabrication of scanning near-field microwave probes compatible with atomic force microscopy to image embedded nanostructures,” *IEEE Transactions on Microwave Theory and Techniques*, vol. 52, no. 3, pp. 971–979, 2004.

[21] K. Lai, W. Kundhikanjana, M. A. Kelly, and Z.-X. Shen, “Nanoscale microwave microscopy using shielded cantilever probes,” *Applied Nanoscience*, vol. 1, pp. 13–18, 2011.

[22] F. Hui and M. Lanza, “Scanning probe microscopy for advanced nanoelectronics,” *Nature electronics*, vol. 2, no. 6, pp. 221–229, 2019.

[23] M. J. Cadena, R. G. Reifenberger, and A. Raman, “High resolution subsurface imaging using resonance-enhanced detection in 2nd-harmonic kpfm,” *Nanotechnology*, vol. 29, no. 40, p. 405702, 2018.

[24] W. Melitz, J. Shen, A. C. Kummel, and S. Lee, “Kelvin probe force microscopy and its application,” *Surface Science Reports*, vol. 66, no. 1, pp. 1–27, 2011.

[25] P. Girard, “Electrostatic force microscopy: principles and some applications to semiconductors,” *Nanotechnology*, vol. 12, no. 4, p. 485, nov 2001.

[26] B. Feenstra, C. Vlahacos, A. Thanawalla, D. Steinhauer, S. Dutta, F. Wellstood, and S. Anlage, “Near-field scanning microwave microscopy: measuring local microwave properties and electric field distributions,” in *1998 IEEE MTT-S International Microwave Symposium Digest (Cat. No.98CH36192)*, vol. 2, 1998, pp. 965–968 vol.2.

[27] U. Hartmann, “Magnetic force microscopy,” *Annual review of materials science*, vol. 29, no. 1, pp. 53–87, 1999.

[28] R. Wiesendanger, *Scanning probe microscopy and spectroscopy: methods and applications*. Cambridge university press, 1994.

[29] P. Polovodov, D. Théron, S. Eliet, V. Avramovic, C. Boyaval, D. Deresmes, G. Dambrine, and K. Haddadi, “Operation of near-field scanning millimeter-wave microscopy up to 67 ghz under scanning electron microscopy vision,” in *2020 IEEE/MTT-S International Microwave Symposium (IMS)*, 2020, pp. 95–98.

[30] U. Mueller, C. Boehm, J. Sprengepiel, C. Roths, E. Kubalek, and A. Beyer, “Geometrical and voltage resolution of electrical sampling scanning force microscopy,” in *1994 IEEE MTT-S International Microwave Symposium Digest (Cat. No.94CH3389-4)*, 1994, pp. 1005–1008 vol.2.

[31] K. Torigoe, M. Arita, and T. Motooka, “Sensitivity analysis of scanning microwave microscopy for nano-scale dopant measurements in si,” *Journal of Applied Physics*, vol. 112, 11 2012.

Die approbierte gedruckte Originalversion dieser Diplomarbeit ist an der TU Wien Bibliothek verfügbar
The approved original version of this thesis is available in print at TU Wien Bibliothek.
TU WIEN Bibliothek Your knowledge hub

[32] E. Brinciotti, G. Gramse, S. Hommel, T. Schweinboeck, A. Altes, M. A. Fenner, J. Smoliner, M. Kasper, G. Badino, S.-S. Tuca, and F. Kienberger, "Probing resistivity and doping concentration of semiconductors at the nanoscale using scanning microwave microscopy," *Nanoscale*, vol. 7, pp. 14 715–14 722, 2015.

[33] D. E. Steinhauer, C. P. Vlahacos, S. K. Dutta, F. C. Wellstood, and S. M. Anlage, "Surface resistance imaging with a scanning near-field microwave microscope," *Applied Physics Letters*, vol. 71, no. 12, pp. 1736–1738, 1997.

[34] D. E. Steinhauer, C. P. Vlahacos, F. C. Wellstood, S. M. Anlage, C. Canedy, R. Ramesh, A. Stanishevsky, and J. Melngailis, "Imaging of microwave permittivity, tunability, and damage recovery in (ba, sr)tio3 thin films," *Applied Physics Letters*, vol. 75, no. 20, pp. 3180–3182, 1999.

[35] C. Gao, B. Hu, I. Takeuchi, K.-S. Chang, X.-D. Xiang, and G. Wang, "Quantitative scanning evanescent microwave microscopy and its applications in characterization of functional materials libraries," *Measurement Science and Technology*, vol. 16, no. 1, p. 248, dec 2004.

[36] A. Karbassi, D. Ruf, A. D. Bettermann, C. A. Paulson, D. W. van der Weide, H. Tanbakuchi, and R. Stancliff, "Quantitative scanning near-field microwave microscopy for thin film dielectric constant measurement," *Review of Scientific Instruments*, vol. 79, no. 9, p. 094706, 2008.

[37] K. A. Rubin, Y. Yang, O. Amster, D. A. Scrymgeour, and S. Misra, *Scanning Microwave Impedance Microscopy (sMIM) in Electronic and Quantum Materials*. Cham: Springer International Publishing, 2019, pp. 385–408.

[38] S.-S. Tuca, M. Kasper, F. Kienberger, and G. Gramse, "Interferometer scanning microwave microscopy: Performance evaluation," *IEEE Transactions on Nanotechnology*, vol. 16, no. 6, pp. 991–998, 2017.

[39] C. C. Williams, W. P. Hough, and S. A. Rishton, "Scanning capacitance microscopy on a 25 nm scale," *Applied Physics Letters*, vol. 55, no. 2, pp. 203–205, 1989.

[40] M. Awadein, M. Sparey, S. Grall, F. Kienberger, N. Clément, and G. Gramse, "Nanoscale electrochemical charge transfer kinetics investigated by electrochemical scanning microwave microscopy," *Nanoscale Advances*, 2022.

[41] J. Smoliner, H. P. Huber, M. Hochleitner, M. Moertelmaier, and F. Kienberger, "Scanning microwave microscopy/spectroscopy on metal-oxide-semiconductor systems," *Journal of Applied Physics*, vol. 108, no. 6, p. 064315, 2010.

[42] M. Soliman, Y. Ding, and L. Tetard, "Nanoscale subsurface imaging," *Journal of Physics: Condensed Matter*, vol. 29, no. 17, p. 173001, mar 2017.

[43] L. You, J.-J. Ahn, Y. S. Obeng, and J. J. Kopanski, "Subsurface imaging of metal lines embedded in a dielectric with a scanning microwave microscope*," *Journal of Physics D: Applied Physics*, vol. 49, no. 4, p. 045502, dec 2015.

Die approbierte gedruckte Originalversion dieser Diplomarbeit ist an der TU Wien Bibliothek verfügbar
The approved original version of this thesis is available in print at TU Wien Bibliothek.
TU WIEN Bibliothek Your knowledge hub

[44] G. Gramse, A. Koelker, T. Lim, T. J. Z. Stock, H. Solanki, S. R. Schofield, E. Brinciotti, G. Aeppli, F. Kienberger, and N. J. Curson, "Nondestructive imaging of atomically thin nanostructures buried in silicon," *Science Advances*, vol. 3, no. 6, p. e1602586, 2017.

[45] C. Plassard, E. Bourillot, J. Rossignol, Y. Lacroute, E. Lepleux, L. Pacheco, and E. Lesniewska, "Detection of defects buried in metallic samples by scanning microwave microscopy," *Physical Review B*, vol. 83, p. 121409, 03 2011.

[46] C. Mecklenbräuker, G. Lasser, and E. Bonek, *Lecture Script to "Wellenausbreitung LVA 389.064" at Institute of Telecommunications, TU Wien*, 12th ed., September 2014.

[47] A. Prechtl, *Lecture Script to "Elektrodynamik" at Institute of Electrodynamics, Microwave and Circuit Engineering, TU Wien*, 2010.

[48] M. Steer, *Microwave and RF Design: Transmission Lines*, 3rd ed. North Carolina State University Libraries, September 2019, vol. 2.

[49] B. Wadell, *Transmission Line Design Handbook*, ser. Artech House Aantennas and Propagation Library. Artech House, 1991.

[50] R. Simons, *Coplanar Waveguide Circuits, Components, and Systems*, ser. Wiley Series in Microwave and Optical Engineering. Wiley, 2004.

[51] K. Haddadi and T. Lasri, "Interferometric technique for microwave measurement of high impedances," *2012 IEEE/MTT-S International Microwave Symposium Digest*, pp. 1–3, 2012.

[52] ANASYS, *Standard AFM Modes User's Manual*. [Online]. Available: https://lsa.umich.edu/content/dam/chem-assets/chem-docs/00-0018-01%20Standard%20AFM%20Modes.pdf (Accessed 30.12.2022).

[53] M. Poik, T. Hackl, S. Di Martino, M. Schober, J. Dang, and G. Schitter, "Model-based rf sensing for contactless high resolution voltage measurements," ***Submitted*** *to IEEE Transactions on Instrumentation and Measurement*, 2022.

[54] K. Haddadi, O. Haenssler, K. Daffe, S. Eliet, C. Boyaval, D. Theron, and G. Dambrine, "Combined scanning microwave and electron microscopy: A novel toolbox for hybrid nanoscale material analysis," in *2017 IEEE MTT-S International Microwave Workshop Series on Advanced Materials and Processes for RF and THz Applications (IMWS-AMP)*. IEEE, 2017, pp. 1–3.

[55] A. Sain and K. L. Melde, "Impact of ground via placement in grounded coplanar waveguide interconnects," *IEEE Transactions on Components, Packaging and Manufacturing Technology*, vol. 6, no. 1, pp. 136–144, 2015.

[56] T. Schweinböck and S. Hommel, "Quantitative scanning microwave microscopy: A calibration flow," *Microelectronics Reliability*, vol. 54, no. 9, pp. 2070–2074, 2014, sI: ESREF 2014.

TU WIEN Bibliothek Your knowledge hub
Die approbierte gedruckte Originalversion dieser Diplomarbeit ist an der TU Wien Bibliothek verfügbar
The approved original version of this thesis is available in print at TU Wien Bibliothek.

[57] H. Adriaens, W. L. De Koning, and R. Banning, "Modeling piezoelectric actuators," *IEEE/ASME transactions on mechatronics*, vol. 5, no. 4, pp. 331–341, 2000.

[58] M. Radmacher, "Measuring the elastic properties of biological samples with the afm," *IEEE Engineering in Medicine and Biology Magazine*, vol. 16, no. 2, pp. 47–57, 1997.

[59] O. D. S. Ferreira, E. Gelinck, D. de Graaf, and H. Fischer, "Adhesion experiments using an afm-parameters of influence," *Applied Surface Science*, vol. 257, no. 1, pp. 48–55, 2010.

Die approbierte gedruckte Originalversion dieser Diplomarbeit ist an der TU Wien Bibliothek verfügbar
The approved original version of this thesis is available in print at TU Wien Bibliothek.
TU WIEN Bibliothek Your knowledge hub

TECHNISCHE UNIVERSITÄT WIEN

Ich habe zur Kenntnis genommen, dass ich zur Drucklegung meiner Arbeit unter der Bezeichnung

DIPLOMARBEIT

nur mit Bewilligung der Prüfungskommission berechtigt bin.

Ich erkläre an Eides statt, dass die vorliegende Arbeit nach den anerkannten Grundsätzen für wissenschaftliche Abhandlungen von mir selbstständig erstellt wurde. Alle verwendeten Hilfsmittel, insbesondere die zugrunde gelegte Literatur, sind in dieser Arbeit genannt und aufgelistet. Die aus den Quellen wörtlich entnommenen Stellen, sind als solche kenntlich gemacht.

Das Thema dieser Arbeit wurde von mir bisher weder im In- noch Ausland einer Beurteilerin/einem Beurteiler zur Begutachtung in irgendeiner Form als Prüfungsarbeit vorgelegt. Diese Arbeit stimmt mit der von den Begutachterinnen/Begutachtern beurteilten Arbeit überein.

Ich nehme zur Kenntnis, dass die vorgelegte Arbeit mit geeigneten und dem derzeitigen Stand der Technik entsprechenden Mitteln (Plagiat-Erkennungssoftware) elektronisch-technisch überprüft wird. Dies stellt einerseits sicher, dass bei der Erstellung der vorgelegten Arbeit die hohen Qualitätsvorgaben im Rahmen der geltenden Regeln zur Sicherung guter wissenschaftlicher Praxis „Code of Conduct“ an der TU Wien eingehalten wurden. Zum anderen werden durch einen Abgleich mit anderen studentischen Abschlussarbeiten Verletzungen meines persönlichen Urheberrechts vermieden.

Stadt und Datum | *Unterschrift*

Die approbierte gedruckte Originalversion dieser Diplomarbeit ist an der TU Wien Bibliothek verfügbar
The approved original version of this thesis is available in print at TU Wien Bibliothek.
TU WIEN Bibliothek Your knowledge hub